Seismic Performance of Ductile Reinforced Concrete Masonry Shear Walls with C-Shaped Boundary Elements

Mohammed Lotfy Albutainy

A Thesis
In The Department
of
Building, Civil, and Environmental Engineering

Presented in Partial Fulfillment of the Requirements

for the Degree of

Doctor of Philosophy (Civil Engineering) at

Concordia University

Montreal, Quebec, Canada

October 2022

© Mohammed Lotfy Albutainy, 2022

CONCORDIA UNIVERSITY

School of graduate studies

This is to certify that the thesis prepared

By: Mohammed Lotfy Albutainy

Title: Seismic Performance of Ductile Reinforced Concrete Masonry Shear Walls with C-Shaped Boundary Elements.

and submitted in partial fulfilment of the requirements for the degree of

Doctor of philosophy *(Civil Engineering)*

complies with the regulations of the University and meets the accepted standards with respect to originality and quality.

Signed by the final examining committee:

_____ Chair
Dr. Ahmed A. Kishk

_____ External Examiner
Dr. Mohamed ElGawady

_____ External to Program
Dr. Ramin Sedaghati

_____ Examiner
Dr. Ashutosh Bagchi

_____ Examiner
Dr. Anjan Bhowmick

_____ Thesis Supervisor
Dr. Khaled Galal

Approved by _____
                      Dr. Mazdak Nik-Bakht, Graduate Program Director

_____
Dr. Mourad Debbabi, Dean
Gina Cody School of Engineering and Computer Science

Date of Defence: 2022-10-04

ii

ABSTRACT

Seismic Performance of Ductile Reinforced Concrete Masonry Shear Walls with C-Shaped Boundary Elements

Mohammed Albutainy, Ph.D.
Concordia University, 2022

There is a global drive to promote and optimize the design of higher building performance at low cost and minimum environmental impact. Although reinforced masonry construction is known for its better fire protection, structural durability, energy efficiency and cost reduction, its use is hindered by the lack of knowledge of its resistance to earthquake loads. The main objective of this research is to quantify the effect of influential parameters on the seismic performance of Reinforced Masonry Shear Walls with Boundary Elements (RMSW+BE). The parameters to be investigated are the size of the boundary element, the spacing between the transverse reinforcement hoops and the vertical reinforcement ratio in the boundary elements.

This research is divided into experimental and numerical investigations. A new system/configuration for RMSW+BE with C-shaped units to form the BE is proposed and implemented, and a new experimental setup is designed and built to capture the response of the lower panel of RMSW+BE in a 12-storey building subject to quasi-static loading protocol. Experimental and numerical research study intended to improve reinforced masonry shear walls' structural performance and constructability. A testing system capable of testing RMSW+BE with a high aspect ratio was developed along with the control system. For this investigation, six half-scale RMSW+BE defined by flexural dominance under continuous axial stress and reversed cyclic top moment and lateral loading were built and tested. The tested walls represent the lower storey panel of a reinforced masonry shear wall in a 12-storey building to simulate the plastic hinge zone for these walls. The boundary elements were constructed using C-shape masonry units rather than stretcher units. This study considered the size, vertical reinforcement ratio, and boundary element confinement ratio of the wall's boundary elements as variables. An experimentally validated model was created to assess the effect of changing the confinement reinforcement ratio in reinforced masonry wall boundary elements. The model was validated using the outcomes of three different experimental programs. To examine the influence of the boundary element's eccentricity on the accuracy of the 2D model findings, the results from the 2D model and the 3D model were compared. Furthermore, the effect of the loading strategy

(cyclic vs monotonic) on wall curvature was investigated. The model was used to investigate the effect of modifying the confinement ratio in the boundary element by adjusting the spacing between the confinement hoops on the RMSW's behaviour.

The results showed that the proposed experimental setup and control system could represent the loading conditions on the plastic hinge zone of a 12-storey high masonry wall. From the constructability point of view, it was proven that the C-shaped units provided the lateral strength as designed and provided design engineers with the option of increasing the vertical and confinement reinforcement and the flexibility to change the boundary element length. Additionally, it is anticipated that using C-shaped masonry units to form the boundary elements can reduce the required manpower and the time needed to build the wall compared to the walls constructed using regular stretcher units. The proposed system could provide the lateral strength and ductility required to resist earthquake events. The tested walls were dominated by a flexural failure mode. The enhanced C-shaped boundary element did not change the out-of-plan stability required by the CSA S304-14 "Design of Masonry Structures" design standard. Additionally, it was demonstrated that when subjected to quasi-static reversed cyclic loading, RMSW with C-shaped boundary elements can provide a high level of ductility with minimal strength degradation.

The developed and validated numerical 2D and 3D models showed that the eccentricity of the boundary elements is not affecting the predicted lateral force capacity, initial stiffness, stiffness degradation and energy dissipated in each cycle. In addition, reducing the spacing between the confinement hoops does not affect the yield and the ultimate lateral resistance and stiffness degradation. However, reducing the spacing between the confinement reinforcement leads to an increase in the number of cycles to failure and delays/prevents the vertical reinforcement buckling, which reflects the increase in the ductility of the wall. It also increases the amount of energy dissipated by the wall, which enhances the seismic behaviour of the structure and shifts the failure to the next weaker area (i.e., the web).

Dedications

To my beloved parents; Lotfy and Huda,

To my lovely wife; Mariam Saleh,

To my beautiful daughters; Malak and Mila,

To my sisters; Rania and Reem,

To my biggest supporters; Helmi and Maha.

Table of Contents

List of Figures

List of Tables

Chapter 1
Introduction

1.1 Background and problem definition

With increasing environmental and economic concerns, there is a global drive to raise the efficiency of the building design process. Design optimization is required to promote higher building performance with less cost and less environmental impact [1]. Design process enhancement could be achieved by optimizing the material utilization within the structural components. Reinforced masonry construction has the known benefits of better fire protection, structural durability, energy efficiency and cost reduction [2]. However, there is still a widespread misconception that masonry structures cannot possess the required ductility to resist earthquake loads due to the poor performance of unreinforced masonry buildings in earthquake events. Reinforced Masonry Shear Walls with boundary elements (RMSW+BE) have the added benefit of enhanced ductility by providing the required space for two layers of vertical reinforcement and confinement hoops. Confinement hoops provide the support for vertical reinforcement to delay the buckling, and the grout core continues to carry stress at higher strain levels [3].

Reinforced masonry shear walls (RMSW) are fully or partially grouted concrete masonry blocks reinforced with steel bars in vertical and horizontal directions. They are used in medium to high rise buildings as a seismic force-resisting system in moderate seismic risk regions. Shear wall systems are used in buildings due to their ability to provide the required stiffness and strength to resist the lateral loads induced by wind or seismic excitations. Several research studies were conducted to understand better the seismic response of RMSW [4]–[9]. These studies showed that the specimens controlled by the flexure mode of failure provide a higher ductility and lower strength degradation at higher drift levels. However, the masonry block shape restricts the placing of the confinement and vertical reinforcements, resulting in premature buckling of vertical bars or crushing of the grouted core. Therefore, increasing the confinement in the wall's toe zones will increase the ultimate compressive strain at the boundary elements zone and increase the ultimate curvature capacity. It is also expected to delay the buckling of

vertical reinforcement and the crushing of the grouted core, which will increase the ductility and enhance the overall seismic response of RMSW [10].

Typical rectangular RMSW has a geometry restriction; by having one layer of vertical reinforcement, which does not allow adding confining hoops to the end zone. Many confinement methods were proposed by researchers, e.g., confinement plates, confinement comb and spiral ties [11]–[13]. Another alternative confinement method is to add boundary elements to the wall's end zones [12]. Boundary elements provide the required space to have two layers of vertical reinforcement, which allows for adding confinement hoops.

Several research studies were conducted to better understand the seismic response of RMSW [8], [14]–[18]. These studies showed that the flexure mode of failure provides a high level of ductility and small strength degradation at large drift levels. Therefore, to enhance the ductility and the overall seismic response of RMSW, there was a need to confine the toe zones in the wall to delay the buckling of vertical reinforcement and to increase the grouted masonry ultimate compressive strain in order to increase the ultimate curvature capacity.

Shedid et al. [8] tested seven RMSWs with three different end configurations (rectangular, flanged, and end-confined). The results showed that flanged and end-confined boundary elements increased the wall's ductility by 39% and 106%, respectively. Also, the measured drifts at 20% drop from peak load were 1.0%, 1.5% and 2.0% for the rectangular, flanged and end-confined boundary elements walls, respectively. Moreover, a 40% reduction in the required vertical reinforcement in flanged and end-confined walls compared to rectangular walls was achieved. Banting [14] tested fully grouted half-scale RMSW+BE to investigate the effect of confinement on the drift capacity and vertical reinforcement buckling of the walls. The results showed that confining delayed the buckling of vertical reinforcement and delayed the crushing of the grout core.

Moreover, face shell spalling in the compression toes did not cause an abrupt drop in resistance. Thus, these research efforts showed that adding boundary elements at RMSW ends enhances the wall ductility and limits wall toes damage. Additionally, introducing a boundary element at the wall ends provides out-of-plane stability, decreases the required length of the compression zone, and increases the curvature capacity at maximum load. All these advantages

can be achieved with even less vertical reinforcement ratio compared to RM rectangular walls [8].

Currently, the boundary elements are made from regular stretcher units and are restricted in size and vertical and transverse reinforcement ratios. Also, they have many constructability issues; for example, masonry units and hoops should be laid in a certain sequence, which consumes lots of time and workforce. In addition, to have hoops spacing less than the block unit height, a large number of cutting operations need to be done, as can be seen in Figure 1.1.
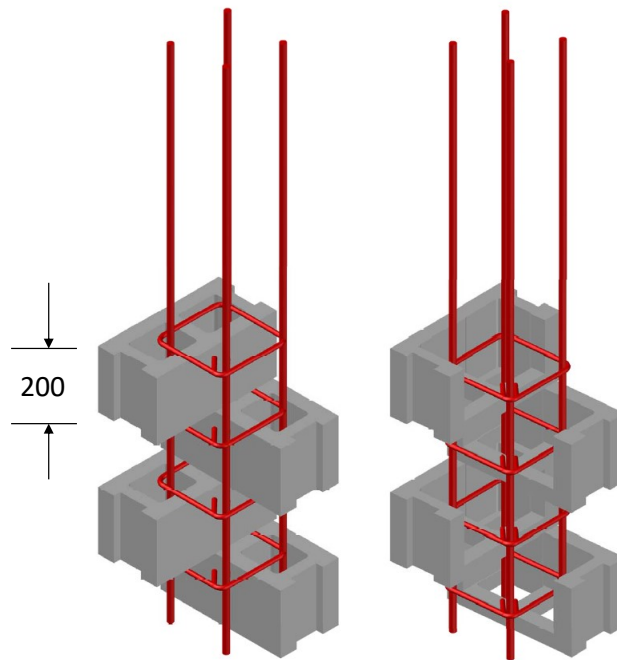
Figure 1.1: Number of cutting operations for the web and the flange of the stretcher unit

Due to the geometry restrictions of the stretcher units, the spacing between the transverse reinforcement hoops spacing is limited and does not provide the required vertical reinforcement buckling prevention spacing. Also, using stretcher blocks restricts the boundary element's shape to the square (to be practical) and restricts the number of vertical reinforcement bars. Moreover, the confined core in the boundary elements made by using stretcher units is a mix of three materials; grout, stretcher block, and mortar which makes it a non-homogeneous material. This, in turn, makes it hard to control the boundary element properties in practical applications. Construction and testing of RMSW+BE with a new configuration of boundary element was introduced in collaboration with the masonry industry in Canada, namely, the Canadian Concrete

Masonry Producers Association (CCMPA), Canada Masonry Design Centre (CMDC), and L'Association des Entrepreneurs en Maçonnerie du Québec (AEMQ) by Albutainy et al., 2017 [19] to ensure its practicality for future manufacturing and its use in the construction industry. The current CSA S304-14 [20] and NBCC 2015 [21] reflected the recent research efforts to improve the design of reinforced masonry (RM) walls by proposing a new ductile RM wall category with a ductility-related force reduction factor (R_d) of 3.0. As a result, ductile RMSW was considered an adequate lateral force resisting system for high-rise masonry buildings with heights up to 40 m in zones with seismic hazard index larger than 0.75 [21]. However, the literature is lacking experimental investigation for RMSW with heights close to 40 m.

1.2 Research significance and motivation

The latest research efforts in the area of seismic behaviour of RMSW were reflected in the current CSA S304-14 by introducing a new type of ductile RMSW with a ductility reduction factor of 3.0. Despite the research advancement, there are still some limitations associated with the current CSA S304-14. The current standards limit the ultimate compressive crushing strain used in the design to 0.0025 instead of 0.0035, compared with reinforced concrete. This has an impact of underestimating the ultimate curvature of the wall's section and the predicted ductility. However, CSA S304-14 allows increasing the design compressive strain up to a maximum value of 0.008 (clause 16.10.2), when satisfying two main conditions shown in Figure 1.2 (a and b). The first condition is to provide buckling prevention reinforcement for the vertical bars in the boundary element. The second condition is for the minimum length of boundary elements to the maximum of $c(\varepsilon_{mu} - 0.0025)/\varepsilon_{mu}$, c/2, or (c - 0.1$l_w$), where c is the compression zone depth, ε_{mu} is the used ultimate compression strain l_w is the wall's length. The second condition is required to ensure that the ultimate compression strain outside the confined area does not exceed 0.0025.

Clause 16.11.4 of CSA S304-14 [20] provides the confining hoops vertical spacing "S" required to provide confinement to the boundary elements. The minimum required spacing "S" is the least of six times the vertical bar diameter, 24 times the confining hoop diameter and one-half of the least boundary element dimension. The maximum diameter allowed by CSA S304-14 to be used in vertical reinforcement is 25M (clause 12.2). Considering clauses 16.11.4 and 12.2, the spacing required for confining hoops will range from 96 mm to 150 mm in most cases. The

stretcher unit height used to form the boundary elements is approximately 200 mm. In order to provide the required buckling prevention reinforcement, a large number of cutting operations for the web and the flange of the stretcher unit are required as shown in Figure 1.2. Increasing the cutting operations will increase the construction time, manpower and wasted material. In addition, cutting the stretcher unit in many locations may initiate unwanted hairline cracks that may weaken the masonry unit and break it off in several areas.
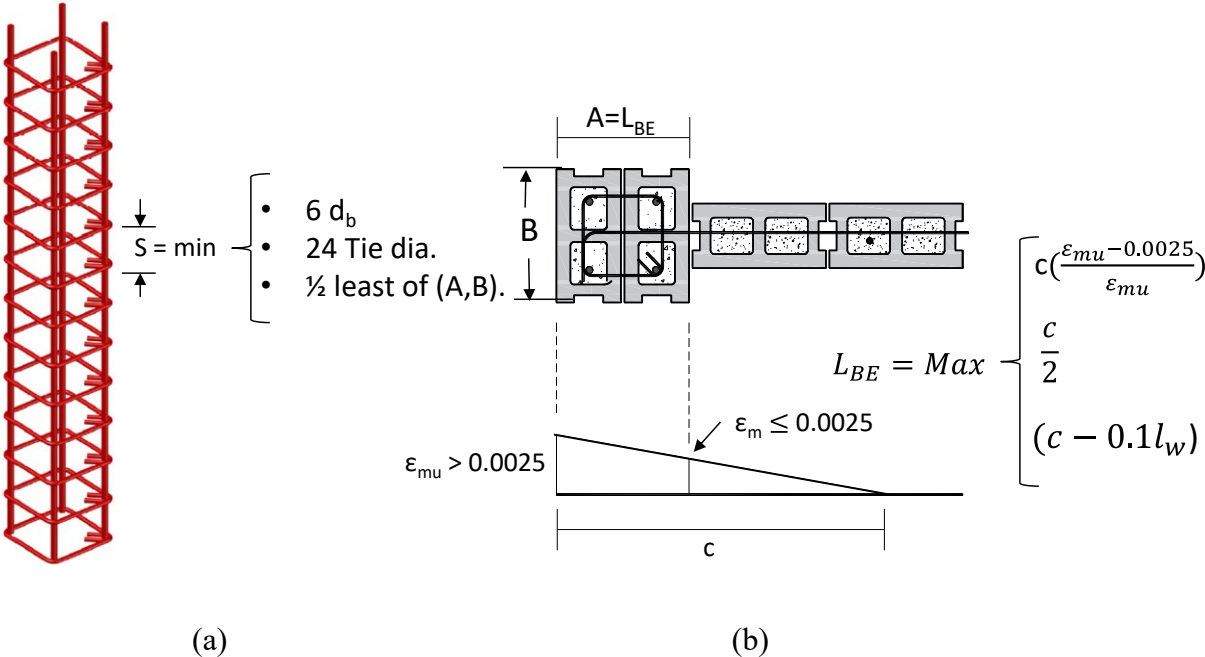
Figure 1.2: CSA S304-14 (a) hoop spacing requirements, and (b) increased compression strain requirements

When using stretcher units, the boundary element is limited to a square shape, since increasing the BE length will require increasing the number of stretcher units, which makes it complicated for construction. Additionally, using the stretcher units to form the BE limits the number of vertical reinforcement bars to four. Thus, there is a need to have a BE configuration that can provide the flexibility to control the BE length and the number of vertical reinforcement bars in a practical and economical way. The square form of the boundary element, in full-scale, is approximately 400 × 400 mm. These dimensions restrict the design options required by CSA S304-14 [20] to meet the minimum boundary element length. Furthermore, boundary elements formed by stretcher units are a mix of three materials, grout, stretch block, and mortar, which makes it non-homogeneous and challenging to control its properties in practical applications. In

5

addition, when using stretcher units to form the boundary elements, the masonry units and hoops should be placed in series, which consumes more time and manpower.

Providing and testing a new boundary element system satisfies the code requirements to provide the required strength and ductility to ductile RMSW buildings in the notes in cl. 16.10.2, which states that:

"Designers should provide sufficient additional construction review beyond that normally required in reinforced masonry construction to ensure that details related to creating high ductility in the plastic hinge region of structures employing confined masonry in compression are constructed in accordance with the contract documents" [20].

Another related aspect is the practicality of the system and what the masonry industry needs. From this point of view, the use of stretcher blocks requires more effort and time from the mason to keep installing the transverse reinforcement hoops from the top of vertical reinforcement bars. There had been no experimental research studies on the response of high-rise ductile RMSW+BE under simulated earthquake event prior to the research presented in this thesis. The majority of RMSW+BE experimental testing have been conducted on low-rise walls.

The motivation of this research is to provide a practical RMSW system that can overcome the limitations that arise from the current practice. In addition, many experimental works have been carried out to better understand the non-linear response of reinforced concrete (RC) and reinforced masonry shear walls (RMSW) due to seismic excitation. However, the cost and time associated with the experimental work are standing as a barrier toward conducting enough experiments to better understand the response of RC and RMSW. This explains why there was a need to develop reliable numerical models that can provide a reliable prediction of the RC/ RMSW non-linear response.

The C-shaped boundary element units are shown in Figure 1.3. Here, the boundary element is formed using two C-shaped masonry units facing each other and the steel cage is installed as one peace. C-shaped BE has the advantage of providing more homogenous grouted core, flexibility in selecting the boundary element size and the amount of vertical and transverse reinforcement.

6
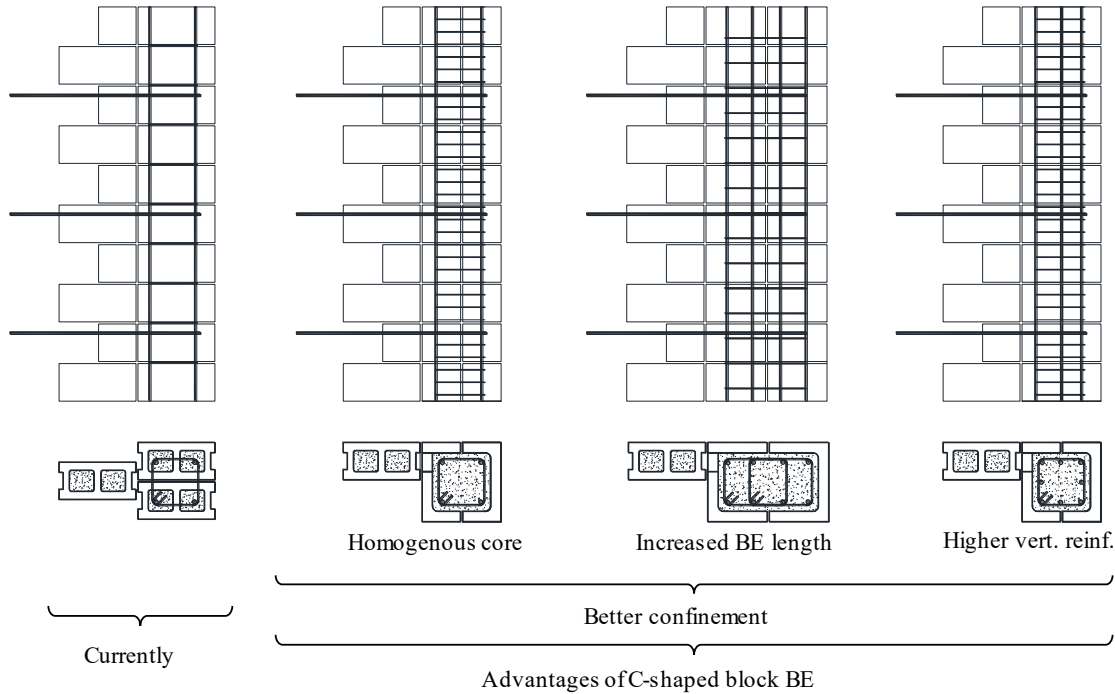
Figure 1.3: Advantages of C-shaped block boundary elements

1.3 Research objective

The research objective of this study is to provide engineers with RMSW configurations that allow them to customize the boundary element's size, the distance between transverse reinforcement hoops, and the grout strength. This research is intended to push the boundaries by testing the plastic hinge zone in a 12-storey RMSW building having an aspect ratio of 10.6, whereas the RM shear wall with highest tested aspect ratio before commencing this research work in 2016 was 4.5 [22]. Furthermore, this study is part of a program at Concordia University that aims to develop a new boundary element block that allows designers to decrease the spacing between hoops in the boundary elements and thus increase the confinement ratio. This new boundary element block eliminates the limitations associated with regular concrete blocks (i.e., stretchers) utilized in prior studies.

1.4 Hypotheses statement

1. A stronger boundary element can provide more out-of-plan support to the web; thus, there is a potential to increase the web's un-supported height recommended by CSA S304-14.
2. Increasing the confinement in the boundary element by decreasing the spacing between the confinement hoops will enhance the seismic response of the RMSW+BE.

3. Increasing the length of the boundary elements can enhance the seismic response of the RMSW+BE and can utilize the increased value of the ultimate crushing strain recommended by CSA S304-14.

4. Increasing the vertical reinforcement ratio of the larger boundary elements can enhance the ductility of the RMSW+BE.

5. There is a potential to increase the ductility reduction factor for ductile RMSW recommended by NBCC 2015.

1.5 Specific objectives and scope of work

This study seeks to generate experimental data on the flexural behaviour of RMSW+BE by testing walls with larger aspect ratios than those previously evaluated. Additionally, this study aims to develop a testing setup and verify its performance and assess the effect of the boundary element's confinement ratio on the RMSW seismic response. Finally, the experimental results will be used to create and evaluate a numerical model capable of simulating the behaviour of the RMSW. To achieve the above objectives, the scope of work needs to include the following tasks:

1. Developing a new system/configuration for RMSW with C-shaped masonry units.

2. Developing and designing test setup to meet the research terminal objective and test the above stated hypotheses.

3. Investigating the potential to increase the web un-supported height recommended by CSA S304-14 (Hypothesis 1)

4. Investigating the effect of increasing the confinement in the boundary elements on the seismic behaviour of RMSW+BE and its failure mode (Hypothesis 2).

5. Investigating the effect of changing the length of the boundary elements on the seismic response of the RMSW+BE (Hypothesis 3).

6. Investigating the effect of changing the vertical reinforcement ratio of the boundary elements on the seismic response of the RMSW+BE (Hypothesis 4).

7. Investigating the potential to increase the ductility reduction factor for ductile RMSW recommended by NBCC 2015 (Hypothesis 5).

8. Developing and validating a numerical model that can simulate the behaviour of the tested walls.

9. Using the validated numerical model to study the effect of the eccentricity of the boundary elements with respect to the web by comparing 2D and 3D models.

1.6 Methodology

The proposed research project is divided into experimental and numerical investigations. As shown in Figure 1.4, the experimental work will start with designing the walls based on the selected building plan and location. The next step is to design and build the test setup based on the predicted response of the designed walls. The outcome from the experimental investigation and constitutive properties of the material obtained from tests will be used to validate the numerical model.

1.7 Test Program

This study is part of a large research program conducted at Concordia University. In this research program, twelve wall specimens were investigated to establish the effect of the following variables on the seismic response of RMSW with C-shaped boundary elements: the boundary element vertical reinforcement ratio, the boundary element confinement ratio, the size of the boundary element, the axial load ratio, the vertical reinforcement lap splice, the type of blocks used to form the boundary elements, and the wall aspect ratio. In this thesis, six walls specimens were tested to address the first three parameters. In order to achieve the objectives of this research work, an experimental setup was designed along with the test control by the author to allow testing RMSW+BE with high aspect ratio and synchronize the testing actuators in a controlled fashion. In addition, a 3D model was developed to investigate the effect of the recommended BE eccentricity with respect to the wall's web on the seismic response of the tested walls. This aspect has never been investigated before.

1.8 Expected contributions to knowledge

The knowledge expected to be gained from this study will contribute to improving the seismic hazard safety of mid-rise masonry buildings in Canada. The end-user and stakeholders in the masonry design and building industries would benefit from this thesis' primary findings, as follows: The properly designed and performed experimental and numerical work will improve the way reinforced masonry boundary elements are currently built in RMSW+BE. By creating an experimental setup that enables testing the plastic hinge zone in a 12-story RMSW+BE building

with an aspect ratio of 10.6, as opposed to the RM shear wall with the highest tested aspect ratio of 4.5. This study pushes the boundaries of what is currently possible. The research outcome is expected to provide in-depth knowledge of the seismic performance of RMSW+BE, with the newly proposed boundary element formed with C-shaped units. Using a validated numerical model, the effect of boundary element eccentricity with respect to the web, and the effect of changing the boundary element confinement reinforcement spacing will be established.

1.9   Thesis layout

Six chapters (including this one), a list of figures and tables, an appendix, and references make up the dissertation. The chapters provide and discuss all the experimental, numerical, and analytical work completed. The following is the content of the chapters:

- Chapter 1: presents the background, research significance and motivation, research objectives, and a description of the thesis layout.
- Chapter 2: provides a literature review of RMSW's failure modes, the concept of ductility and ductility reduction factor, the determination of plastic hinge, previous experimental research work on RMSW and masonry prisms and the numerical modelling for RMSW. Finally, a summary of the literature review was provided.
- Chapter 3: provides a detailed description and the development of the experimental program and setup including the test control system.
- Chapter 4: addresses the effect of changing RMSW with C-shaped boundary element unsupported length. In addition, the constructability advantages of utilizing the proposed c-shaped boundary elements were addressed. The test results for three RMSW+BE are presented and discussed. The three tested walls varied in the amount of confinement reinforcement in the boundary elements. The results of this study demonstrated the great potential of RMSW with masonry boundary elements (MBEs) formed by the proposed C-shaped masonry blocks to provide the strength and ductility required for lateral force resisting systems in medium to high rise masonry buildings.
- Chapter 5: describes the construction and testing of three half-scale RMSW+BE specimens characterized by flexural dominance under reversed cyclic moment and lateral loading. The boundary elements of the wall were different in terms of their size and vertical reinforcement ratios. The findings of this work revealed that employing C-shape

masonry units to construct the boundary elements effectively overcame the constructability limits imposed by the use of stretcher units.

- Chapter 6: develops an experimentally validated numerical model to investigate the effect of changing the confinement reinforcement ratio in reinforced masonry wall boundary elements on its seismic response and failure mode. The model was validated against experimental results from three different experimental programs. A comparison between the results obtained from the 2D model and the 3D model was carried out to establish the effect of the eccentricity in the boundary element on the accuracy of the 2D model results. In addition, the effect of the used loading protocol (cyclic vs monotonic) on the wall curvature was also investigated.

- Chapter 7: provides a summary of the performed research work, the main findings and conclusions, and the recommendations for future work.

- Appendix A: Calculating the critical buckling load for W2-C$_S^{30}$ boundary element.
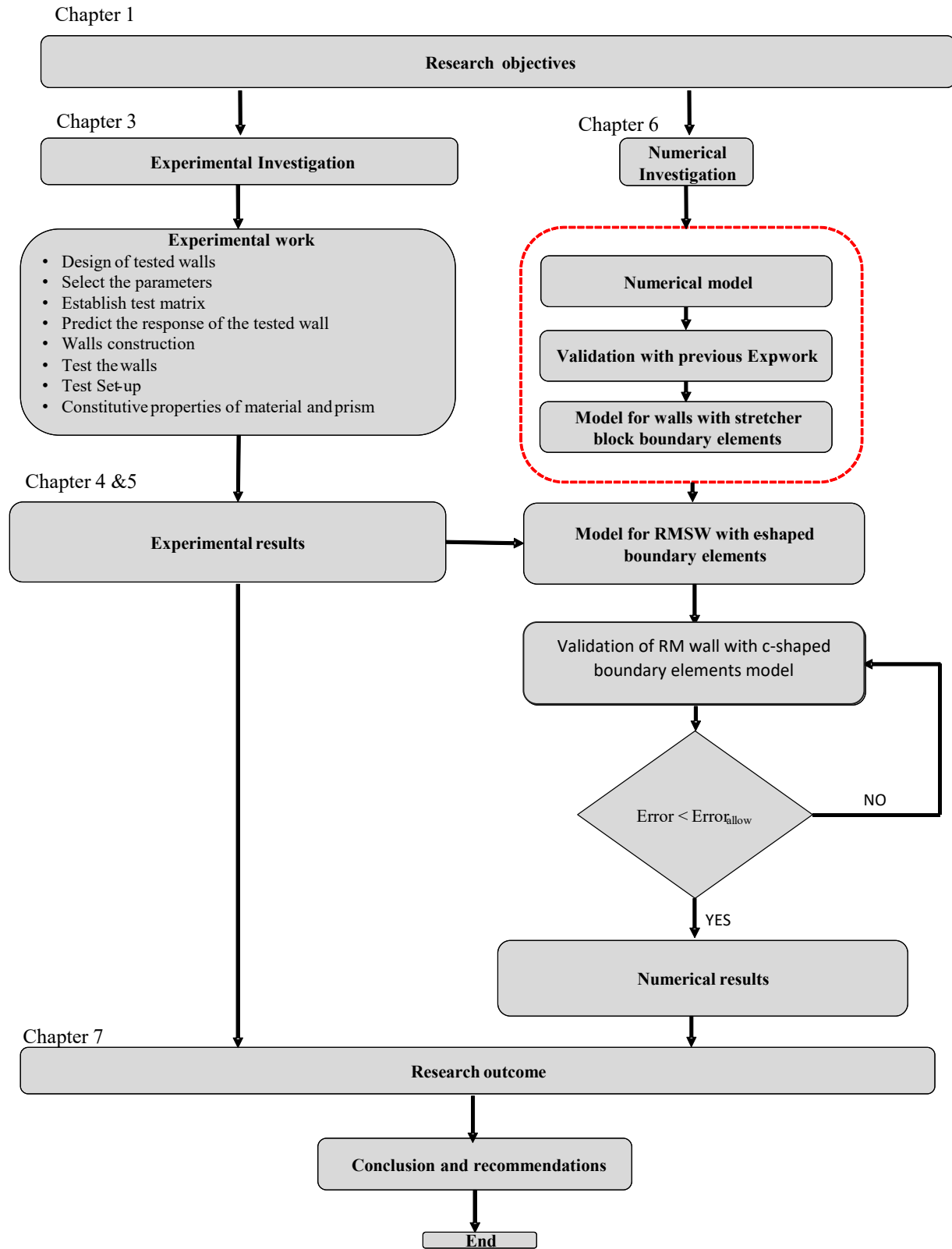
Figure 1.4: Research methodology

Chapter 2

Literature Review

This chapter provides a critical review of previous research on reinforced masonry shear walls (RMSW). RMSW's failure modes are discussed in section 2.1. The concept of ductility and ductility reduction factor are discussed in sections 2.2 and 2.3, respectively. The determination of plastic hinge length is addressed in section 2.4. Sections 2.5 and 2.6 present a summary of previous experimental research work on RMSW and masonry prisms. Finally, the numerical modelling for RMSW is discussed in section 2.7. Concluding remarks and identification of research gaps in the state-of-the-art are identified in section 2.8.

2.1 Shear wall failure modes

There are many modes of failure for cantilever shear walls. These modes are flexural, shear, rocking and sliding as shown in Figure 2.1. Paulay and Priestley [15] indicated that the in-plane main failure modes of shear walls are the flexural mode, shear mode and sliding mode. Also, they showed that the mode of failure is highly dependent on the wall's aspect ratio (H/L). The out-of-plane failure modes are mainly buckling, lap splice or anchorage slippage. Flexural failure is commonly favoured in seismic design since it corresponds to the wall ductile behaviour (Shing et al., [23]; Paulay and Priestley [15]; Shedid, [12]). Flexural mode of failure is characterized by tensile yielding of vertical reinforcement, toe-crushing and the formation of plastic hinge zones. This type of failure is also associated with a high level of energy dissipation.

The shear failure, which is not a favourable mode of failure, is due to the brittle behaviour and quicker strength degradation of the shear wall after reaching the maximum strength [15]. It can be characterized by diagonal or step tensile cracks. In this mode of failure, no yielding in the vertical reinforcement, which is the main source of energy dissipation in laterally loaded cantilever shear walls, is observed [16]. Shear failure depends on the level of axial stress, the strength of the masonry, and the aspect ratio of the wall [17]. Sliding failure occurs when sliding planes form along horizontal or diagonal cracks [24]. Also, it happens on the plane between the wall and the footing if there is not enough friction as shown in Figure 1(d).
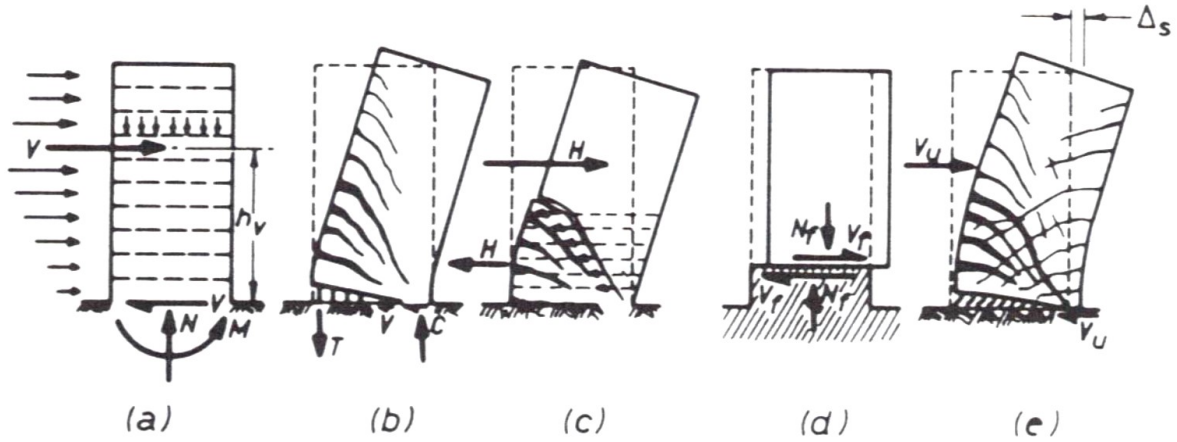
Figure 2.1 Typical cantilever shear wall failure modes. (a) Typical applied loads on a cantilever wall, (b) Rocking failure, (c) Shear failure, (d) Sliding failure, and (e) Flexural failure [15]

2.2   Ductility

Ductility ratio μ_Δ can be considered as the most effective way to determine the structure's ductility demand and capacity [25]. For the cantilever structure shown in Figure 2.2, the ductility ratio can be expressed as the ratio between the ultimate displacement (Δ_u) and the yield displacement (Δ_y) at the top of the wall:

$$\mu_\Delta = \frac{\Delta_u}{\Delta_y} \hspace{5cm} \text{Equation 2-1}$$

The total displacement (Δ_u) will result from the summation of the yield displacement (Δ_y) and the plastic displacement (Δ_p) shown in Figure 2.2.

Structures can be classified in terms of their design ductility level. Figure 2.3 shows the relationship between the strength and the displacements for different design approaches, where S_E is the strength required to resist earthquake force and Δ is the corresponding displacement. It can be seen that while increasing the ductility level, μ, results in a decrease in the lateral design force and the yield displacement, it also causes an increase in the system's plastic displacement.
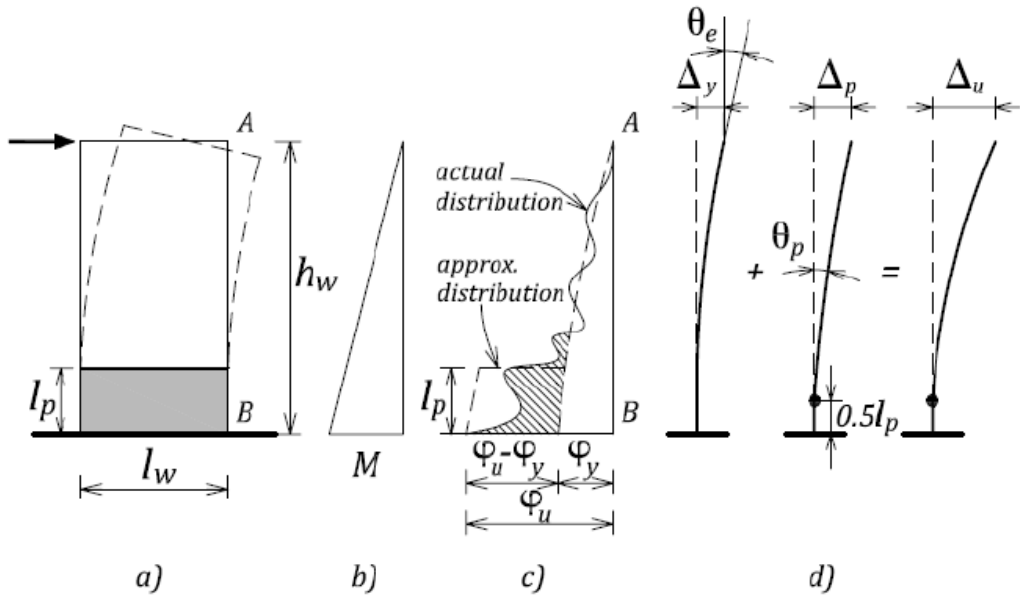
Figure 2.2: Moment, curvature and deflection relationships for a prismatic reinforced concrete or masonry cantilever [15]
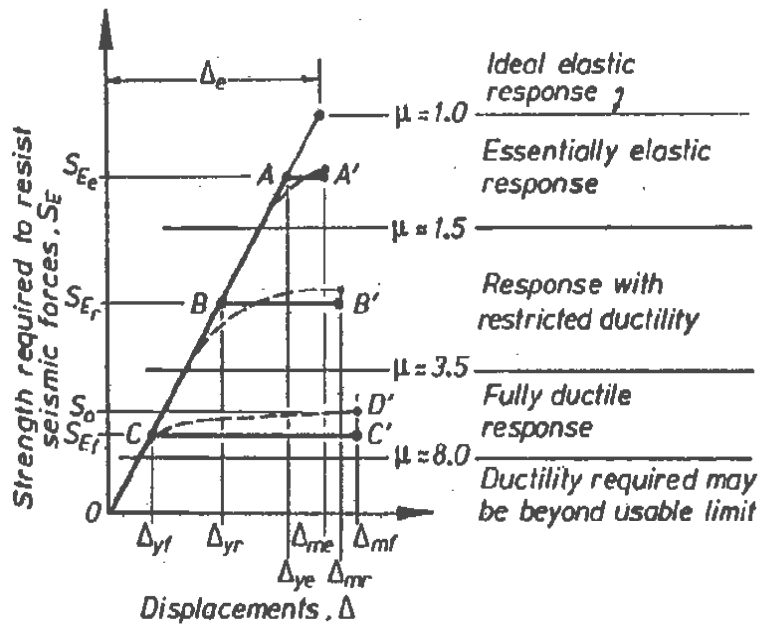
Figure 2.3: Relationship between strength and ductility [15]

15

2.2.1   Elastic response

Buildings with high functional importance (nuclear reactors, hospitals...) are designed to develop a lateral strength that ensures that they will remain elastic to reduce the level of damage in these vital buildings. In this case, the building design is based on 'strength design' concept. This implies that the plastic state could be achieved in the critical sections without any significant inelastic deformation. This can be achieved through the material strength reduction factors used in the design to provide extra protection and to ensure no development of inelastic deformations. In this case, a high level of detailing for reinforcement and section dimensions is not needed. However, a certain level of ductility can be maintained even with this design philosophy. The elastic response can be shown in Figure 2.3 by the OAA' curve [15].

2.2.2   Ductile response

Buildings of normal importance are designed for forces less than required to have an elastic response [15]. This leads to more inelastic deformation, which needs a more ductile structure system to resist these forces and accommodate the large inelastic deformation. Therefore, these buildings have to be designed and detailed to allow the building to deform in the plastic range. This level of detailing will vary with the required level of ductility. The ductile response can be divided into two main subcategories: fully ductile structures (Figure 2.3 by the line OCC' and OCD'), and structures with restricted ductility shown in Figure 2.3 by the curve OBB'). It is worth mentioning that there are no restricted limits for structures with full or restricted ductility since the transformation from one system to the other takes place gradually.

Studies carried out by Priestley [4], Paulay et al. [5], Sveinsson et al. [26], Tomazevic et al. [27], Shing et al. [16], Seible et al. [28], Voon and Ingham [29], Miller et al. 2005 [30], Shedid et al. [12], and Banting et al. [31] showed that the flexure mode of failure provides a high level of ductility and small strength degradation at large drift levels.

2.3   Force reduction factors

Reducing the design forces will lead to more inelastic deformations in the structure. This will result in yielding in the vertical reinforcement and crashing in the concrete or masonry. This inelastic deformation can be accepted subject to ensuring that the structural system will not experience a strength degradation in the inelastic zone and has an acceptable response.

Moreover, displacements and damages in the structure have to be well controlled. The advantage of inelastic response, besides the cost-effectiveness, is the increase of the structure's natural period. Such an increase will decrease the response peak acceleration, which will reduce the damage to the building components. This behaviour can be described as ductile behaviour, which must be ensured for the full duration of the earthquake in all directions.

Some research work has been carried out to investigate the relation between the response modification factor and the ductility of the structure, e.g., Newmark and Hall [32], Paulay and Priestley [15], Chopra [33] and Drysdale and Hamid [34]. The results of these investigations showed a relation between the structure period and the principal used to calculate the response modification factor R as shown in Figure 2.4(a). For structures with a period (T) greater than the period that corresponds to the peak elastic spectral response, it was observed that the maximum displacements achieved by both elastic and inelastic systems are very similar, given that the elastic system stiffness is the same as the inelastic system initial stiffness, as shown in Figure 2.4(b). In this case, the ductility ratio is given by:

$$\mu = \frac{\Delta_m}{\Delta_y} = R \qquad\qquad\qquad \text{Equation 2-2}$$

where R is the lateral force reduction factor. This observation is known as an equal-displacement principle.

For structures with a period T shorter than the period that corresponds to the peak elastic spectral response, it was observed that the displacement ductility demand is higher than the lateral force reduction factor R. The area under the elastic and the inelastic curves in Figure 2.4(b) are equal in dissipating the same energy. In this case, the ductility ratio is related to R by the following relation:

$$\mu = \frac{R^2+1}{2} \qquad\qquad\qquad \text{Equation 2-3}$$

This observation is known as the equal-energy principle.
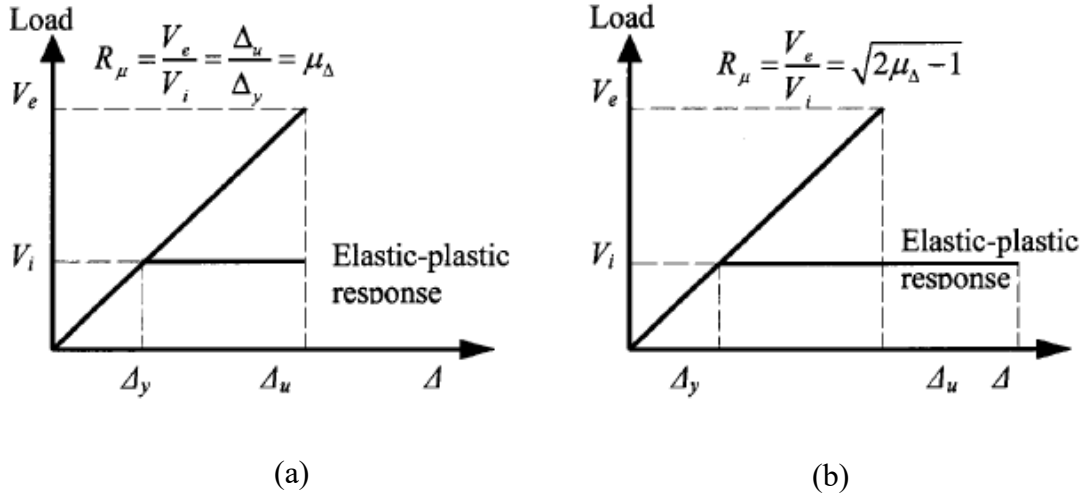
Figure 2.4: Relationship between ductility and force reduction factor [35]

2.4 Plastic hinge length

The plastic hinge zone in a shear wall is where the inelastic rotations are concentrated toward the wall base. Determining the plastic hinge zone height is important to determine the shear wall's ultimate displacement. The presence of the grout and reinforcement enhances this behaviour by having continuity in the stress flow and by making the behaviour of fully grouted RM walls similar to RC walls [36]. In this sense, the application of the plastic hinge equations developed for reinforced concrete (RC) shear walls are applicable to RMSW as well. Many researchers introduced equations to calculate the plastic hinge length for concrete and masonry structural walls, e.g., Paulay and Uzumeri [37], Paulay and Priestley [15], Priestley and Kowalsky [38], Bohl and Adebar [39], Shedid et al. [40], and Banting [14].

Table 2.1 summarizes the plastic hinge height equations suggested in the literature, in which l_w is the wall length, h_w is the wall effective height, d_p is the vertical bar diameter, f_y is the yield strength of the vertical bars, f_u is the ultimate strength of the vertical bars, p is the applied axial load, f_c' is the specified compressive strength for concrete or masonry, and A_g is the gross area of the shear wall. In order to investigate the difference between the proposed equations, the following values were assumed. These values represent the characteristics of a reinforced masonry shear wall with the same dimensions as those of the six scaled walls that will be tested in this thesis:

18

$l_w=$ 1715   mm

$h_w=$ 12750   mm

$f_y=$ 400   MPa

$f_u=$ 500   MPa

$f'_c=$ 20   MPa

$d_p=$ 12   mm

$A_g=$ 154350   mm^2

$P=$ 231525   N

Table 2.1: Comparison between plastic hinge equations reported in the literature

	Plastic hinge height (l_p) equation	Proposed by	Calculated l_p in mm
1	$0.5l_w + 0.05h_w$	Mattock (1967)	1495
2	$0.4l_w + 0.05h_w$	Paulay and Uzumeri	1323.5
3	$0.2l_w + 0.075h_w$	(1975)	1299.25
4	$0.08l_w + 0.022d_bf_y$	Paulay and Priestley (1992)	242.8
5	$0.2l_w + 0.022h_w$	Priestley and Kowalsky (1998)	623.5
6	$0.2\left(\dfrac{f_u}{f_y} - 1\right)h_w + 0.1l_w + 0.022d_pf_y$	Priestley et al. (2007)	914.6
7	$(0.2l_w + 0.05h_w)(1.0 - \dfrac{1.5P}{f'_cA_g})$	Bohl and Adebar (2011)	870.2

Figure 2.5 shows the plastic hinge height estimated by different equations in the literature. The expressions shown in Table 2.1 are based on regression analysis of either experimental, numerical or hybrid studies with variation in mechanical and structural parameters. The control variables in the aforementioned equations are moment gradient and tensile strain penetration through the bond-slip mechanism inside the foundation. It can be seen that these equations provided a wide range of the predicted plastic hinge height. It should be noted that these equations do not consider other relevant parameters, such as the wall configuration, the existence of boundary elements, as well as the vertical, horizontal and confinement reinforcement that may

affect the prediction of the plastic hinge height. Banting [14] proposed Equation 2-3 to predict the plastic hinge height, taking into consideration the effect of the ratio between the vertical and horizontal reinforcement and its spacing:

$$l_p = 0.25h_w + 0.5l_w\sqrt{(\frac{A_{sv}f_{yv}}{S_v})/(\frac{A_{sh}f_{yh}}{S_h})} \leq \min{(1.5l_w, h_w)} \qquad \text{Equation 2-4}$$

where A_{sv} f_{yv} and A_{sh} f_{yh} are the product of the areas of the vertical and horizontal steel and their respective yield strength. The parameters S_v and S_h are the spacing between the vertical and horizontal reinforcement, respectively.

Plastic hinge height (mm)
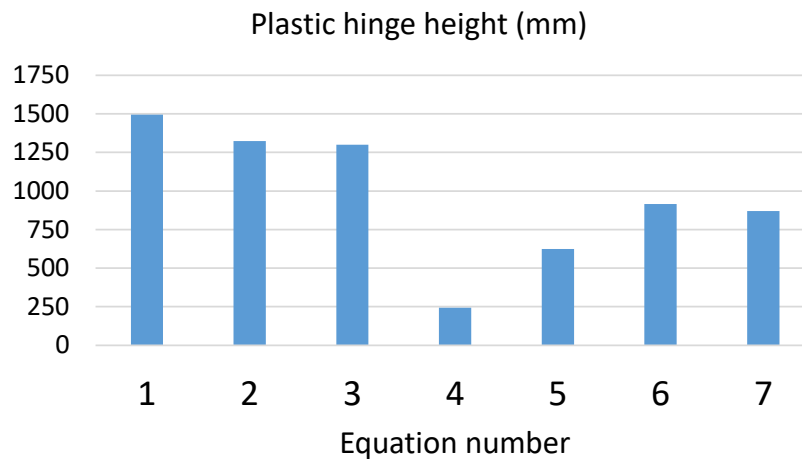
Figure 2.5: Plastic hinge height calculated based on equations in Table 2.1

2.5 Masonry Shear Wall Experimental work

In 1971, Williams [41] tested four fully grouted RMSWs under static loading procedure and four walls under dynamic loading procedure. The experimental setup is shown in Figure 2.6. Williams concluded that it is possible to design RMSW with ductile behaviour. He established that low service load, low vertical reinforcement ratio, and high aspect ratio promote the ductile behaviour of the wall. He also recommended confining the corner material to prevent buckling of the vertical reinforcement.

In 1974, Priestley and Bridgeman tested eighteen RMSW under slow cyclic loading and dynamic loads [42]. They showed that satisfactory ductility could be achieved from the RMSW if the horizontal reinforcement is capable of carrying the full shear load, and the first few courses

are confined within the thin steel plates in the bed mortar joints, in reigns where crushing is expected. In addition, the test results revealed that strain hardening in the vertical reinforcement increased the flexural capacity of the wall by 14%, compared to the theoretical calculations.

(a)   (b)
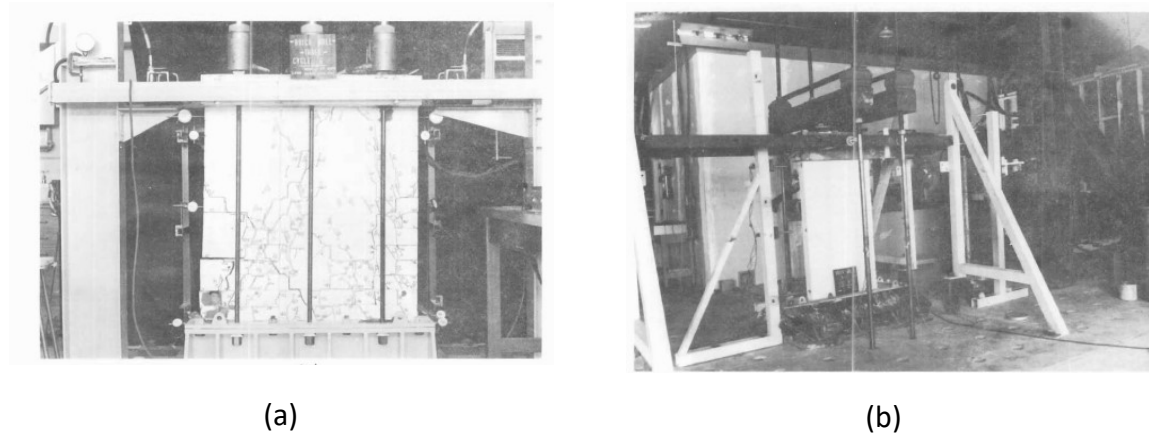
Figure 2.6: Tested walls by Williams 1971, a) Static test, and b) Dynamic test

Later in 1982, Priestly and Elder [43] tested three slender reinforced masonry walls detailed in Figure 2.7. The walls were scaled to 1:0737 for four to five stories high. In these walls, the effects of changing the axial load, the existence of confinement plates placed in mortar bed joints, shown in Figure 2.8, and the presence of lapped starter bars in the plastic hinge zone were examined. They concluded that lapped splices have the effect of shortening the plastic hinge zone, and the existence of confining plates improves the overall response of RMSW.

In 1988, Takashi et al. [44] investigated the strength and the deformation capacity of twenty-two walls under double curvature deformation and constant axial stress. The results showed that increasing the axial stress increases the shear strength and the deformation capacity for walls failed in shear. Additionally, the deformation capacity of walls that failed in flexure was shown to increase by increasing the shear reinforcement and confining the compression zones.

Shing et al. (1988 and 1989) [16], [7] tested sixteen RMSW to investigate the effect of changing the axial stress and vertical reinforcement ratio on the lateral resistance of RMSW. The experimental setup is shown in Figure 2.9. The results of these tests indicated that by providing the right amount of horizontal reinforcement, the brittle shear failure could be avoided. In addition, it was shown that the amount of horizontal and vertical reinforcements has influence on the energy dissipation and ductility of walls that fail in shear. It was also concluded that the first

21

major diagonal crack depends on the tensile strength of the masonry. These experiments showed that reducing the axial stress leads to increasing the wall ductility. Brunner and Shing tested three fully grouted masonry walls with a low aspect ratio [45]. The only parameter that was changed in these walls was the aspect ratio (H/L). The data generated in this work was used to develop an analytical model to evaluate the shear and flexural strength of the wall.
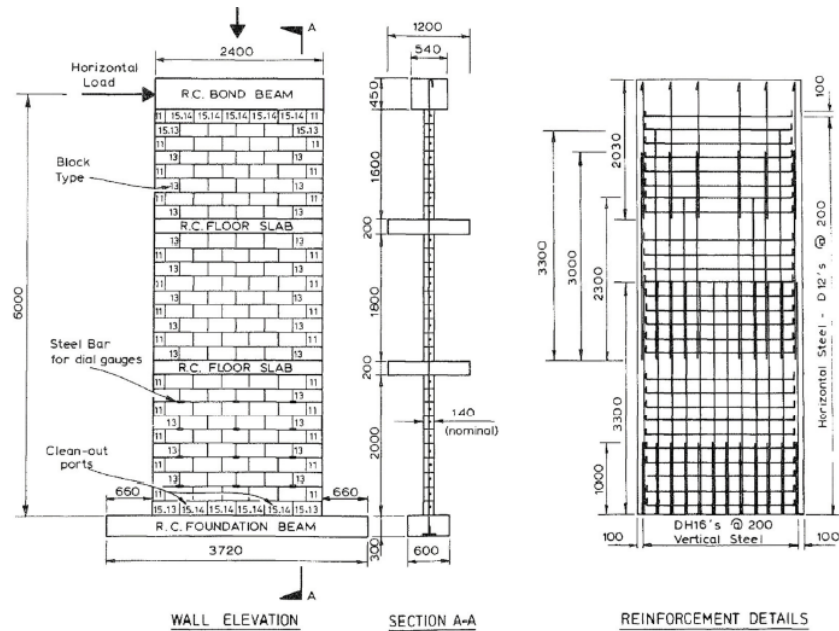
Figure 2.7: Wall dimensions and reinforcement test by Priestly and Elder [43]

| (a) | (b) | (c) |
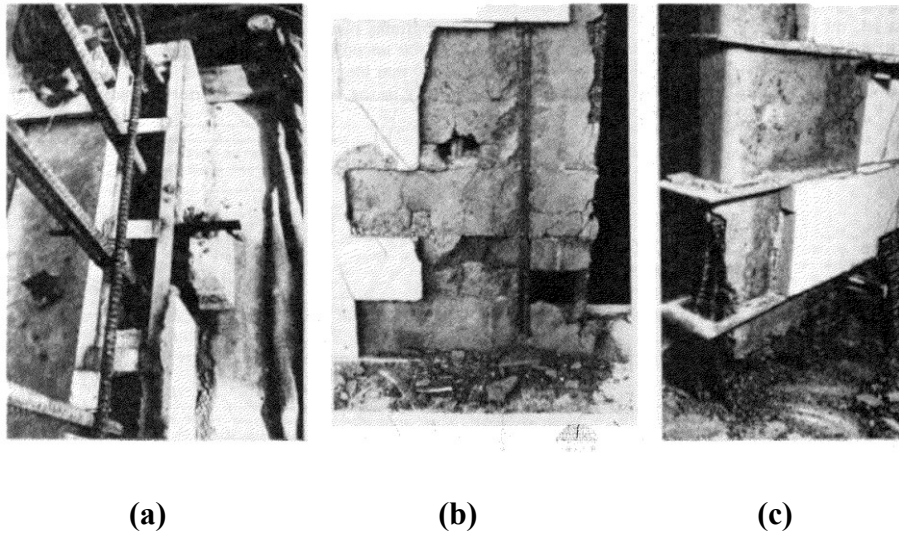
Figure 2.8: Confinement plate a) placing of confinement plates, b) unconfined wall after two cycles μ=3.9, and c) confined wall after two cycles μ =5.7 [43]
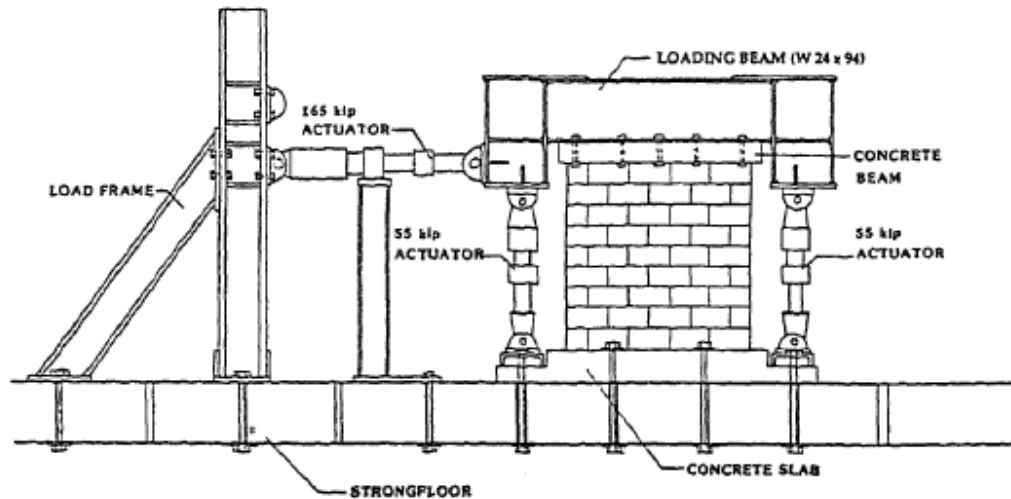
Figure 2.9: Test setup by Shing et.al. [44]

In 1990, Sajjad [46] investigated the behaviour of four masonry shear walls using three types of confinement: hoop reinforcement, comb confinement reinforcement, and spiral cage confinement. The fourth wall was not confined to provide a benchmark for comparison. The dimensions, the horizontal reinforcement ratio, the vertical reinforcement ratio, and the applied axial load of all four masonry walls were identical. The confined reinforced walls were found to have enhanced the maximum loads by 6% to 14% compared to the unconfined wall. The results indicate that when the maximum load is applied, the drift increases by 58% to 64% when compared to the unreinforced wall. Finally, when confinement was added to the wall, the maximum drift increased by up to 123% when compared to the unreinforced wall.

Later in 1999, Ibrahim and Suter tested five reinforced masonry walls [47]. The parameters tested were the level of axial vertical stress, the amount of vertical reinforcement, and the wall aspect ratio. The results revealed that the shear behaviour depends on the compressive strut mechanism, the amount of horizontal reinforcement and the aggregate interlock. It was observed that all walls experienced the first major diagonal crack at almost the same displacement, even with changing the axial stress and wall length. The lateral capacity of the walls was not affected much by increasing the vertical reinforcement ratio. However, the lateral capacity increased considerably by increasing the axial load. On the other hand, it was shown that walls with a lower aspect ratio have more ductility and energy dissipation capabilities. Figure 2.10 shows the different crack patterns for the tested walls.

23
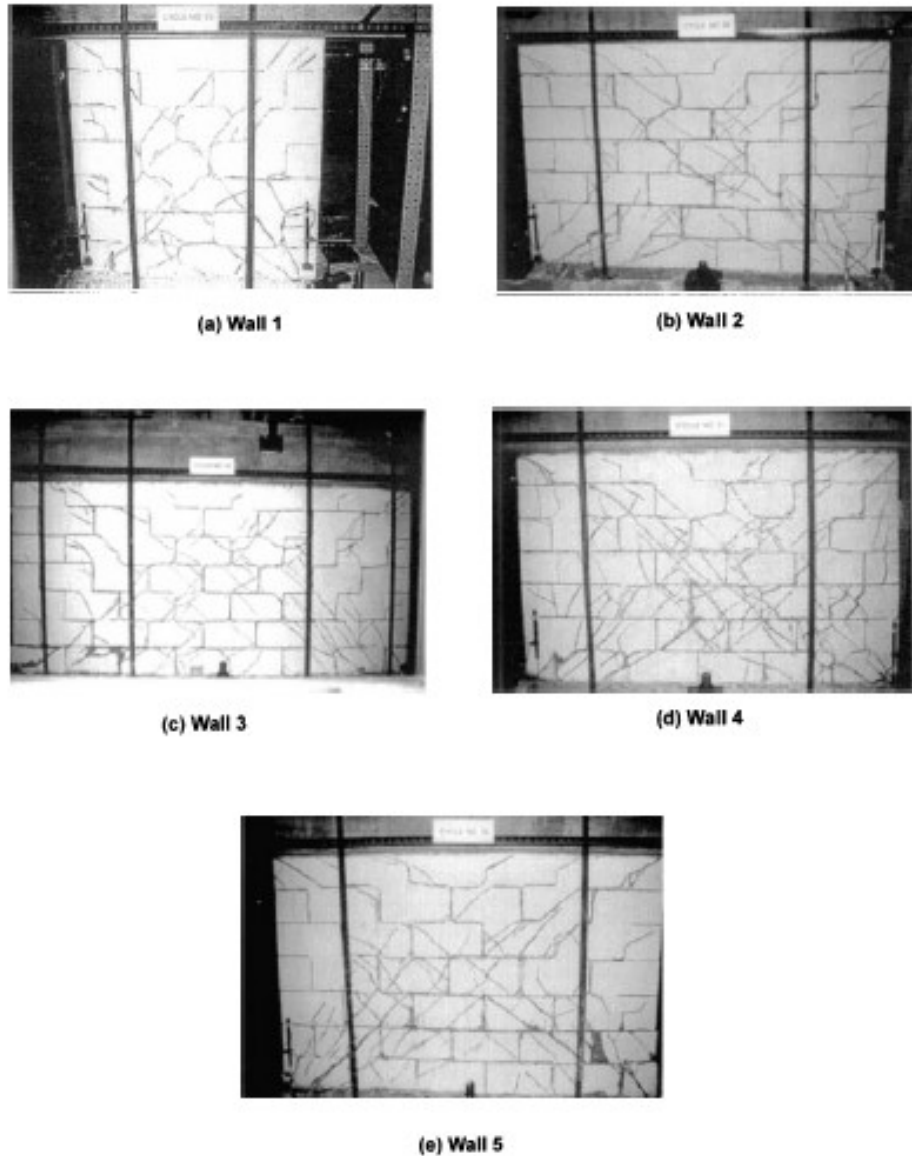
Figure 2.10: Cracks in walls tested by Ibrahim and Suter [47]

Snook et al. [48] investigated the influence of several forms of confinement reinforcement on RMSW's ductility and energy dissipation capability. Nine RMSW were subjected to reversed cyclic loading and constant axial stress. Three confinement methods were used to reinforce the walls: steel confinement plates, seismic reinforcement combs, and polymer fibres incorporated into the grout. The results of the tests suggested that employing these confinement techniques increased the displacement and energy dissipation capacities of the walls very slightly. In comparison to the use of confinement plates or seismic reinforcing combs in mortar joints, the

24

inclusion of polymer fibres in the grout mix increased energy dissipation and drift capacities the most. Additionally, by including the fibres into the grout, the shear resistance was enhanced, resulting in a reduction in the observed shear damage, i.e., diagonal cracks and shear deformations, in the tested walls.

Voon and Ingham [49] tested ten fully grouted and eight partially grouted RMSW. The aim of this study was to investigate the effects of axial stress, aspect ratio, grouting, and shear reinforcement on the response of RMSW. It is worth noting that while walls 2 and 4 to 10 were dominated by shear failure, wall 1 failed by flexural/shear, and wall 3 failed by flexural/sliding. Figure 2.11 shows the crack pattern and failure mode of the tested walls. These tests showed that increasing the axial load leads to increasing the shear capacity of the walls and decreasing the post-cracking deformation capacity. Uniformly distributed shear reinforcement helped to increase the shear capacity of the wall and improve the wall's post-cracking performance, which led to more ductile behaviour and higher energy dissipation. The fully grouted wall showed higher shear capacity. However, the influence of grout becomes less effective when the shear stress was calculated based on the net areas. Finally, it was demonstrated that the shear strength decreased with increasing the aspect ratio.

In 2010, Shedid et al. tested seven RMSWs with three different end configurations (rectangular, flanged, and end-confined [50]. The results showed that using flanged and confined boundary elements increased the wall's ductility by 39% and 106%, respectively. In addition, the measured drift at 20% drop from peak load was 1.0%, 1.5% and 2.0% for rectangular, flanged, and confined boundary elements walls, respectively. A 40% reduction in the required vertical reinforcement in flanged and end-confined walls, compared to rectangular walls, was achieved.

Kapoi, later in 2012, tested eight full-scale unconfined RMSWs and studied the effect of concentrated reinforcement at the end zones of the masonry walls on the response of RMSW [51]. It was concluded that the performance of evenly distributed reinforcement walls was very similar to walls with concentrated reinforcement, in terms of displacement ductility. However, walls with concentrated reinforcement were found to dissipate 50% more energy
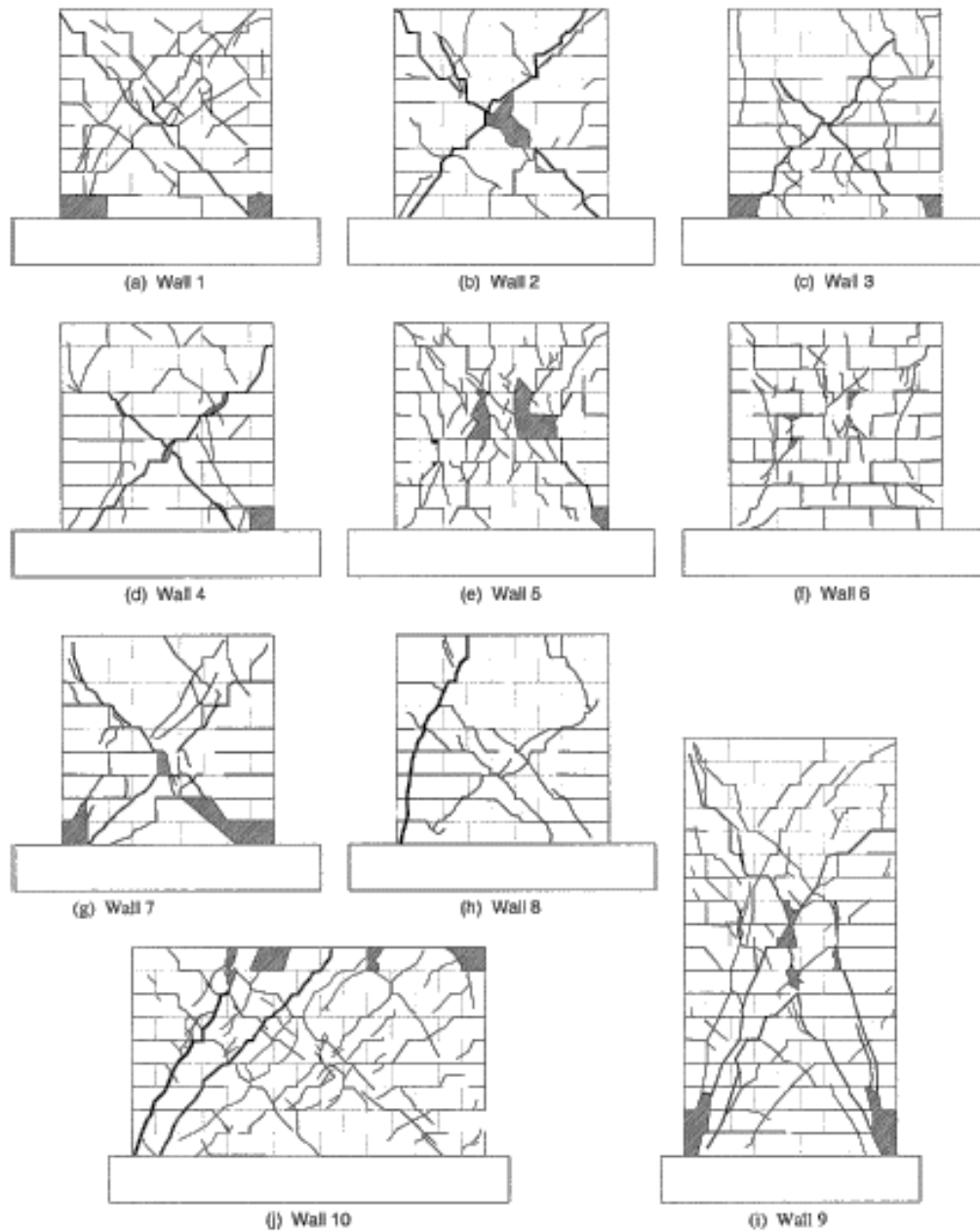
Figure 2.11: Cracks Pattern in walls tested by Voon and Ingham [49]

Banting [14] tested fully grouted half scale RMSW+BE to investigate the effect of confinement on wall drift and delaying vertical reinforcement buckling. The results showed that confining delayed the buckling of the vertical reinforcement and delayed the crushing of the grout core. The face shell spalling in the compression toes did not cause an abrupt drop in resistance. Figure 2.12 shows the details of the boundary element.
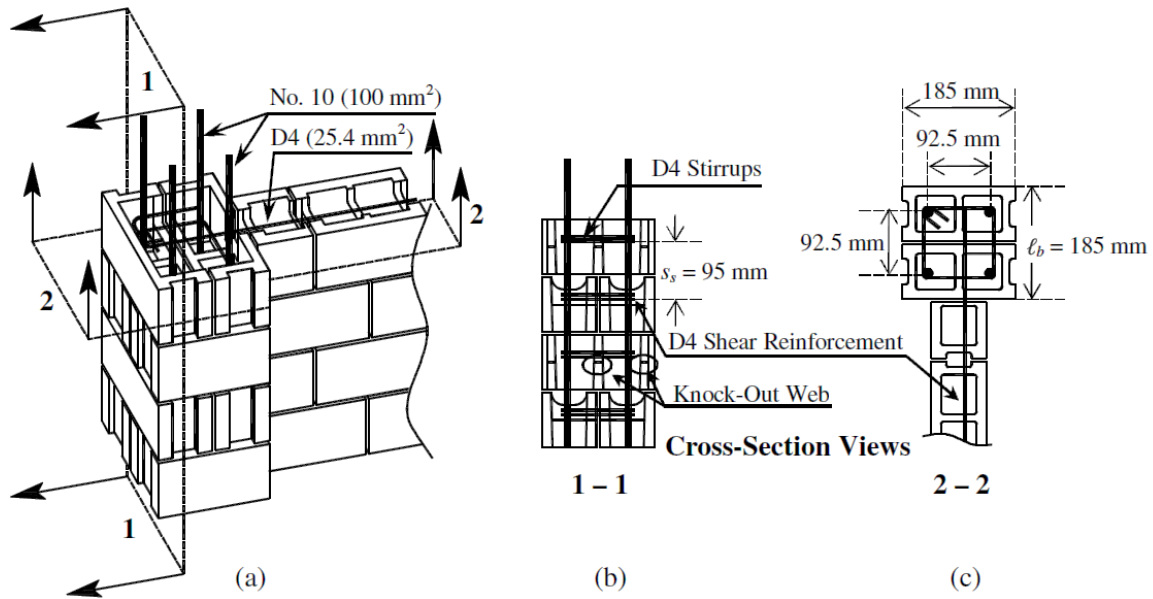
Figure 2.12: Boundary Element Detailing: a) Boundary Element Tied into Web of a RM Wall, b) Elevation View (Section1-1), and c) Plan View (Section 2-2) [14]

Thus, from these research efforts, results showed that adding confined boundary elements at the ends of the RMSW promotes the ductility of these walls and limits the damage to the wall's ends at the toe zone. Moreover, introducing a boundary element at the wall ends provides out-of-plane stability, decreases the required length of the compression zone, and increases the curvature capacity at maximum load. All these advantages can be achieved with even less vertical reinforcement ratio, compared to RM rectangular walls [15].

Ahmadi et al. [52] discussed the experimental results of 30 full-scale fully grouted RM shear walls tested under reversed quasi-static cyclic loading. The relationship between the nonlinear hysteretic response and key design parameters (aspect ratio, axial load, arrangement and amount of vertical reinforcement, and lap splices) was investigated. It was observed that the displacement corresponding to the peak strength decreases with the increase in the vertical reinforcement ratio. Lap splices in the vertical reinforcement caused a reduction in wall performance. Test results showed that specimens tested with low vertical reinforcement ratios developed higher displacement ductility.

Zhao and Wang [53] tested ten RMSW under reversed cyclic lateral load to investigate the influence of different reinforcements and applied axial stress values on their seismic behaviour. Larger values of normal stresses relate to larger values of lateral strength. The amount of

27

horizontal reinforcement improves the lateral strength due to smeared cracks, which are more evenly distributed by the presence of horizontal reinforcements. It also significantly improves the ductility due to the crushing toe failure of the walls. The stiffness for walls in the flexure mode decreases rapidly to 17%–19% and 48%–57% of the initial stiffness for walls in the shear mode and flexural mode, respectively at a displacement equal to half of the displacement corresponding to the peak load. The displacement ductility is strongly dependent on the amount of horizontal reinforcement.

As a part of a research program supported by NSERC CRD (Collaborative Research and Development) with the masonry industry (CCMPA, AEMQ, and CMDC) and led by Professor Khaled Galal, Albutainy et al., 2017 published the first conference paper outcome of this research program [19]. The existing experimental setup in the Structures Lab at Concordia was not suitable for testing RMSW+BE with high aspect ratio. This MTS-based setup was redesigned/modified by the author to a new configuration (shown in figure 3.7 in chapter 3). To allow the synchronization among the three actuators the MTS MPT files of control system were developed by Patrice Bélanger and Martin Leclerc of Polytechnique Montreal and commissioned by the author. Using this modified system, Aly and Galal further investigated the effect of increasing the axial load, wall aspect ratio and lab splice on the performance of RMSW+BE [54].

2.6   Previous experimental work on masonry prisms

Drysdale and Hamid [34] described the failure of unreinforced and unconfined masonry prisms as a brittle compression-tension failure. Based on that, there was a need to provide confinement to the masonry prisms to avoid the undesired brittle failure.

Priestley and Elder, 1983, tested twenty-one masonry prisms reinforced with steel plates in the bed joint (Priestley plates) [55]. The reinforcement plate eliminated the compression-tension failure and changed it to crushing failure, provided softer behaviour in the descending part of the stress-strain curve.

Hart et al., 1988, tested seventy-one prisms with different types of confinement [13]. The confinement techniques are Priestley plates, square ties, cages with hoops, spiral reinforcement, spiral reinforcement, and cages with spiral reinforcement. The confinement caused a ductile failure to the prisms and enhanced the post-peak part of the compression stress-strain curve.

Shedid et al., 2010, five groups of prisms, shown in Figure 2.13, to investigate the compression stress-strain relationship and the effect of vertical and confinement reinforcement [35]. G1 prisms were unreinforced and constructed using stretcher units. G2 prisms had vertical reinforcements and no confinement reinforcement and were constructed using stretcher units. G3 are reinforced prisms with confinement reinforcement and constructed using stretcher units. G4 prisms were unreinforced and constructed using pilaster units. Finally, G5 prisms were reinforced vertically and had confinement reinforcement and were constructed using pilaster units. The failure mode for the unreinforced masonry prisms, G1 and G4, was characterized by vertical cracks after face shell spalling. Prisms with vertical reinforcement, G2, had less damage than the unreinforced prisms and had more strength due to the existence of vertical reinforcement. Confined prisms, G3 and G5, provided more strength, compared with the unconfined ones, and no buckling in the vertical reinforcement was observed. In addition, confined prisms provided more gradual post-peak stress-strain relationship. For prisms made from pilaster units, the confined prisms showed an increase in the peak strength and its corresponding strain, as shown in Figure 2.14. Comparing G1, and G4 prisms, G4 had higher axial stress due to the confinement provided by the pilaster units. Comparing G3 and G4 prisms, both groups had almost the same axial stress; however, G4 prisms showed more ductile behaviour due to splitting and cracks in G1 prisms' mortar joints.
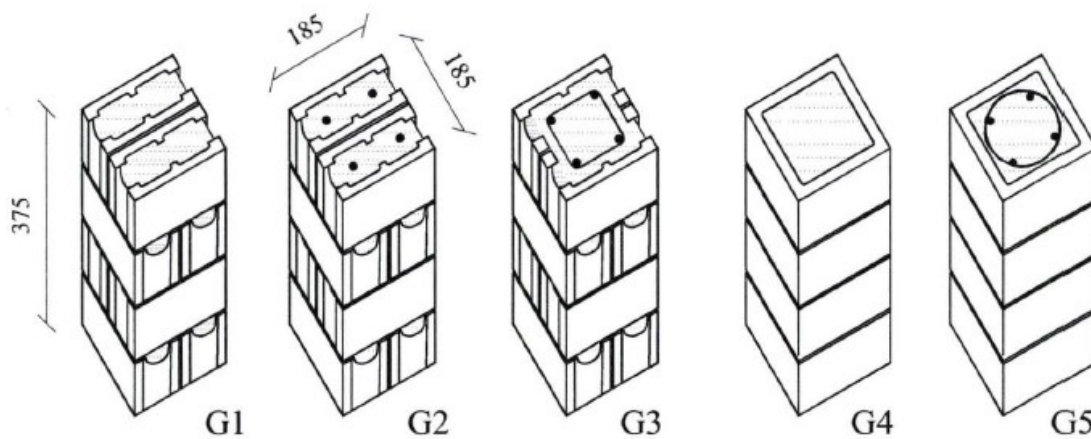
Figure 2.13: Boundary element prisms [35]
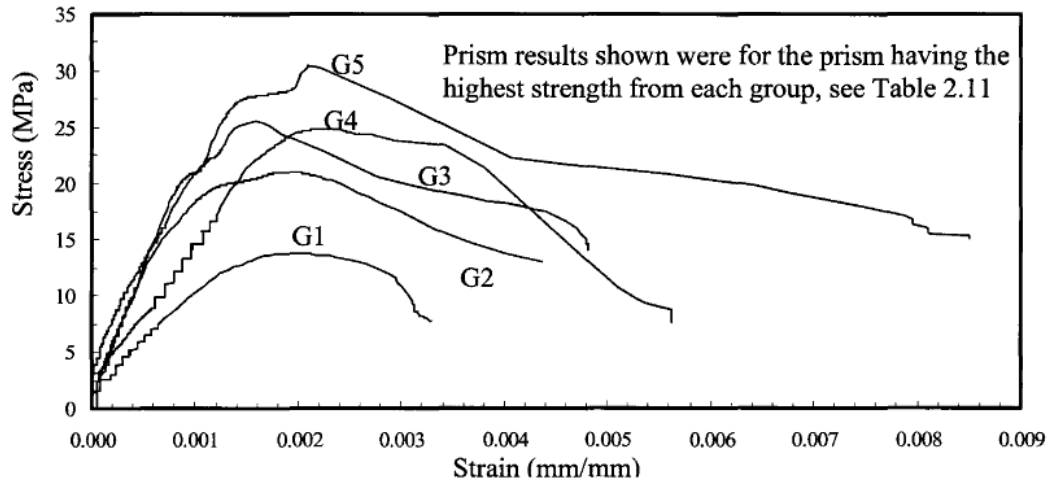
Figure 2.14: Stress-strain relationships for boundary element prisms [35]

Abo El Ezz et al. [56] studied the compressive stress-strain behaviour of unconfined and confined concrete block masonry boundary element columns. Under concentric axial compression, full-scale boundary elements were built and tested. No abrupt decline in strength was detected, and instead, a declining branch was recorded with a modest slope until reaching a 50% reduction in strength with an average strain of 0.005. The suggested model can be used to calculate strain ductility and curvature ductility of reinforced masonry walls with boundary features, resulting in a more cost-effective design in seismic areas. The effects of the confinement ratio on the compression stress-strain behaviour of RM boundary elements at the extremities of RM shear walls were investigated experimentally and numerically by Obaidat et al. [57]. Full-scale test units were built and tested until they failed under axial compression loading. Increasing the confinement reinforcement ratio had a considerable impact on post-peak behaviour, according to the findings. The descending branch of the stress-strain curves softened, resulting in an increase in the post-peak strain at 75% and 50 % of compressive strength of 1.25–1.87 times and 1.42–3.55 times that of the unreinforced units, respectively.

Abdelrahman and Galal [58] investigated the effect of vertical reinforcement ratio, the volumetric ratio of confinement reinforcement, the cross-section configuration, the bonding pattern, and pre-wetting of dry masonry shell before grouting on the axial compressive behaviour of unreinforced and reinforced masonry boundary elements. The results showed that increasing the volumetric ratio of the confinement reinforcement increased the strain ductility and the measured axial crushing strain. It is also reported that the rectangular reinforced BEs has

improved performance than their square counterpart, especially minimizing the stress drop following the face shell spalling.

2.7   Scale-Model Testing

In the area of scale model testing, many research efforts were directed toward investigating the reliability of the results obtained from reduced-scale test models. For concrete elements in general and masonry elements in particular, the most studied parameters were the strain rate, size effect, crack simulation, and testing methods on the uniaxial stress-strain relationship. The advantage of small-scale modelling is permitting the testing of the failure of complex structural configurations in a controlled laboratory environment and at an affordable cost [59].

Simulated testing of the seismic behaviour of a masonry building and its failure mechanisms requires satisfying some similarity laws that ensure duplicating the physical phenomena observed in the prototype structure [60]. The theory of models provides the framework for establishing the relationships between the physical quantities of the prototype and the model structures, e.g., the geometry, material properties, initial conditions, boundary conditions and environmental effects [61]. The scale factors for various physical quantities are determined through dimensionless analysis based on a 'force-length-time-temperature' system. The requirements of the similarity between the prototype and the model can generally be classified as: (a) similarity in the dynamic behaviour, which requires similar distribution of masses and stiffnesses along the height, and (b) similarity in the failure mechanism, which requires the similarity of the working stress level. The selection of the geometric scale factor is governed by practical limitations related to the capacity of the actuators (maximum driven mass), resonant frequency of the testing facility, and the effect of model-actuator interaction on controlling the simulated ground motion.

Generally, there are two types of similarity models that can be carried out for scale simulated testing: the complete and the simple models. In the complete similarity model, special materials are to be designed and produced to have their stress-strain curve scaled with the geometric scale while keeping their specific weight, Poisson's ratio, and damping the same as those of the prototype [60]. Although the two similarity requirements stated above are fully fulfilled in the complete similarity model, such special materials cannot be practically found [59]. This drawback limits the application of the laws of the complete model similarity in practical cases. In

the simple similarity model, however, the prototype materials are used to construct the models. This may explain why this model is commonly used for its simplicity and low cost, despite the need to add masses to compensate for not satisfying the requirement of mass distribution. It is worth noting that the disregard of some similarity requirements in the reduced-scale testing is often acceptable when their results are generated for developing or verifying analytical or numerical models [61].

In general, there are three test methods to investigate the seismic response of structural elements, namely, quasi-static, pseudo-dynamic and dynamic loading. The quasi-static test method is common for developing design and detailing procedures for structural elements and subassemblies. A predefined displacement history is often applied to the test specimen slowly, with frequent extended pauses to assess the specimen for damage visualization. Krawinkler [59] showed that slow testing resulted in a decrease in the strength and, consequently demonstrable rise in the deterioration of reinforced concrete (RC) and masonry structures. It was also pointed out that to establish design recommendations, the quasi-static loading method provides conservative results provided that the applied displacement history covers the expected range of deformation produced in severe earthquake events. A similar conclusion was drawn by Abrams [62]. Recently, the quasi-static test method was successfully applied to simulate the seismic action on brickwork specimens to investigate the effectiveness of a novel retrofitting approach for historical masonry buildings [63].

Abboud et al. [64] investigated the capability of forecasting the reaction of concrete block masonry using a one-quarter size model masonry unit. The standard six and eight inches prototype is duplicated in three different variants. Model slender wall panels were tested with and without axial loading under monotonic and cyclic out-of-plane loading. It was shown that direct modelling of masonry is a practical and cost-effective way to better understand complicated masonry systems. The model units were shown to respond similarly to the prototype at the material and assembly levels. Despite minor differences, the model and prototype were found to have good-to-excellent correlations.

The behaviour of half-scale and full-scale masonry elements under axial compression and diagonal tension have been investigated by Long et al. [65]. It was found that the stress-strain behaviour of both half-scale and full-scale masonry are comparable, especially for the grouted

masonry. Also, the half-size masonry exhibited similar strength and failure modes as the full-size prototype. Therefore, it was concluded that the half-size masonry could be used as a suitable model in the behaviour of full-sized grouted masonry shear walls. Mohammed et al. [66] looked at the scaling effect on the structural behaviour of clay bricks under compression. They considered four scales, namely prototype, half, fourth, and sixth scale. The results revealed that the strength of the masonry triplet in compression was greater than the prototype in the fourth and sixth model scales but similar to the prototype in the half scale.

2.8   Numerical modelling of fully grouted RMSW

Predicting the behaviour of RM walls under lateral loads requires enhanced numerical tools that are calibrated using controlled experimental tests. This section presents an overview of the different modelling techniques that have been used by researchers in the modelling of RM shear walls.

Since masonry is a composite material with anisotropic behaviour and is subjected to a bi-axial stress condition, masonry shear walls exhibit complex structural behaviour. There have been several numerical models carried out in an attempt to analyze and better understand their behaviour under seismic loads. Simulating the nonlinear behaviour of RMSW can be done in two ways. The discretization of a structure into a finite number of small elements is the basis of micro-modelling. Macro-modeling, on the other hand, is based on expressing the overall structure with larger elements, each with properties equal to the total of its components [67]. Although Macro-modeling is the ideal method for studying features such as strength capacity, energy dissipation, and structure deformation since it requires less processing time, it cannot capture a structural member's local response. The drawback of Micro-modeling is it requires a high level of meshing and detailing and is a complex approach that necessitates an extensive computational effort.

Haach et al. [67] conducted a numerical analysis to determine the behaviour of masonry walls subjected to lateral loading. Additionally, the influence of various parameters on the lateral behaviour of brick walls was evaluated. The numerical simulation was conducted using a micro-modelling approach to investigate the resisting mechanisms of brick walls. A comprehensive parametric analysis was conducted with the objective of determining the effect of the aspect ratio, vertical pre-compression, horizontal and vertical reinforcement ratios on the in-plane

33

behaviour of brick walls. Shear failure is more likely to occur on walls with a low aspect ratio and a moderate pre-compression level, whereas flexure failure is more likely on walls with a high aspect ratio and a low pre-compression level. However, it was observed that flexure dominates the in-plane reaction of cantilever walls, whereas shear failure dominates the in-plane response of fixed end walls. Vertical reinforcement has a varying effect depending on the main resisting mechanism. It has a negligible effect on the lateral resistance of walls when shear is the dominant effect, but enhanced the lateral strength when flexure is the dominant effect, since reinforcement resists tensile stresses caused by the wall's elevation. When horizontal reinforcement is used, its effect on the behaviour of shear walls is similarly dependent on the predominance of resistant shear processes. Horizontal reinforcement, as seen in experiments, acts only after diagonal breaking. Additionally, horizontal reinforcement improved stress distribution inside the walls, resulting in more evenly distributed diagonal cracking. It was discovered that horizontal reinforcement had a negligible effect on the lateral resistance of cantilever walls due to the predominance of the flexure mechanism.

Minaie et al. [68] developed an effective nonlinear 3D finite element modelling approach that was correlated with experimental results and demonstrated the model's ability to accurately simulate the capacity (within 10%), failure mechanisms, and hysteretic response of partially-grouted (PG) brick shear walls. The effect of bi-directional loading was then investigated using this model in a series of parametric simulations with out-of-plane drift, wall aspect ratio, and vertical stress as variables. The study showed that The Concrete Damage Plasticity (CDP) model is a powerful tool for modelling the nonlinear cyclic response of masonry. The findings of the parametric analysis indicated that when out-of-plane drift is applied at the top of the walls, the in-plane capacity of masonry shear walls with cantilever boundaries can be reduced by up to 20%. When the level of axial tension is reduced and the effective aspect ratio is increased, this effect becomes stronger. In addition, the bidirectional input received by masonry shear walls during earthquakes influences the in-plane capacity of the walls. The susceptibility of masonry shear walls to out-of-plane drift is much more abruptly up to the point where such drift results in the cracking of the PG masonry walls. Although out-of-plane drift causes early cracking in PG masonry shear walls, which reduces peak capacity, it has no noticeable influence on the response of PG masonry shear walls, and consequently most likely has no discernible effect on their overall seismic performance.

Seif Eldin et al. [69] simulated the nonlinear behaviour of masonry walls, using numerical models based on the finite element method FEM that has been created utilizing VecTor2 software. To simulate the behaviour of the RM shear walls, a nonlinear finite element (FE) model was created. The model was validated using the test results of two single-storey fully grouted RM shear walls, which demonstrated that the FEM was within an acceptable degree of accuracy, in comparison to the experimental data. A parametric study was undertaken to determine the effect of shear reinforcement distribution, axial compression stress level, and wall aspect ratio on the in-plane shear behaviour of RM shear walls. The results of this numerical investigation indicated that the distribution of shear reinforcement has no discernible effect on the shear strength. On the other hand, it increases displacement ductility when axial compression stress is applied at a low level.

2.9 Summary and remarks

Intensive research efforts were conducted to better understand and enhance the performance of reinforced masonry shear walls (RMSW). The review of the literature revealed that RMSW is capable of performing as an effective seismic force resisting system (SFRS) for mid-rise buildings in moderate seismic zones. Many confinement techniques were suggested to enhance the RMSW ductility and its energy dissipation capabilities by increasing the measured compressive strain. Adding boundary elements, as an end confinement method, has the advantage over the other proposed confinement methods. Boundary elements have the advantages of providing space for two layers of vertical reinforcement with confinement hoops, providing out-of-plane stability, decreasing the compression zone, and reducing the required vertical reinforcement up to 40%. In addition, boundary elements are currently formed from stretcher units, so no special material or reinforcement are required. However, using stretchers to form the boundary element limits the vertical and confinement reinforcement and the size of the boundary element. Moreover, using stretcher units have some constructability issues. In summary, the current practice of constructing the RMSW+BE can provide strength, stiffness, and ductility to perform as SFRS. However, there is still a need to have RMSW system with better confinement, more vertical reinforcement in the boundary elements, flexibility to change the boundary element length and better constructability. On another aspect, the equations provided in the literature to predict the plastic hinge height for RMSW has large variability

depending on the parameters considered in the equation. The current equations still miss considering the level of confinement in the boundary elements and the dimension of the boundary element.

In this research, the proposed RMSW was developed in collaboration with industry partners to make sure of its practicality. Then a well-designed testing program is conducted to investigate the performance of the proposed system under seismic excitation. To overcome the high cost and time typically associated with experimental work, numerical models capable of capturing the local response of the RMSW will be developed.

This critical review of the state-of-the-art in this area of research on the seismic performance of ductile reinforced concrete masonry shear walls allowed us to identify some gaps that need to be addressed within the scope of this research program. These gaps are implicitly translated into the Hypotheses statement (section 1.4) and the Specific objectives and scope of work (section 1.5).

Chapter 3
Experimental setup and testing program

3.1   Introduction

In order to test the research hypotheses and achieve its objectives that were identified in Chapter 1, sections 1.4 and 1.5, respectively, a new configuration for RMSW with C-shaped masonry units has been proposed. A specially designed experimental test setup was used to allow investigation of the response behaviour of the lower panel of RMSW+BE in a 12-storey building subjected to quasi-static loading protocol. This research aims to quantify the effect of influential parameters on the seismic performance of Reinforced Masonry Shear Walls with masonry boundary elements (RMSW+BE).

In this chapter, the research program is defined. A new configuration for RMSW with C-shaped masonry units is developed, and the design and control of the test setup are developed and described. This study is part of an extensive research program conducted at Concordia University. This research project involves the testing of twelve wall specimens to investigate the effect of the following variables on the seismic response of RMSW with C-shaped boundary elements: the boundary element vertical reinforcement ratio, the boundary element confinement ratio, the size of the boundary element, the axial load ratio, the vertical reinforcement lap splice, the type of blocks used to form the boundary elements, and the wall aspect ratio. In the first phase of this project, six walls were tested in two stages. Stage one studied three walls to verify the performance of the testing setup and to evaluate the effects of the boundary element's confinement ratio [70]. These tests were the pilot tests for the entire program. In the second stage, three walls were tested to investigate the effect of the boundary element configuration, specifically, the vertical reinforcement ratio and the size of the boundary element.

3.1.1   Proposed boundary element masonry units

Given the size limitations of the existing testing machines and the limited laboratory space, it was decided to use half scale units to construct the walls. The design of the experimental setup is based on a simple similarity model in consideration of technological and economic factors discussed in the introduction section. Figure 3.1 shows the shape and dimensions of the masonry units used in the construction of the walls. The four masonry units were manufactured at CMDC

and shipped to Concordia University's Structures Laboratory. The masonry units to form the boundary elements were the uncut rectangular blocks shown in Figure 3.1(a). The units shown in Figure 3.1(b, c, and d) are the stretcher, the depressed web stretcher, and the half-block unit, respectively. The rectangular boundary element units were cut, using a concrete saw, into two C-shaped blocks facing each other to form the masonry boundary elements shown in Figure 3.2. A small notch was made in the boundary element masonry block to allow passing of the horizontal reinforcement.
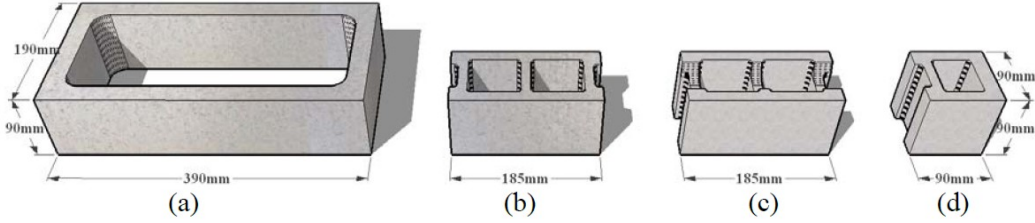
Figure 3.1 Half scale unit types and dimensions [71]

Figure 3.3 shows the wall components [19], where D8 (diameter = 8.11 mm) horizontal reinforcement deformed wires were spaced at 285 mm along with the wall height and were placed alternatively [72]. These shear reinforcement wires had hooks at 90° from one end and 180° from the other end. In addition, the D8 horizontal reinforcement with 180° hooks was embedded in the boundary element and extended inside the web with sufficient development length to develop the yield strength on both sides along the interface between the boundary element and the web to resist the shear flow.
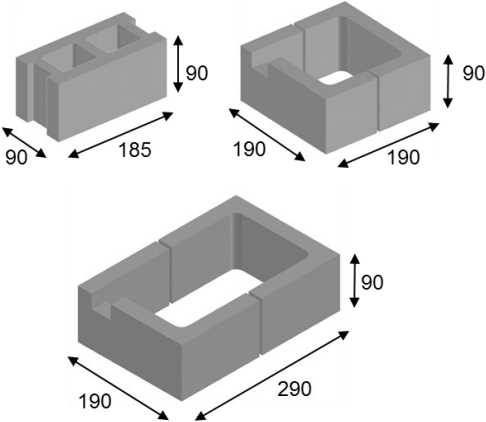
Figure 3.2 Masonry boundary elements after being cut (all dimensions are in millimeter)

38
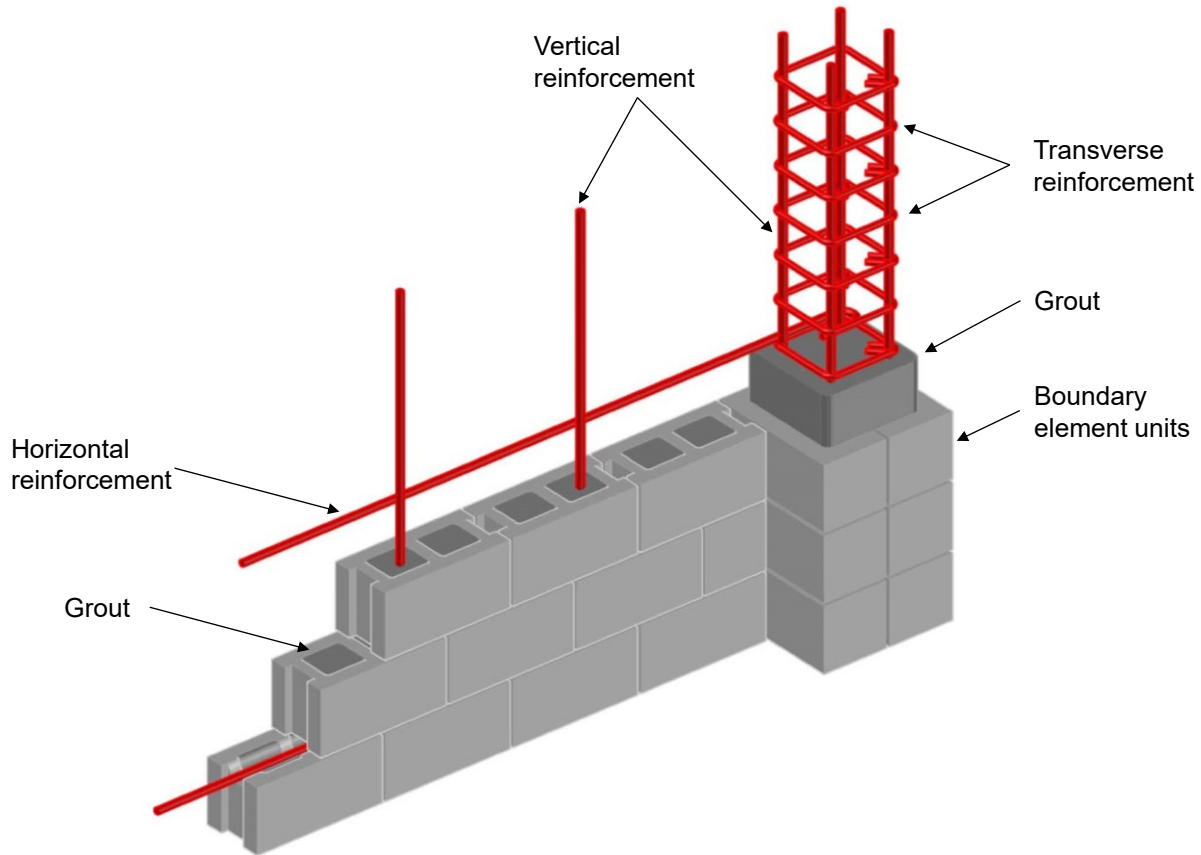
Figure 3.3 Wall Components

3.1.2 Selection of the shear walls

A twelve-storey residential building with an overall wall height of 36.50 m was designed to be constructed in Montreal, Quebec, Canada. According to the plan shown in Figure 3.4, the slabs were designed to be 180 mm thick flat plates. The exterior and interior columns were designed to be reinforced concrete columns with the dimensions of 380 x 380 mm and 570 x 570 mm, respectively. The shear walls were reinforced concrete masonry walls with boundary elements. The web thickness of the shear wall was 190 mm, while the boundary element dimensions were 390 x 390 mm. The building's interior and exterior spans were 6.00 m and 5.50 m, respectively. The ground floor height was 3.20 m, and the typical floor height was 3.07 m. A normal density concrete with a specified compressive strength $f'_c = 30$ MPa was assumed for slabs and columns. The compressive strength of the reinforced masonry members f'_m for the boundary elements and the web of the shear wall were assumed to be 30 MPa and 17 MPa, respectively. The reinforcement yield strength was taken as 400 MPa. For typical floors, the dead

loads assigned to the building are the self-weight of the building and 1.50 kPa for partitions and mechanical services. It was also assumed that the live load is 1.90 kPa for residential occupancy and 2.48 kPa for the snow load on the roof [21]. The shear walls were further assumed to carry 100% of the applied lateral loads. The force modification factors used to calculate seismic forces R_d and R_o were 3.0 and 1.5, respectively, in the N-S and E-W directions according to NBCC 2015 [21] and CSA S304-14 [20]. For design, the soil was assumed to be class C. The wall on gridline (A) and between gridlines (1 and 2) shown in Figure 3.4 was selected as the base wall. The wall's total length was 3.43 m. The base wall was designed according to CSA S304-14 [73]. The reference wall's (W4-$C_{Lb,VRFT}^{190,8}$) reinforcement was detailed to satisfy CSA S304-14 [73] requirements for web and boundary elements zones. The maximum reinforcement ratio specified in CSA S304-14 [73], clause 10.15.2, is 2% of the wall's gross area. For the BEs within the plastic hinge zone, the minimum number of vertical reinforcement rebar is four and with a minimum reinforcement area equal to $0.00075b_w l_w$ (Clause 16.11.8), where b_w is the web thickness and l_w is the wall length. The transverse reinforcement hoops' spacing in the BEs were selected to satisfy the vertical reinforcement buckling prevention requirements in Clause 16.11.4. Boundary element maximum reinforcement ratio is not explicitly stated in CSA S304-14 [73]. Boundary element could be considered as a column with gradient strain distribution, thus the maximum reinforcement ratio in the BE was considered as 4% as recommended in CSA S304-14 [73] clause 10.15.4. The reinforcement details provided in the reference wall, and in turn the remaining of the tested walls, were in compliance with the above mentioned requirements.

The Canada Masonry Design Centre (CMDC) specified two construction requirements. First, the boundary elements should be aligned with the wall such that their major axes are along the same plane to avoid creating flanged walls. The second requirement was that the boundary element should have one edge in the same plan as the rest of the wall to avoid barbell-shaped wall cross-sections. Keeping the boundary element flush with one face of the wall aids the mason by providing a clear surface to maintain wall levelness and plumpness over its height. This orientation also minimizes the disruption of the boundary element to the architectural wall layout and space planning. Where possible, the recessed area and cavity of the boundary element walls located around the building peripherals should be used for insulation. Orientating the boundary element in-line with the wall also reduces the architectural impacts of the boundary element.
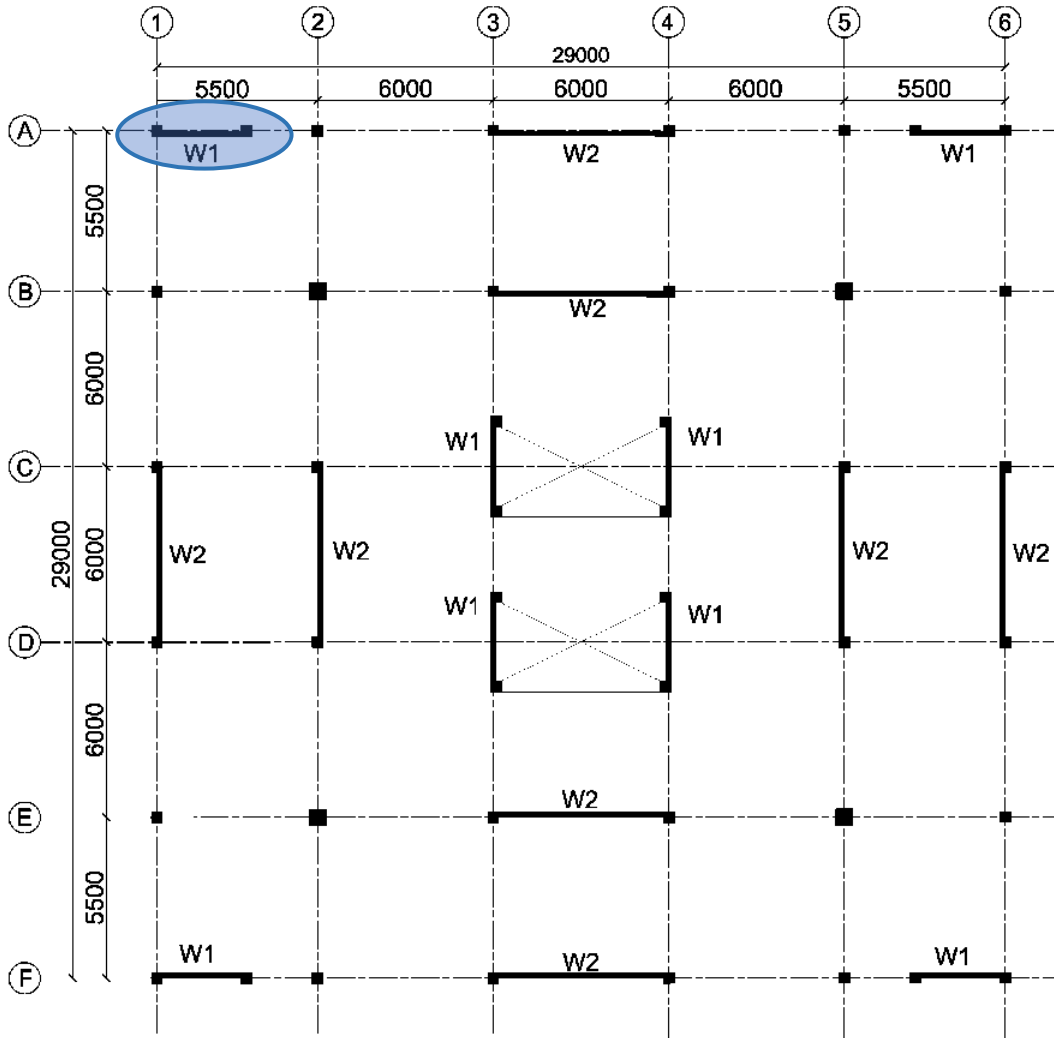
Figure 3.4 Building Plan

3.1.3 Design of experiments and test matrix

To evaluate the effect of the confinement ratio of the boundary element on the RMSW seismic response, the experimental setup was used to test six RMSW with C-shaped boundary elements to assess their seismic performance. The dimensions of the original building were divided by two to represent a half-scale specimen of the walls to be tested. Therefore, the length of the wall on gridline (A) between gridlines 1 and 2 (Figure 3.4) was selected to be 1,715 mm. In the test matrix shown in Figure 3.5

Six half-scaled RMSW+BE were tested under a reverse cyclic top moment and lateral loading in two testing phases. The walls were designed to fail in flexural mode. Following the CSA

41

S304-14 [1], the shear walls were designed to provide a safe margin for shear and sliding resistance to prevent undesirable shear failure. The height of the tested walls (h_{lab}) was 2.38 m, which represents the plastic hinge zone of a half-scale twelve-storey building with a total height (h_w) of 18.25 m. The plastic hinge zone length (L_p) was calculated based on Equation 3-1 recommended by CSA S304-14 Clause 16.10.3[20].

$$L_p = 0.5l_w + 0.1h_{eff} \qquad\qquad \text{Equation 3-1}$$

where l_w is the length of the wall and h_{eff} is the effective height of the wall, which was selected to be two-third of the total height of the wall. The boundary width (B_b) were selected to be 190 mm to represent a standard masonry concrete block. Boundary element length (L_b) is varying between two values, 190 mm, and 290 mm, to represent the length of one block and one and half block respectively.

The flexural capacity was calculated using the CSA S304-14 [20] procedure without taking into consideration the material reduction factors ϕ_m and ϕ_s. The shear walls were designed to provide shear and sliding resistance with a safe margin to avoid undesirable shear failure. Figure 3.5 shows the wall dimensions and reinforcement arrangement.

In the test matrix shown in Figure 3.5, W4-$C_{L_b,VRFT}^{190,8}$ is the base wall extracted from the design explained in section 3.1.2. The remaining walls in the test matrix configurations were selected to address the research objectives stated in section 1.5.

Table 3.1 and Table 3.2 provide a summary of the dimensions of the walls, the web, and the boundary elements, as well as the axial applied stress. Each wall is given an ID to identify the parameter under investigation. For instance, in phase one, the first wall is identified as W1-C_S^{60} to show that the boundary elements were made of C-shaped masonry units and the vertical spacing (S) of the hoops was 60 mm. For phase two, wall "W4" is referred to as W4-$C_{L_b,VRFT}^{190,8}$ to indicate that the boundary elements were made of C-shaped masonry units and that the length of the boundary element (L_b) is 190 mm, and the number of #3 bars (VRFT) in the BE is eight. The parameters ρ_v, ρ_x and ρ_y given in Tables 3.1 and 3.2 stand for the vertical reinforcement ratio in the boundary elements and the transverse reinforcement ratio perpendicular and parallel to the boundary element thickness, respectively. They were calculated using Equations 3-2 and 3-3:

$$\rho_x = \frac{A_s n_x}{d_c S} \qquad\qquad \text{Equation 3-2}$$

$$\rho_y = \frac{A_s n_y}{b_c S} \qquad\qquad \text{Equation 3-3}$$

where A_s is the hoop cross-sectional area, n_x and n_y are the number of hoop branches perpendicular and parallel to the boundary element thickness, respectively, d_c and b_c are the length of the confined core of the boundary elements perpendicular and parallel to the boundary element thickness, respectively, and s is the vertical spacing between hoops.

For all tested walls, the boundary elements have confinement hoops reinforcement of D4 wires (diameter = 5.6 mm) with 60 mm spacing. The web was reinforced vertically with four #3 rebars and horizontally with D8 wire (diameter = 8.11 mm) spaced vertically at 285 mm and 190 mm for phase one and phase two, respectively. The increase in the shear reinforcement in phase two walls was due to its higher flexural capacity. Each wall is given an ID to identify the parameter under investigation. For instance, in phase one, the first wall is identified as $W1\text{-}C_S^{60}$ to show that the boundary elements were made of C-shaped masonry units and the vertical spacing (S) of the hoops was 60 mm. The length of phase one walls was 1715 mm and they are similar in dimensions and reinforcement except for the spacing between the vertical hoops reinforcement in the boundary elements.

For phase two walls, the total length of $W4\text{-}C_{Lb,VRFT}^{190,8}$ is 1715 mm, and the size of the boundary elements is 190 x 190 mm. The boundary elements were reinforced using eight #3 vertical rebars. The total length of $W5\text{-}C_{Lb,VRFT}^{290,8}$ is 1725 mm and the size of the boundary elements is 190 x 290 mm. The boundary elements were also reinforced using eight #3 vertical rebars. The total length and the size of the boundary element of $W6\text{-}C_{Lb,VRFT}^{290,6}$ are identical to those of $W5\text{-}C_{Lb,VRFT}^{290,8}$. However, boundary elements were reinforced using six vertical #3 rebars. $W4\text{-}C_{Lb,VRFT}^{190,8}$ is considered the reference wall for this group of walls. Comparing $W4\text{-}C_{Lb,VRFT}^{190,8}$ and $W5\text{-}C_{Lb,VRFT}^{290,8}$ would determine the effect of changing the boundary element length on the wall's behaviour, while keeping the same amount of vertical reinforcement. Comparing $W5\text{-}C_{Lb,VRFT}^{290,8}$ and $W6\text{-}C_{Lb,VRFT}^{290,6}$ would reveal the effect of the boundary element vertical reinforcement ratio on the wall's response. All walls were subjected to axial compressive stress of 1.5 MPa.
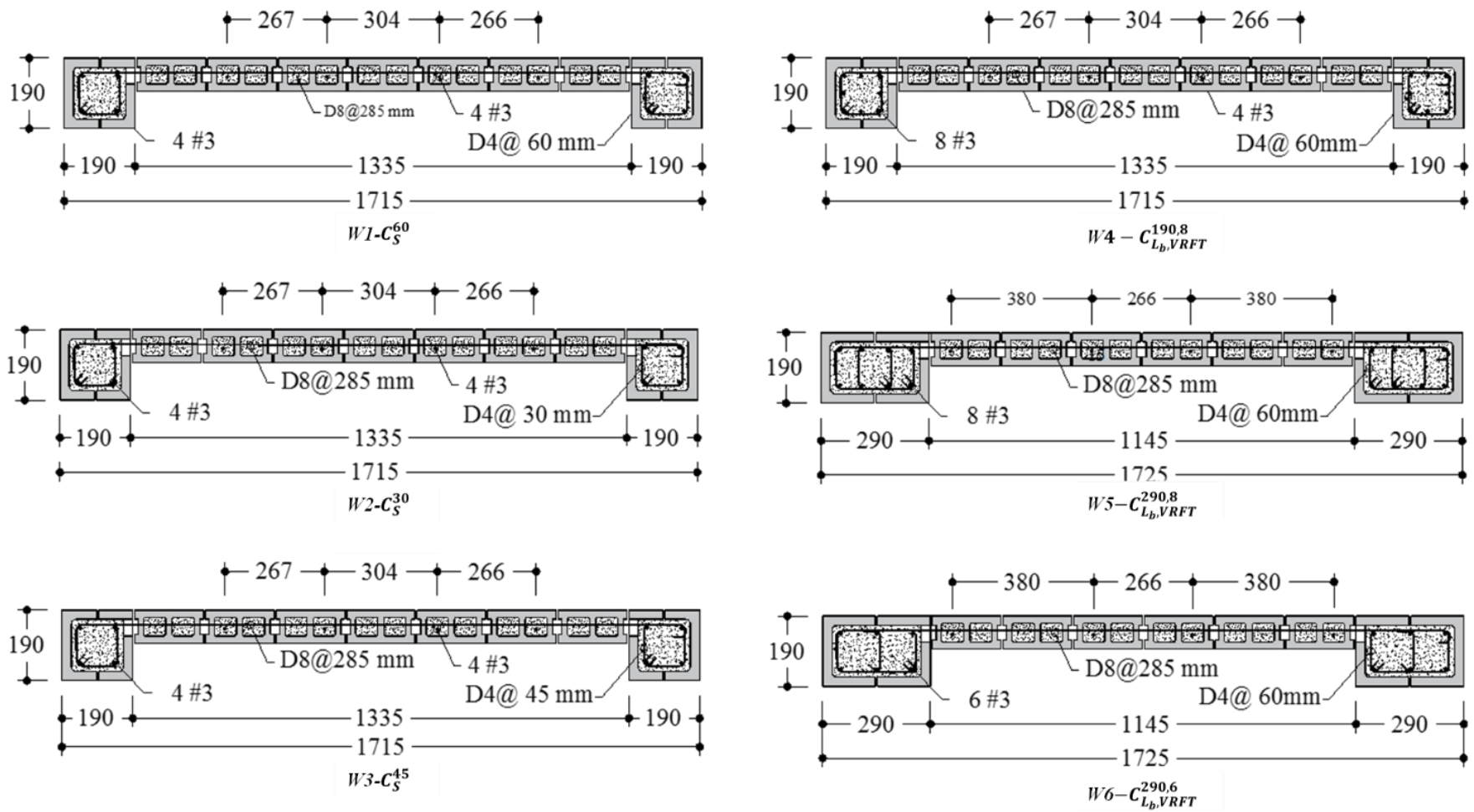
Figure 3.5 Dimensions and reinforcement arrangement of the tested walls (all dimensions are in millimeters)

Table 3.1: Text matrix for phase one

| | | | | | | Common Parameters | | | | | | | Studied Parameters | | |
| | | | | | | Web | | | Boundary Element | | | | | | |
Wall ID*	Wall Length (mm)	Wall total Height, h_w (m)	Lab wall Height, h_{lab} (m)	Aspect ratio**	Axial Stress (MPa)	Thickness (mm)	Vert. bars	Horizontal bars***	Length (mm)	Width (mm)	Vert. bars	ρ_v (%)	ρ_x (%)	ρ_y (%)	Hoops***
W1-C_S^{60}	1715	18.25	2.38	10.6	1.5	90	4#3	D8@285	190	190	4#3	0.79	0.74	0.74	D4@60
W2-C_S^{30}	1715	18.25	2.38	10.6	1.5	90	4#3	D8@285	190	190	4#3	0.79	1.49	1.49	D4@30
W3-C_S^{45}	1715	18.25	2.38	10.6	1.5	90	4#3	D8@285	190	190	4#3	0.79	0.99	0.99	D4@45

* Based on the parameters studied in this paper
** Calculated using wall height (h_w) = 18.25 m
*** Spacing in mm

Table 3.2: Text matrix for phase two

| | | | | | | Common Parameters | | | | | | | Studied Parameters | | |
| | | | | | | Web | | | Boundary Element | | | | | | |
Wall ID*	Wall Length (mm)	Wall total Height, h_w (m)	Lab wall Height, h_{lab} (m)	Aspect ratio**	Axial Stress (MPa)	Thickness (mm)	Vert. bars	Horiz. Bars***	Width (mm)	ρ_x (%)	ρ_y (%)	Hoops	ρ_v (%)	Vert. bars	Length (mm)
W4-$C_{L_b,VRFT}^{190,8}$	1715	18.25	2.38	10.6	1.5	90	4#3	D8@190	190	0.74	0.74	D4@60	1.57	8#3	190
W5-$C_{L_b,VRFT}^{290,8}$	1725	18.25	2.38	10.6	1.5	90	4#3	D8@190	190	0.74	0.78	D4@60	1.03	8#3	290
W6-$C_{L_b,VRFT}^{290,6}$	1725	18.25	2.38	10.6	1.5	90	4#3	D8@190	190	0.74	0.58	D4@60	0.77	6#3	290

* Based on the parameters studied in this paper
** Calculated using wall height (h_w) = 18.25 m
*** Spacing in mm

3.1.4 Wall construction

Skilled certified masons built the walls to ensure repeatability and minimize the uncertainty associated with the variability of the construction. The web was constructed using a running bond pattern, and the boundary elements were constructed using a stack pattern. The construction of the wall begins by casting the foundation with a complete length of vertical reinforcement. Then, the first course was laid for the full length of the wall, including the boundary elements of the C-shaped pilaster. At this point, the outer C-shaped pilasters were not laid out. As a result, this technique allows the mason to install the horizontal reinforcement from the wall side, position the reinforcement cage and perform the necessary inspection. The walls were constructed in three parts to represent the low-lift technique performed in practice. The actuator forces were eventually transferred to the wall via the reinforced concrete top-loading beam. Figure 3.6 shows the construction sequence of the walls.

(a)

(b)

(c)

(d)

(e)

(f)
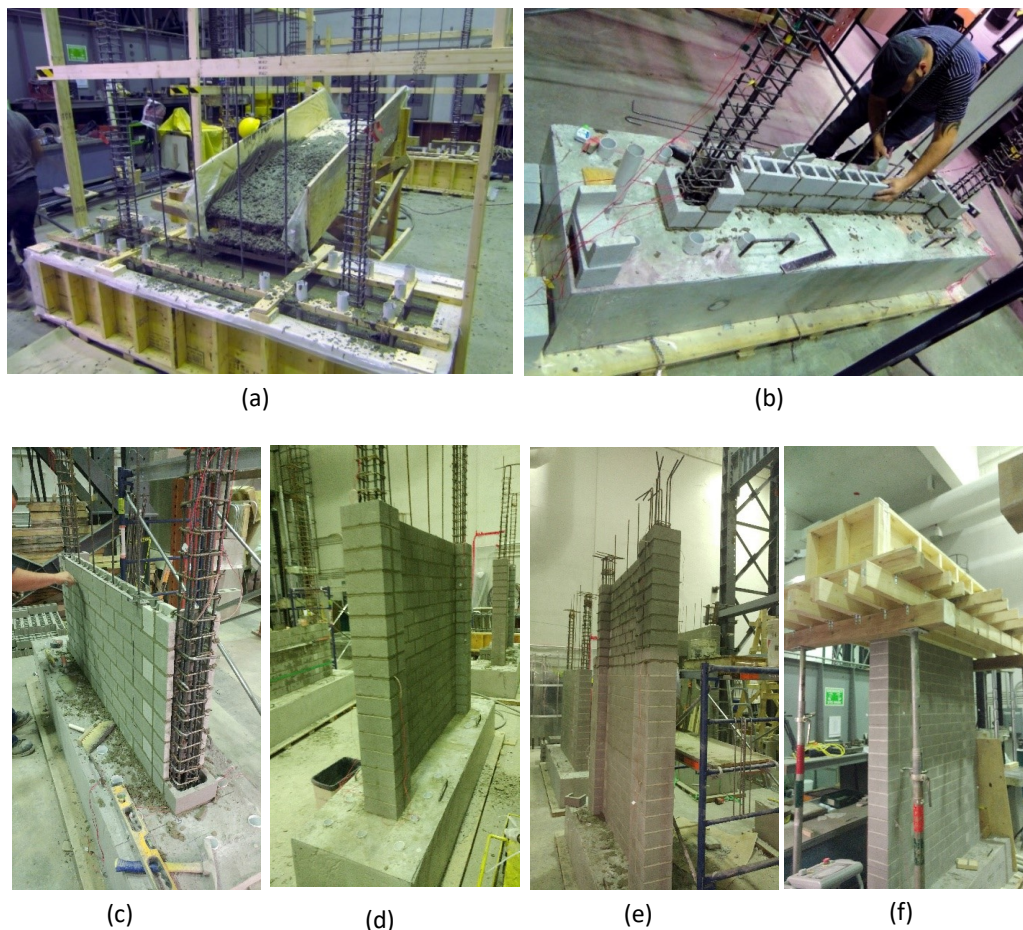
Figure 3.6: Construction sequence for the walls

3.2   Design of Experimental Setup and Control System

3.2.1   Test setup and Instrumentation

Tests were conducted using a specially designed test setup consisting of a steel frame equipped with three attached MTS actuators for load application. This test setup allows the application of lateral displacement increments in a quasi-static pattern to observe the full lateral behaviour of the tested wall. The reaction frame shown in Figure 3.7 was designed to support two vertical actuators and one horizontal actuator. The capacity of each of the three MTS digitally controlled actuators is 750 kN in compression and tension, with a maximum stroke of 400 mm. The test setup allows testing the shear wall's plastic hinge zone when subjected to a constant/variable axial load along with synchronized cyclic lateral displacement and cyclic top moment. The lateral displacement was applied by the horizontal actuator, while the vertical actuators applied the top moment. The laboratory's strong floor has twelve tie-down anchorages. A heavily reinforced concrete footing, or transfer footing, was constructed to tie the specimen's footing to the laboratory's strong floor via twelve 2" high-strength threaded rods. This arrangement prevented sliding and overturning of the wall under test. The wall footing is a 2,300 × 640 × 400 mm reinforced concrete footing. This foundation was secured to the base foundation by eighteen (out of available forty-four) 1" high tensile threaded rods as shown in Figure 3.8. Finally, a reinforced concrete top loading beam was used to transfer actuator forces to the wall. The details of the loading beam are shown in Figure 3.9.
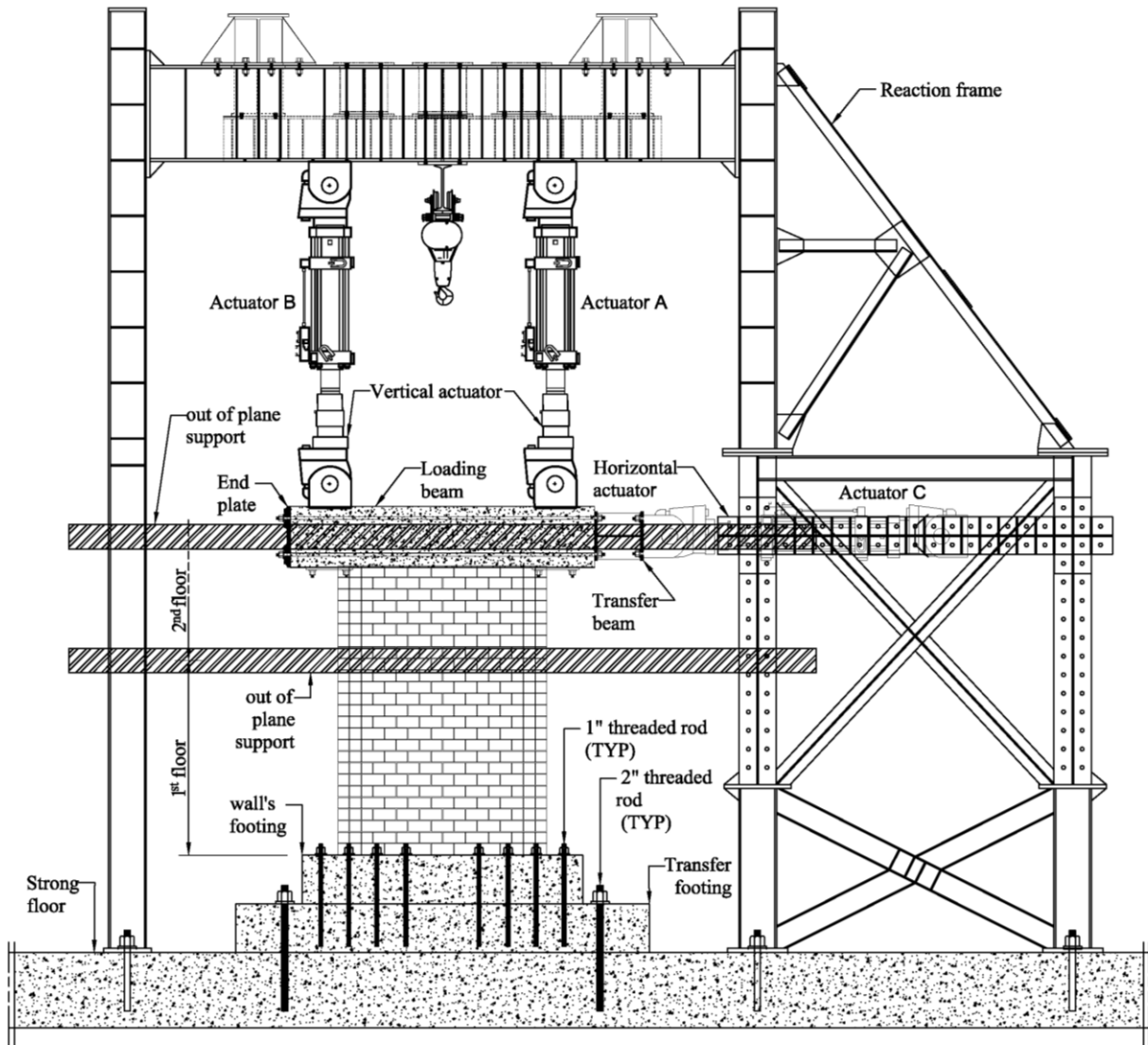
Figure 3.7: Test setup and reaction frame

Figure 3.8: Wall Foundation Layout

Figure 3.9: Loading beam details

The relative displacements between the wall and the top-loading beam and between the wall and the footing were monitored in two locations using linear potentiometers. This allowed capturing any sliding that may occur either at the top or at the bottom of the wall. The uplift of the wall's footing was also monitored using a string potentiometer to account for this effect on the lateral displacement, if any. The test measurements showed that no sliding nor uplift occurred. Figure 3.10 shows the instrumentation layout used in this investigation. Five string potentiometers (P1-P5) were attached to rigid support from one side, while the other side was

attached to the wall under test. Potentiometers P1 and P2 were used to track the wall's top displacement. The measured displacement values were used to draw the force-deformation relationship. Potentiometers P3 and P4 were used to measure the wall's lateral deformation at different heights, and they were spaced at approximately 1,100 mm. Potentiometer P5 was used to measure footing sliding, if any. String potentiometers P6 and P7 were used to monitor the uplift of the footing of the wall. Twelve spring loaded linear potentiometers (L1 to L12) were mounted on the walls' ends to measure the wall curvature. The relative displacement between the web and boundary elements and between the web and the top and the bottom footings were monitored using spring loaded potentiometers L13 to L19. Finally, the diagonal shear deformations were tracked by string potentiometers P8 and P9. Twenty strain gauges were also installed on the outermost rebars in each wall to capture the yield initiation and strain propagation during loading.

3.2.2 Out-of-plane support

Since the walls represent the plastic hinge zone of a shear wall, which is dominated by flexural deformation, it was expected to have a relatively large top wall rotation. Therefore, out-of-plane support was required to allow the wall to transit and rotate in-plane while preventing out-of-plane deformation. The Canadian code CSA 304-14 [20] clause (16.9.3.2) specifies the allowable unsupported height (h/t+10) as 12 for the walls' thickened ends and 24 for the web. To push the aspect ratio limits for the new proposed system, the supported height was selected to satisfy the code limits for the thickened part of the wall (boundary element) while violating the web part. This decision was based on the calculation of the Euler load for the compression zone [24]. One level of out-of-plane support was provided at the top beam level. The unsupported height, in this case, was 2,360 mm. Thus, the height to thickness ratio is 12 for the boundary element and 26 for the web. Wall W2-C_S^{30} had an out-of-plane failure at $8\Delta_y$. So, it was decided to consider the code limits for the rest of the walls. Two levels of out-of-plane support were provided. The first support was at 1,600 mm height, taken as the first-floor level, and the second one was at the top beam level to prevent out-of-plane movement that could result from the actuators' out-of-plane horizontal forces due to any alignment imperfection.

Four W250x45 steel beams were attached horizontally to the reaction frame columns with their strong axis in the horizontal plane to form the out-of-plane support. Screw jacks were

attached to each beam to transmit the lateral forces from the wall to the beams. At the ends of the jacks from the wall side, Delrin crystalline plastic piece was attached to provide a smooth surface to slide on the nearly frictionless Teflon sheets attached to the loading beam. At the wall side, 6 mm Teflon sheets were provided. In order to form a smooth sliding surface for the screw jacks, the Teflon sheets were attached to 6 mm steel plates at the top beam, while at the floor level, 100 mm Delrin strips were attached to 100 mm-wide ¾" plywood strips.
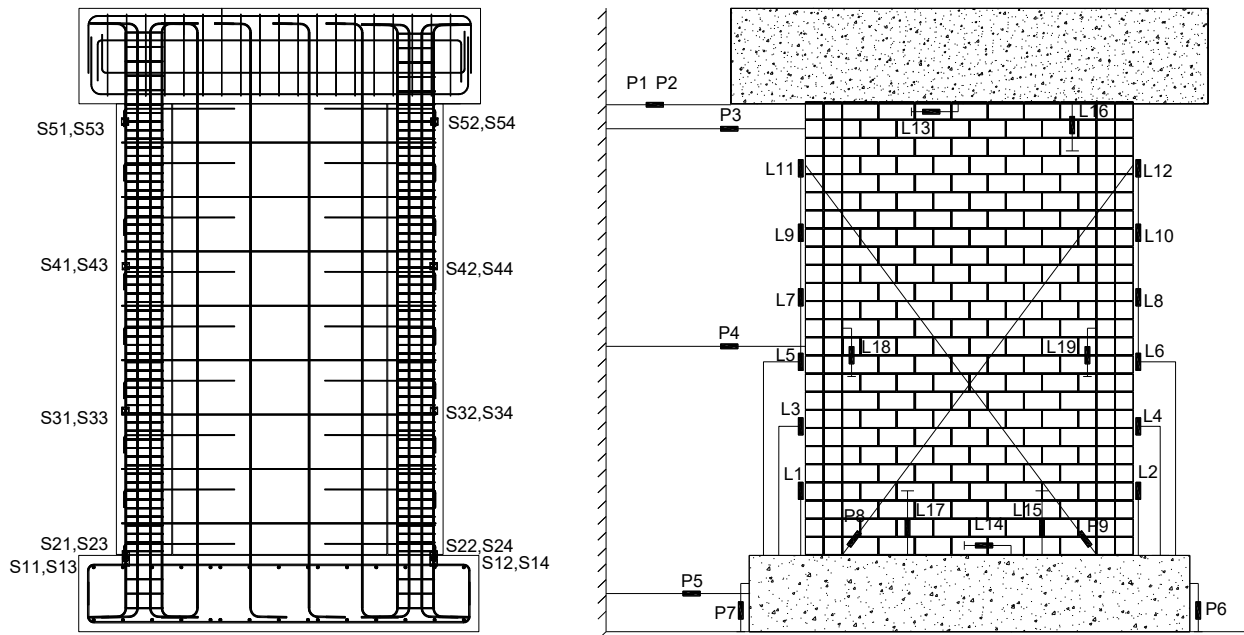
Figure 3.10 Instrumentation arrangement

3.2.3 Loading protocol

The tests and the analysis conducted by Lowes et al. [74] on mid-rise concrete walls concluded that the effective height for mid-rise shear walls ranges from 50% to 70% of the wall height. Based on this conclusion, the selected lateral load shape used in this study was an inverted triangular shape, which provides an effective height of 66.67% of the wall's height Figure 3.11 (a). The horizontal actuator was used to apply the load at the centre of the top-loading beam. The two vertical actuators were used to apply the axial load (corresponding to axial stress of 1.5 MPa) and a top moment to simulate the demanded moment induced from upper stories shear. The top moment, M, calculated using Equation 3-4 was applied along with

51

the applied lateral displacements and its value was varied based on the lateral forces measured by the horizontal actuator:

$$M = F_{V,A \text{ or } B} \times D \qquad\qquad \text{Equation 3-4}$$

where the forces ($F_{V,A \text{ or } B}$) in the vertical actuators A and B, respectively, were calculated using Equation 3-5:

$$F_{V,A \text{ or } B} = \frac{P}{2} \pm \frac{h_{eff} - h_{lap}}{D} F_H \qquad\qquad \text{Equation 3-5}$$

As shown in Figure 3.11 (a), P is the axially applied load, h_{eff} is the effective height of the wall, h_{lab} is the height of the tested walls, D is the horizontal distance between the vertical actuators A and B, and the force (F_H) is the measured force in the horizontal actuator. The term $\left(\frac{h_{eff} - h_{lab}}{D}\right)$ in Equation 3-5 is defined as the uplift factor. The calculated forces in the vertical actuators, $F_{V,A}$ and $F_{V,B}$ were based on (F_H) and its direction. For example, when the horizontal actuator is pushing in the west direction, actuator B will apply a force equal to $\frac{P}{2} + \frac{h_{eff} - h_{lab}}{D} F_H$ while actuator A will apply a force equal to $\frac{P}{2} - \frac{h_{eff} - h_{lab}}{D} F_H$ and vice versa when actuator C is pulling in the east direction.

Figure 3.11(b) shows the displacement control loading protocol of the horizontal actuator. The horizontal excitation is applied in a reversed cyclic pattern. Every two cycles are meant to achieve a specific target displacement. Before reaching the wall's yielding point, which corresponds to the yielding of the outermost vertical reinforcement at the wall footing interface, target displacements are applied as fractions of the estimated yield displacement Δ_y ($0.25\Delta_y$, $0.50\Delta_y$, and $0.75\Delta_y$). The remaining cycles were applied as multiples of the actual yield displacement ($2\Delta_y$, $3\Delta_y$…). The tests were carried out in sequential stages, starting by applying the axial load through the two vertical actuators, and then the horizontal actuator advances until it reaches the required target displacement. This was followed by applying the top moment through the vertical actuators according to the readings of the horizontal actuator's load cell measurement.

(a)

(b)
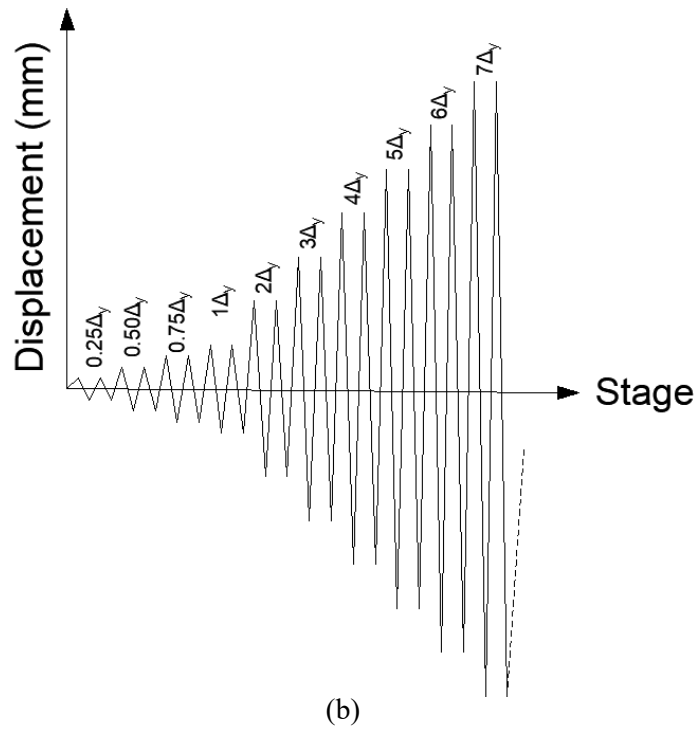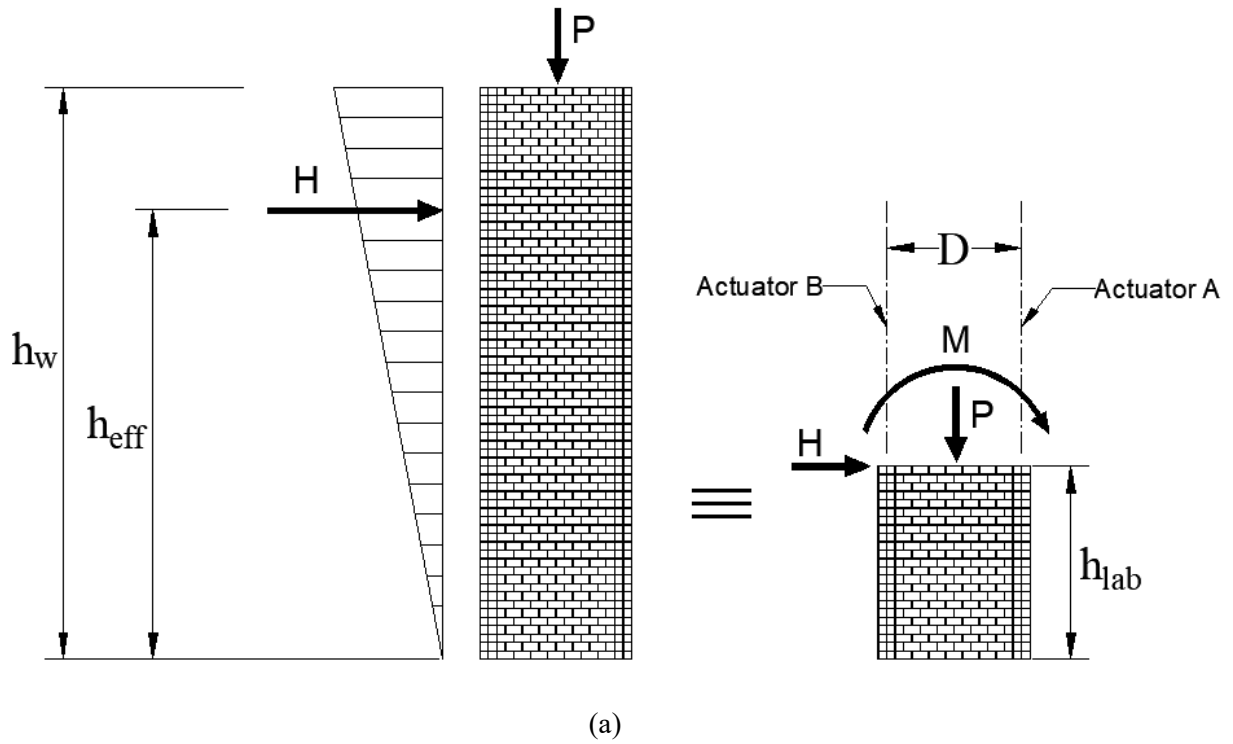
Figure 3.11: (a) Lateral load on wall specimen; and (b) Horizontal actuator displacement control loading protocol

3.2.4 Test control system

The test control was divided into three procedures for applying the axial load, yield finder, and cyclic loading, as shown in Figure 3.12. Figure 3.13 shows the flowchart of the test control system. The test starts with applying half the axial load through the vertical actuators A & B. To start the cyclic loading, while the axial load is already applied on the wall, the control system sends a signal to the horizontal actuator C to apply the horizontal displacement. The load cell in the horizontal actuator measures the applied force and sends the force signal F_H to the control system. If the loading step is still in the loading portion of the loading cycle, the last 10 F_H readings are averaged using an integrated built-in compensation function $F_H(w)$ in the control algorithm. If the loading step is in the unloading portion of the loading cycle, the force measured by the load cell of the horizontal actuator is used as is without compensation $F_H(w/O)$. The horizontally measured force $F_H(w)$ or $F_H(w/O)$ is then used to calculate the forces F_V using Equation 3-5. The force F_V is then applied in the vertical actuators simultaneously with the average horizontal displacement. String potentiometers P1, P2, and P5 readings were used as input in the control system to calculate the average displacement using Equation 3-6.

$$\text{Avg. Displ pot} = \left(\frac{P1+P2}{2}\right) + P5 \qquad\qquad \text{Equation 3-6}$$

The measured force in the horizontal actuator F_H and the calculated average horizontal displacement is also used to generate the force-displacement hysteresis loops, as shown in Figure 3.13. Once the cycle target displacement is reached, the horizontal actuator reveres its direction. Then, the above steps are repeated till the predefined termination criteria "failure" is reached.
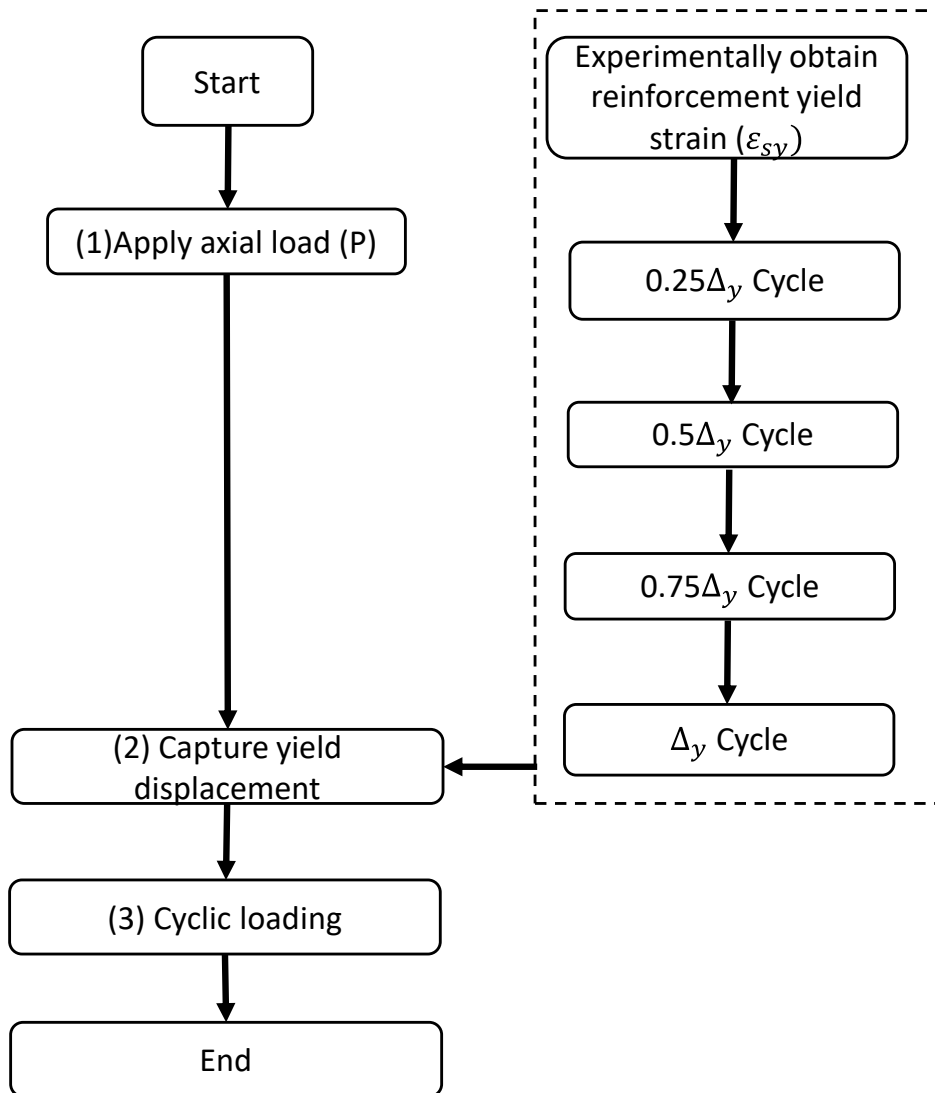
Figure 3.12: Test Procedure
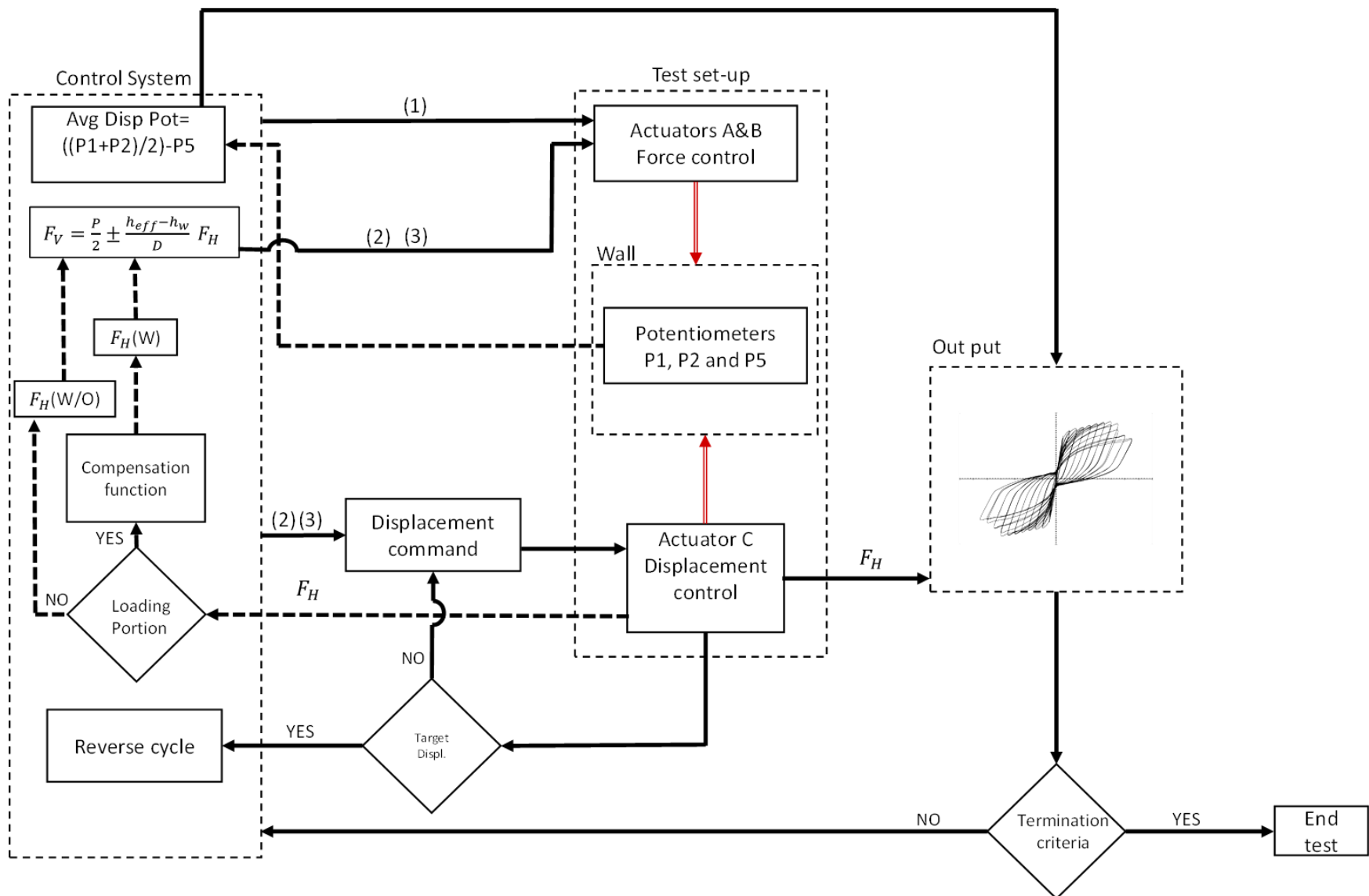
Figure 3.13: Test control flowchart

3.3 Discussion of the test results of $W1\text{-}C_S^{60}$

Wall $W1\text{-}C_S^{60}$ is considered as the reference wall for comparison and to validate the test setup. The test started by applying the axial compressive stress, which simulated the expected gravity loads. This step has successfully passed. However, when the cyclic loading step was initiated, the wall suddenly failed just under the loading beam due to a fault increase in the force applied by the horizontal actuator. This caused a significant increase at the moment applied at the top of the wall, exceeding its load-carrying capacity. Thus, the vertical rebars ruptured at the interface between the top-loading beam and the wall. The failure of the wall is shown in Figure 3.14(a). The programming of the testing protocol was investigated to identify the source of the error. This error was caused by the lack of control of the phase difference between the horizontal and vertical actuators. The control algorithm was accordingly modified to resolve this problem.

The damaged wall was repaired by casting a concrete jacket around the top part of the wall, thus locally repairing the parts with face shell spalling. Epoxy resin was also injected between the loading beam and the top of the wall to guarantee full contact, as shown in Figure 3.14(b). The repaired wall was then used to validate the modified control algorithm and confirm the concept of synchronizing lateral displacement and top moment to test the plastic hinge region of a full wall.

After correcting the error in the control algorithm, and restarting the test on the repaired wall, it was discovered that there was a fluctuation in the feedback signal from the load cell of the horizontal actuator during the loading part of the cycle. This caused instability in the test as the forces in the vertical actuators were a function of the lateral resistance, which was measured by the load cell of the horizontal actuator. To solve this issue, a compensation function was developed to average the last ten readings using a built-in integrated program during the loading portions of the loading cycle, as explained in the test control system section. The results showed a stable behaviour, reflected in the match between the measured forces in the vertical actuators and those calculated based on the horizontal actuator's force using Equation 3-5. The developed stable control algorithm was used to test the remaining two walls.

<center>(a)   (b)</center>

Figure 3.14: (a) Failure of Wall W1-C_S^{60} (b) Repaired Wall W1-C_S^{60}

3.4 Conclusions

A new configuration for RMSW with C-shaped masonry units has been developed and a specially designed experimental test setup equipped with a control system has been built to investigate the response behaviour of the lower panel of RMSW+BE in a 12-storey building subjected to a quasi-static loading protocol. This development fulfils objectives # 1 and 2, stated in subsection 1.5.

Chapter 4

Effect of unsupported wall height and confinement ratio in boundary elements

4.1   Introduction

Using the test setup described in Chapter 3, this chapter aims to investigate the potential of increasing the web unsupported height recommended by CSA S304-14 (Objective #3, Hypothesis # 1) and investigating the effect of increasing the confinement ratio in the boundary elements on the seismic behaviour of RMSW+BE and its failure mode (Objective #4, Hypothesis # 2), stated in chapter 1, subsections 1.4 and 1.5.

For wall W2-C_S^{30}, the CSA S304-14 [20] aspect ratio requirements were stretched to examine if a stronger boundary element has the potential to provide more support to the web. The rationale behind using single out-of-plane support at the loading beam was to avoid the forces that are induced by the actuators due to misalignment. This arrangement was supported by calculating the critical buckling load [24], as presented in Appendix A.

For the third wall (W3-C_S^{45}), in order to prevent the out-of-plane failure, two out-of-plane support levels were provided to laterally support the wall at the loading beam level and first-floor level. The measured response for W2- C_S^{30} and $W3 - C_S^{45}$ are discussed in the following subsections.

4.2   Material Properties

For the two walls presented in this chapter, ready-to-use type S mortar was used to construct the walls. Mortar cubes of 50 x 50 x 50 mm were tested under compression according to the ASTM C270 standard [75]. The average compressive strength of eight mortar cubes was 19.37 MPa (with a coefficient of variation C.O.V.= 8.73%). Grout strength was obtained according to the CSA A179 (2014) [76]. Two types of fine grout mixes were used for grouting the walls. The first type is high strength grout used in the boundary elements, and the second type is normal strength grout used in the web area. The average compressive strength of three grout cylinders was 21.67 MPa (C.O.V. = 7.1%) for the normal strength grout. The average compressive strength of six grout cylinders was 43.33 MPa (C.O.V. = 15.1%) for the high strength grout.

Half-scale masonry units were tested according to the ASTM C140/C140M standard [77]. The masonry units used in these tests were manufactured and supplied by Canada Masonry Design Center (CMDC). The average compressive strength of the half-scale stretcher masonry units was 13.65 MPa (C.O.V. = 7.8%), and for the coupons of the C-shaped boundary elements units was 17.65 MPa (C.O.V. =11.7%). Five fully grouted 4-blocks high boundary element prisms were constructed using C-shaped block units. The average compressive strength of the boundary elements prisms, f_m, was 23.7 MPa (C.O.V. = 11.3%). Five fully grouted 4-blocks high prisms were also constructed in running bond to obtain the compressive strength of the web area. The average compressive strength of the web prisms, f_m, was 10.20 MPa (C.O.V. = 5.8%). The yield and ultimate strength of the #3 vertical steel bars determined from the tensile test, according to the ASTM A615A615M [78], were found to be 460 MPa and 680 MPa, respectively. The yield and ultimate strength of the D4 bars determined from the tensile test, according to ASTM A1064/A1064M [79], were 588 MPa and 633 MPa, respectively.

4.3   Failure modes

For the second wall W2-C_S^{30}, the test was initiated by applying the axial load and initiating the reversed cyclic lateral and top moment loads. The first crack was observed at $4\Delta_y$ in the first cycle at the 5th course, as a horizontal crack in the boundary element at the tension side. Face shell spalling started at the second course at $4\Delta_y$ in the second cycle. The cracks were found to be concentrated at the bed joints and started from the edge of the wall, and then propagated to the web, as shown in Figure 4.1 (a). The loading cycles continued until the 8th push cycle, at which the wall failed out-of-plane, as shown in Figure 4.2(a).

Wall W3-C_S^{45} has an aspect ratio of 10.6 and applied axial stress of 1.5 MPa. The wall response was dominated by flexural behaviour, with hairline cracks appearing in the bed joints at $1\Delta_y$. The first visible horizontal flexural cracks extended along the first storey height, and their spacing was equivalent to two courses at $3\Delta_y$. These cracks were observed in the bed joints at the boundary elements and the web areas. By increasing the applied loads, more horizontal cracks were developed at the bed joints in the boundary elements. During larger lateral drift cycles, the wall deformation was primarily concentrated at one large flexural crack at the wall base, approximately up to 3.2 mm wide. The other flexural cracks did not exhibit similar behaviour. The crack pattern for wall W3-C_S^{45} is shown in Figure 4.1 (b). No sliding was recorded. The face

shell at the boundary elements started to spall during the cycles corresponding to lateral drifts of 1.2%, showing that the grout core was intact. The observed buckling of the vertical web reinforcement is attributed to the lack of confinement at the sixth cycle, which caused degradation in the measured lateral force. In the boundary element zone, no vertical reinforcement buckling or crushing in the grouted core was observed. The wall lost about 20% of its lateral capacity in the sixth cycle and failed in the second cycle of $8\Delta_y$, as illustrated in Figure 4.3 (b).

Although the second level of out-of-plane support at the first-floor level did not significantly improve the ductility factor of the tested walls, it changed the failure mode from out-of-plane failure (as observed in wall $W2\text{-}C_S^{30}$) to in-plane failure due to global buckling of the boundary element and web crashing. The presence of the second out-of-plane support at the first-floor level impacted the cracks' distribution in tested walls. As shown in, diagonal cracks were observed. The cracks were not concentrated in the bottom half of the wall, as observed in wall $W2\text{-}C_S^{30}$.

As shown in Table 4.1, wall $W3\text{-}C_S^{45}$ had almost the same yielding strength, ultimate strength, and displacement as wall $W2\text{-}C_S^{30}$. This result is predicted by the CSA S304-14 [20]. However, by comparing the load-deformation relationships shown in Figure 4.3, wall $W3\text{-}C_S^{45}$ has larger loops than wall $W2\text{-}C_S^{30}$, which means that it dissipated more energy. This could be attributed to the difference in the amount and the distribution of cracks in both walls due to the absence of the out-of-plane support at the first-floor level in $W2\text{-}C_S^{30}$.

Similar to wall $W2\text{-}C_S^{30}$ the spacing of hoops in $W3\text{-}C_S^{45}$ was less than that required by CSA S304-14 [20] bar buckling prevention requirements. This resulted in stronger boundary elements. By increasing the strength of the boundary elements, other failure mechanisms were triggered, e.g., global buckling of the boundary element and the failure in the web of $W3\text{-}C_S^{45}$.
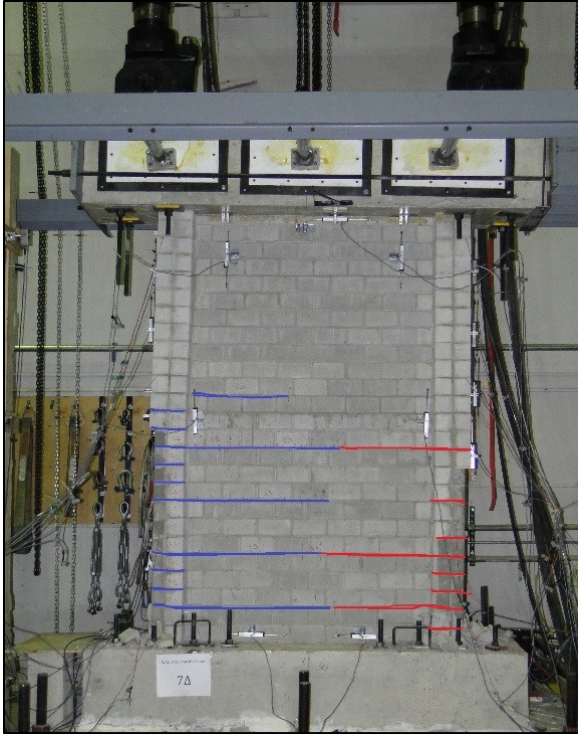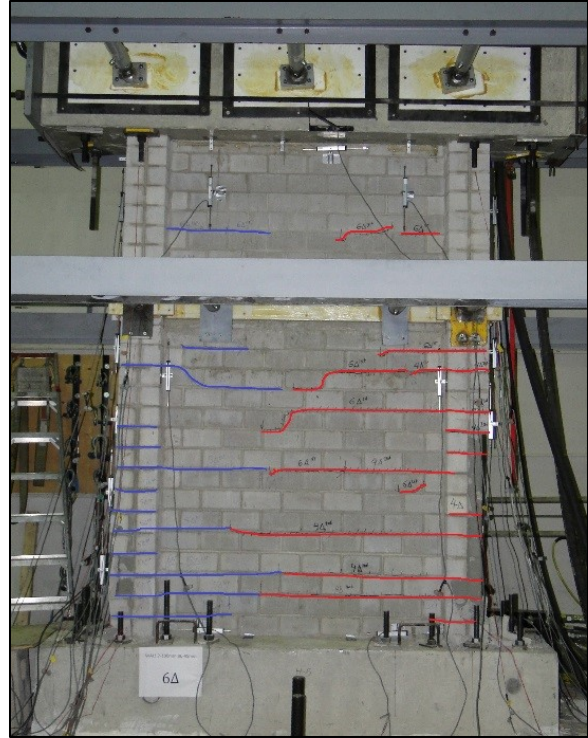
Figure 4.1: (a) Crack pattern in W2-C$_S^{30}$; (b) Cracks pattern in W3-C$_S^{45}$

Rupture and buckling of reinforcement

Web crushing
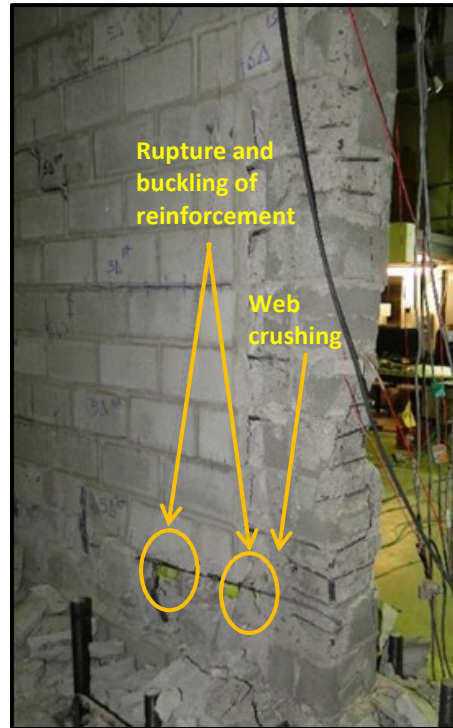
(a)   (b)

Figure 4.2: (a) W2-C$_S^{30}$ failure (b) W3-C$_S^{45}$ failure

Table 4.1: Experimental and predicted forces and displacements

Wall		Q_y (kN)	Q_u (kN)	Δ_y mm	Δ_u mm	μ_Δ
W2-C_S^{30}	Experimental	34.13	51.67	5.6	39.2	7
	Predicted	35.41	47.86	3.07	30.03	9.7
	Relative error	3.75%	-7.37%	-45.18%	-23.39%	-
W3-C_S^{45}	Experimental	35.25	50.39	5.4	43.2	8
	Predicted	35.41	47.86	3.07	30.03	9.7
	Relative error	0.45%	-5.02%	-43.15%	-30.49%	-

(a)   (b)
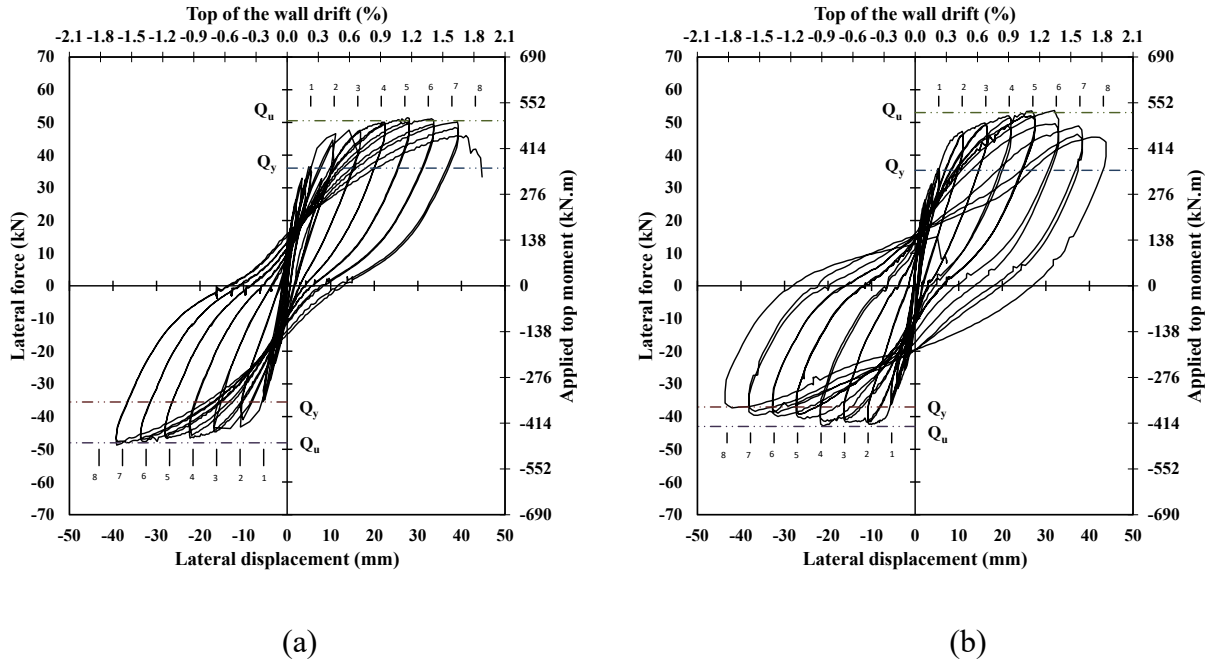
Figure 4.3: Lateral load-deformation relationship (a) W2-C_S^{30} (b) W3-C_S^{45}

4.4   Force-displacement relationship

The predictions of the yield lateral strength, Q_y and the nominal lateral strength, Q_u, were based on CSA S304-14 [20] provisions. The predefined maximum compressive strain was 0.0025, as per clause 16.8.6, and the equivalent rectangular masonry stress block was taken as $0.85f'_m$, as per clause 10.2.6. The predicted wall flexural capacity given in Table 4.1 is the

nominal capacity calculated without considering the material reduction factors, i.e., assuming that ϕ_m and $\phi_s = 1.0$. The yield displacement Δ_y and the ultimate displacement Δ_u were predicted using Equations 4-1 and 4-2 [25]:

$$\Delta_y = \phi_{y,th} \frac{h_{eff}^2}{3} \qquad\qquad \text{Equation 4-1}$$

$$\Delta_u = \Delta_y + (\phi_{u,th} - \phi_{y,th})l_p(h_{eff} - 0.5l_p) \qquad\qquad \text{Equation 4-2}$$

where $\phi_{y.th}$ and $\phi_{u,th}$ are the theoretical yield and ultimate curvature, respectively, h_{eff} is the wall's effective height and l_p is the height of the plastic hinge. The latter was taken as $0.5\,l_w + 0.1h_{eff}$, as per the CSA S304-14 [20] clause 16.9.4. The predicted values of Δ_y and Δ_u were 3.07 mm and 30.03 mm, respectively. The positive lateral force and displacement were measured in the push direction when the horizontal actuator pushed the wall to the west direction and vice versa. The lateral capacities of the walls are shown in Table 4.1, in terms of the measured yield lateral force Q_y and the measured ultimate lateral force Q_u.

Wall W2-C_S^{30} had a similar response in both the push and pull directions. The over-strength factor, Q_u/Q_y, was found to be approximately 1.39. The load-deformation relationship for wall W2-C_S^{30} is shown in Figure 4.3(a). The force values shown in Figure 4.3 were corrected to include the horizontal component of the vertical actuators. Figure 4.4 shows the deformed shape of the tested wall. During the test, the vertical actuators A and B were swinging in the east and west directions following the movement of the horizontal actuator C. Due to the in-plane swing of the vertical actuators during the in-plane cyclic displacements, the axial forces in the vertical actuator will have components in the X and Y directions. The values of the vertical and horizontal force components are a function of the value of the lateral displacement since the value of the initial length of the vertical actuators, h_A is constant and equal to 2.83 m. By studying the deformed shape of the tested wall and the forces in the vertical actuators, it can be seen that the total lateral resistance of the wall is the summation of the measured lateral force in the horizontal actuator C, F_H and the horizontal component of the vertical actuators A and B, $F_{v,Ax}$ and $F_{v,Bx}$.

The yield displacement was considered as the displacement at the onset of the vertical reinforcement bars' yield at the end of the wall. Since no force degradation was observed, the

ultimate displacement was considered as the maximum displacement recorded for the wall. Table 4.1 shows the measured yield Δ_y and ultimate displacement Δ_u and the displacement ductility ratio μ_Δ. The ductility ratio μ_Δ was calculated as the ratio between the measured values of Δ_y and Δ_u. For W2-C_S^{30} the measured displacement ductility ratio μ_Δ is 7.

Figure 4.3(b) shows the lateral force-displacement relationship for wall W3-C_S^{45}. The push direction is when the west side of the wall is under compression, and the pull direction is when the east side of the wall is under compression. The force-deformation relationship included the horizontal component of the vertical actuators. The yield point is defined as the onset of yielding at the outermost bars. The average yield lateral load Q_y was 35.25 kN. The corresponding average displacement for the yield lateral load was 5.4 mm, which was used as a displacement multiplier factor for the next cycles. The average measured ultimate lateral load was 50.39 kN, corresponding to a displacement of 32.4 mm.

Table 4.1 shows the comparison between the predicted and the experimentally measured response. The relative error percentage was calculated as the ratio of the difference between the predicted and experimentally measured values to the experimentally measured value. For W2-C_S^{30}, the comparison shows that the predictions can approximately capture the yield strength but underestimate the nominal lateral capacity by 7.37%. For the displacement predictions, Equations 4-1 and 4-2 underestimated the yield and ultimate displacements by 45.18% and 23.39%, respectively. For the ultimate displacement, the prediction errors could be due to the difference in the compressive strain value used by the code and that determined experimentally, and due to the length of the plastic hinge. For W3-C_S^{45}, the lateral capacity at yield has a prediction error of 0.45%, while the ultimate lateral capacity was underestimated by 5%. The comparison shows that the code provisions are on the conservative side.
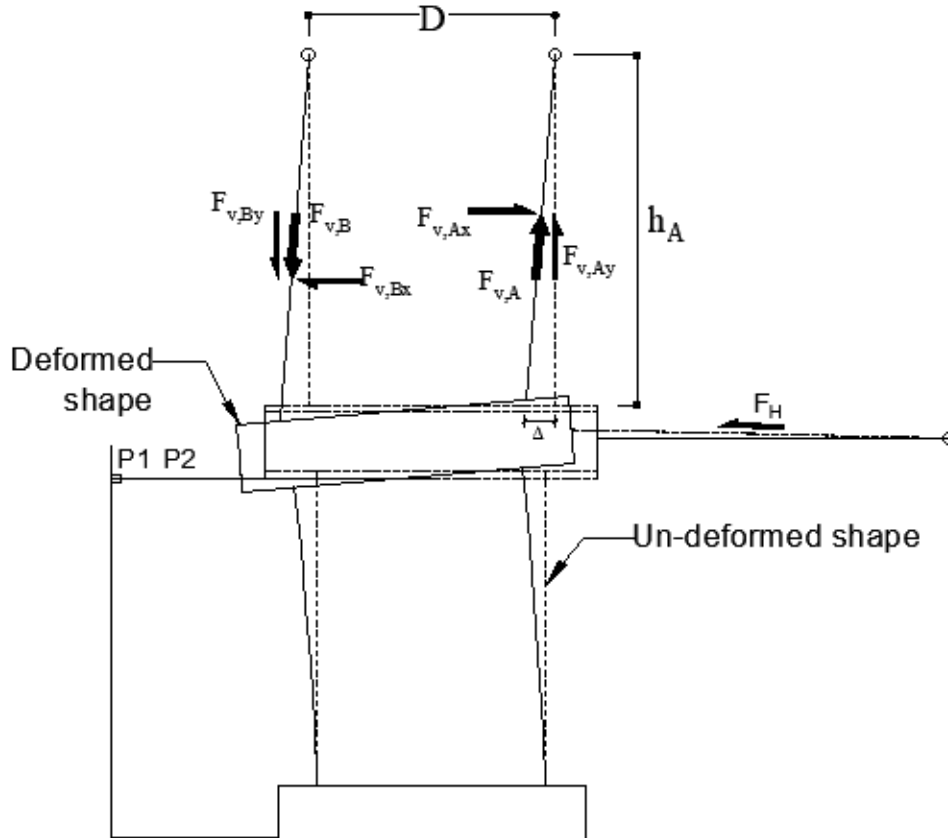
Figure 4.4: Deformed shape of the tested wall.

4.5 Axial compressive strain

The relation between the average measured compressive strain at the wall's ends and the normalized measured lateral force for wall W2-C_S^{30} is shown in Figure 4.5(a). The vertical displacements at the end of the walls were measured at 340 mm, 680 mm, and 1,020 mm from the top of the wall footing. The discontinuity in the measurement was due to the face shell spalling and losing the brackets that held the spring potentiometers. The average maximum measured compressive strain was 0.0075 mm/mm.

The average measured compressive strain at the ends of the wall and the normalized measured lateral force for wall W3-C_S^{45} are shown in Figure 4.5(b). The average maximum measured compressive strain was 0.012 mm/mm, which is approximately six times the limit specified in the CSA S304-14 [20] standard as 0.0025mm/mm.
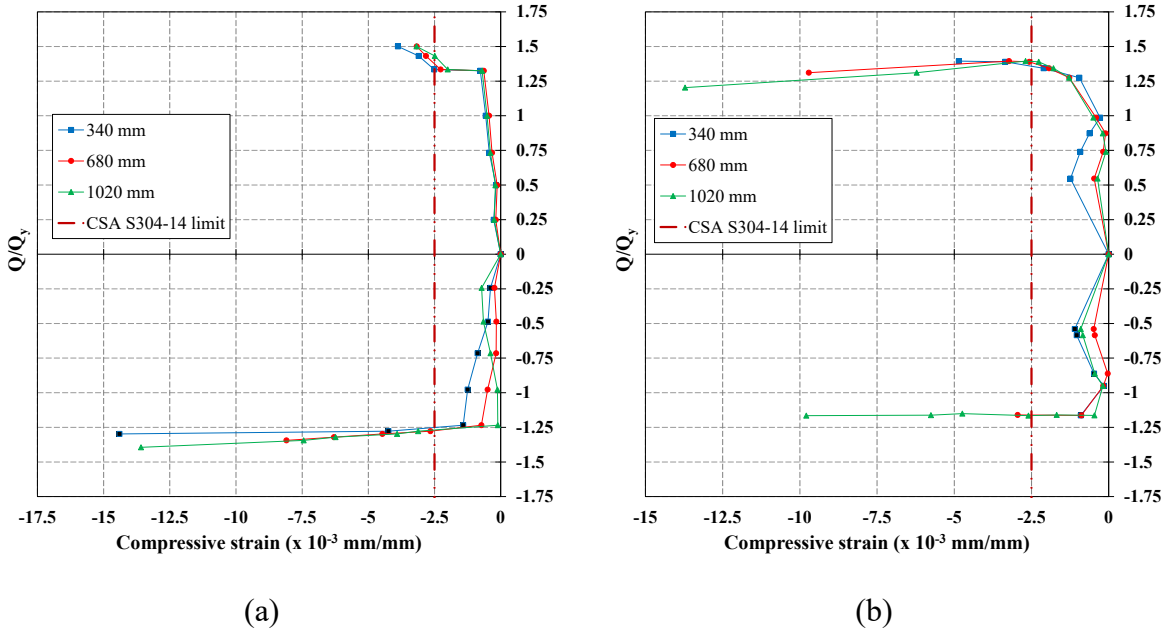
Figure 4.5: Measured compressive strain for (a) W2-C_S^{30} (b) W3-C_S^{45}

4.6   Curvature

The average curvature over the wall height was determined based on the strain profiles at different levels along the wall height. The theoretical ultimate curvature, $\phi_{u,th}$, was calculated using an ultimate strain, ε_{mu} = 0.0025. Both walls have twelve spring potentiometers (six on each side) attached to the ends of the walls to measure the axial deformation. The calculated ultimate and yield curvature for both walls were 1.69×10^{-5} and 1.18×10^{-6} rad/mm, respectively. The measured axial deformations were used to calculate the average curvature over the height of the walls. In addition, the theoretical yield curvature $\varphi_{y,th}$ and the theoretical ultimate curvature $\varphi_{u,th}$ were calculated for both walls using the first principles for concrete section analysis.

For wall W2-C_S^{30}, the average curvature profile is shown in Figure 4.6(a). Robazza et al. [18] studied the cycle of average axial strain versus out-of-plane displacement in an end zone of a rectangular RMSW subjected to in-plane reversed cyclic loading. They observed that wide flexural cracks were uniformly distributed over the wall height when the end of the wall was under tension. When the cycle was reversed, and a compression load was applied, the rapid onset of out-of-plane displacement occurred. At this point, two mechanisms of response were postulated. First, if the out-of-plane displacement exceeds its critical value, out-of-plane failure

will occur, and this was what happened in the 7th push cycle for W2-C$_S^{30}$. The second mechanism is when the out-of-plane displacement is less than the critical value. In this case, the flexural cracks will close, restoring the near-vertical alignment of the wall to its position near the time of load reversal, with the presence of small residual out-of-plane displacements. This mechanism can explain why the curvature profile for W2-C$_S^{30}$, could not be accurately captured using the strain measurements at the ends of the wall. The comparison between the measured and theoretical curvatures showed that both yield and ultimate curvatures are overestimated.

The curvature profile for W3-C$_S^{45}$ is shown in Figure 4.6 (b). The curvature profile for the 7th and 8th cycles was not captured due to face shell spalling. The maximum measured curvature was 6×10^{-5} rad/mm. The measured yield curvature value was matching the calculated theoretical value as shown in Figure 4.6(b). The experimental plastic hinge length can be defined as the average measured height from the base, where the curvature is inelastic and greater than the yield curvature, up to the point where the measured curvature is equal to the yield curvature. The measured plastic hinge height was approximately 1.8 m, representing almost 15% of the wall's effective height. The comparison between the measured and theoretical curvature showed that yield curvature was accurately estimated, and the ultimate curvatures were overestimated.

As indicated earlier, the loading beam was allowed to rotate during the test, and the angle of rotation for tested specimens was found to be in the range from 0 degrees at the start of the test to approximately 3.1 degrees at the end of the test. The rotation angle was determined using a high-resolution camera that can capture up to 400 frames per loading cycle.
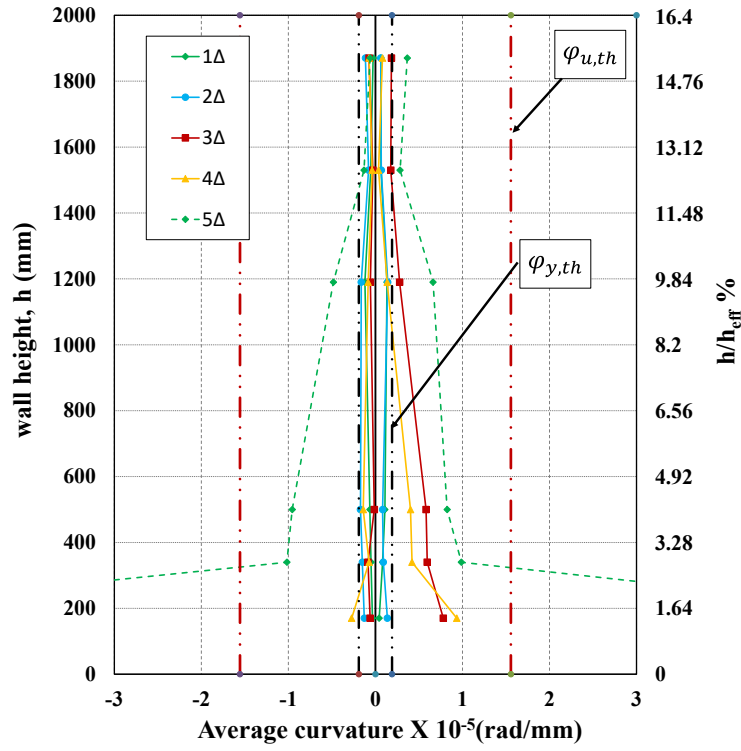
(a)
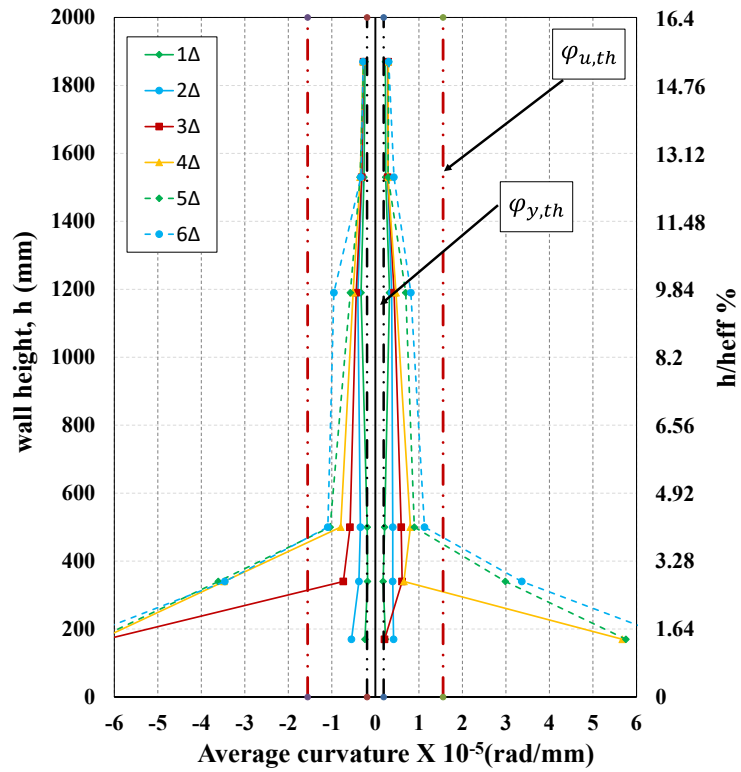
(b)

Figure 4.6: Measured curvature for (a) W2-C_S^{30} (b) W3-C_S^{45}

4.7   Effective secant stiffness degradation

Calvi et al. [80] proposed the use of an effective secant stiffness ($K_e = Q/\Delta$) calculated from the load-displacement response of the inelastic structure at the desired level of top displacement, as a more reliable estimation of the structure's effective design period. Figure 4.7 shows the relation between the normalized effective stiffness (K_e/K_i) and the displacement ductility ratio (Δ/Δ_y), where K_i is the measured initial effective stiffness for the first cycle (0.25Δ). For both walls W2-C_S^{30} and W3-C_S^{45}, the effective stiffness measured at yield, represented by the horizontal double dotted line in Figure 4.7, was significantly reduced by up to an average value of 37% of the initially measured stiffness. In addition, the difference in the failure mode and the confinement ratio between the two walls have almost no effect on the measured effective stiffness.

(a)
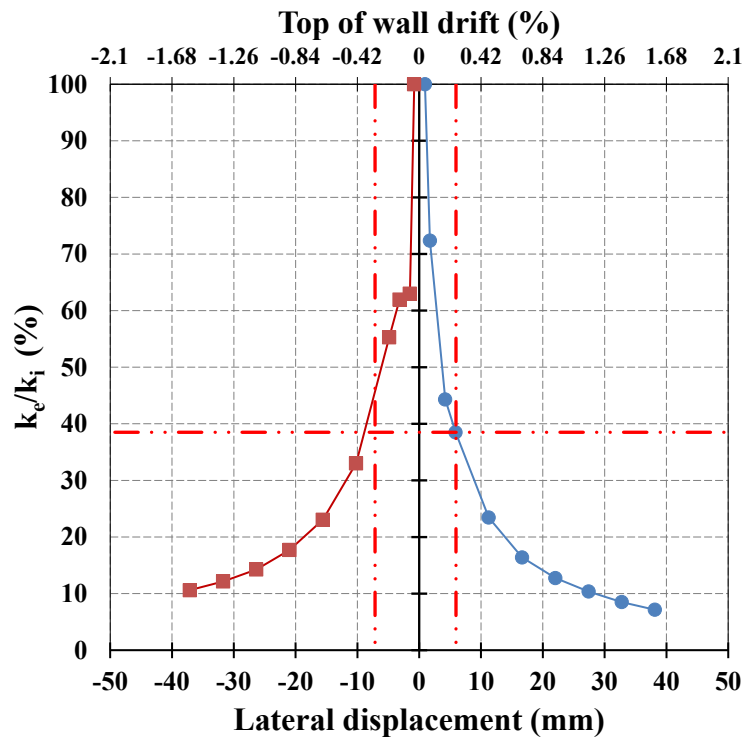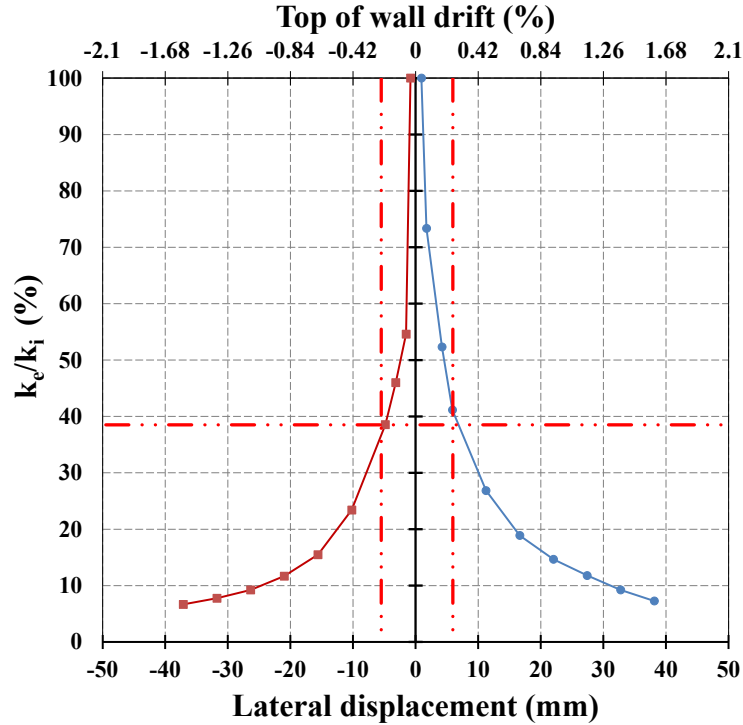
Figure 4.7: Measured normalized stiffness for (a) W2-C_S^{30} (b) W3-C_S^{45}

4.8   Dissipated energy

When a structural wall experiences a flexural bending beyond its elastic limit, a plastic hinge region, where inelastic rotations are concentrated and substantial seismic energy dissipation occurs, will be formed in the lower portion of the wall [15]. The load-deformation relationship shown in Figure 4.3 demonstrated larger loops generated by flexural deformations, indicating high levels of energy dissipated in W3-C_S^{45}. The dissipated energy per cycle was calculated as the area inside the hysteresis loop in each cycle. The relation between the normalized dissipated energy and the displacement ductility ratio is shown in Figure 4.8. Two normalization methods were used. In Figure 4.8 (a), the dissipated energy in each cycle (E) was normalized with respect to the amount of the dissipated energy at yield (E_y). Both walls have almost the same ratio between the normalized dissipated energy (E/E_y) at different displacement ductility levels (Δ/Δ_y). In addition, the dissipated energy increased with the increase of the displacement ductility ratio. In Figure 4.8 (b), the dissipated energy in each cycle (E) was normalized with respect to the amount of the input energy (E_{input}) calculated as the area under the skeleton curve at a

particular displacement ductility ratio. The figure shows that W2-C_S^{30} had a lower capability to dissipate the input energy than W3-C_S^{45}. This difference can be attributed to the out-of-plane deformation in W2-C_S^{30}. Vertical bars positioned at the extreme tension edge of the section will be subject to significant tensile strains when the wall exhibits substantial in-plane curvature. At this point, uniformly distributed horizontal cracks over the plastic hinge height occur. The tensile stress in these bars becomes zero during the subsequent unloading. The compression stresses in these bars will gradually rise when the direction of the lateral load changes. The vertical reinforcement must resist the entire internal compression within the section unless the cracks close. At that point, the vertical steel's stiffness to out-of-plane lateral deformation is low, which contributes to the out-of-plane instability by allowing out-of-plane displacements to rise quickly. However, if the cracks close before the entire section of the wall that had previously been in tension is put into compression, masonry compressive stresses will engage in the area, increasing its stiffness to out-of-plane lateral deformation and helping to prevent instability [24]. The effect of the out-of-plane deformation on the in-plane dissipated energy started at yield. With the increase in the wall's curvature, the out-of-plane deformation increases, which contributes to dissipating a portion of the input energy [24].

(a)

(b)
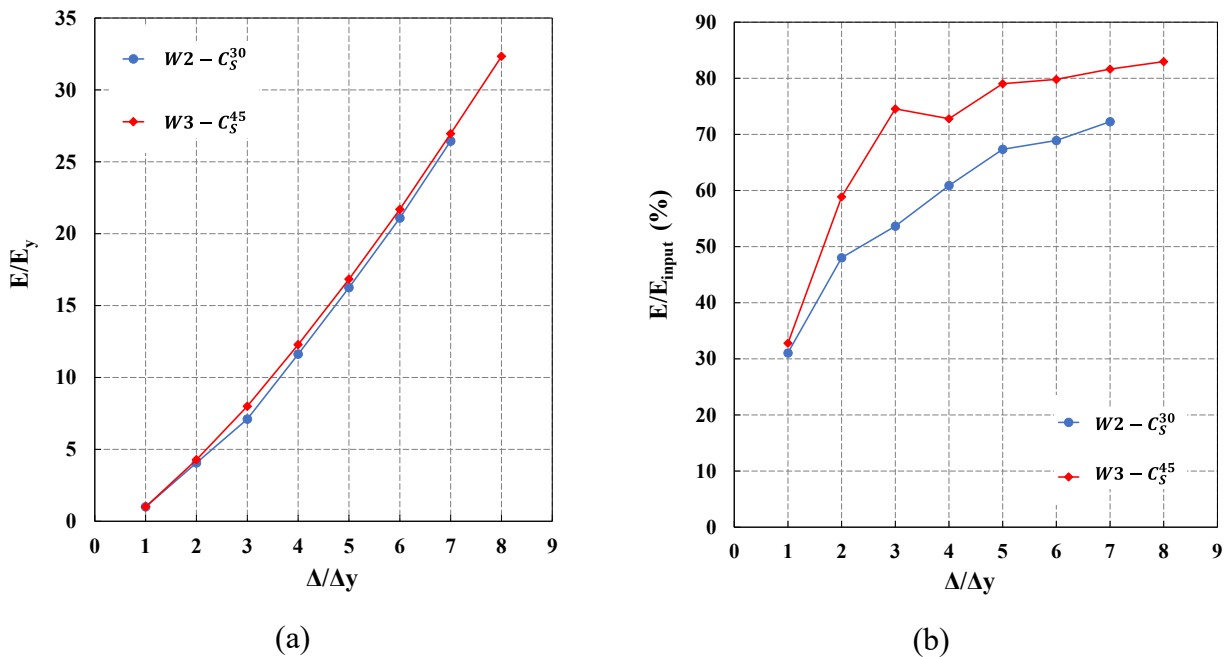
Figure 4.8: Normalized energy dissipation capacity (a) normalized over energy dissipated at the yield (b) normalized over input energy.

4.9 Conclusions

Test results showed that the proposed system could provide the lateral strength and ductility required to resist earthquake events and that the average measured compressive strain was almost four times the limit specified in CSA S304-14. The results also showed that single out-of-plane support at the loading beam level was inadequate, leading to out-of-plane failure. When additional out-of-supports were provided, the failure mode changed to web crushing and buckling of vertical web reinforcement. The test results showed that the proposed experimental setup and its control system has the capability to apply the lateral forces and top moments simultaneously. Therefore, it can mimic the loading conditions on the plastic hinge zone of a 12-storey high masonry wall. The proposed system was used to investigate the effect of increasing the confinement ratio in the boundary elements on the seismic response of the RMSW.

From the constructability point of view, it was proved that the C-shaped units provided the lateral strength as designed and provided the engineer with the option of increasing the vertical and confinement reinforcement, as well as the flexibility to change the boundary element length. Additionally, it is estimated that using C-shaped masonry units to form the boundary elements can reduce the required manpower and the time needed to build the wall by 50% and 67%, respectively, compared to the walls constructed using regular stretcher units.

The two tested RMSW representing the lower panel zone of a 12-storey building (plastic hinge zone) were constructed with similar dimensions and vertical and horizontal reinforcement configuration but with different confinement ratios in the boundary element. The test results showed that the proposed system could provide the lateral strength and ductility required to resist earthquake events. The tested walls were dominated by a flexural failure mode, which is characterized by the yielding of vertical reinforcement and the development of horizontal cracks. However, no vertical reinforcement buckling or crushing in the grouted core was observed due to the presence of additional confinement reinforcement in the boundary elements.

The test results showed that single out-of-plane support at the loading beam level, which partially violated the CSA S304-14 [20] requirements, was inadequate, and an out-of-plane failure occurred at almost the first 8th push cycle at the mid-height of the wall. Nevertheless, the wall had a ductility factor of 7 and maintained the lateral and vertical capacity till the last cycle. When two out-of-plane support levels were provided at the loading beam level and first-floor

level, the wall failed at the second 8th push cycle due to web crushing and buckling of vertical web reinforcement, which in turn applied a lateral pressure on the grout and the face shell and caused wall failure.

The result showed that the out-of-plane failure affected the curvature of the wall, especially for those cycles prior to reaching the out-of-plane displacement critical value. The effective lateral stiffness for RMSW with c-shaped boundary elements did not get affected by the confinement ratio or the failure mode. Lastly, both walls W2-C_S^{30} and W3-C_S^{45} have almost the same ratio between the normalized dissipated energy (E/E_y) at different displacement ductility levels. However, the out-of-plane failure reduced the capability of the wall to dissipate the input energy.

The results also showed no observed sliding between the boundary elements and the web, validating the strain compatibility assumption of the "plane section remain plane," as stated in CSA S304-14 [20] design provisions.

In summary, the results of this chapter demonstrated the great potential of RMSW with MBEs formed by the proposed C-shaped masonry blocks to provide the strength and ductility required for lateral force resisting systems in medium to high rise masonry buildings. However, stronger boundary elements were not able to provide better out-of-plan support to the web. Thus, there is no potential to increase the web un-supported height recommended by CSA S304-14. In this case, hypothesis #1 is not confirmed valid. The comparison between the three tested walls with regards to the confinement ratio in the boundary elements was not established due to the failure mode of walls W1-C_S^{60} and W2-C_S^{30}. Hypothesis #2 will be checked numerically in chapter 6.

Chapter 5

Effect of boundary element details

5.1   Introduction

Using the test setup described in chapter 3, this chapter aims to investigate the effect of changing the boundary element size and vertical reinforcement ratio on the seismic behaviour of the RMSW+BE (Hypotheses #3 and #4). In addition, the possibility of increasing the ductility reduction factor, R_d, recommended by NBCC 2015 [21], was also experimentally investigated (Hypothesis #5). Due to the early face shell spalling observed in phase one of the experimental work, masonry units with higher strength were used in phase two. In phase two, three RMSW+BE were built and tested.

Oh et al. [81] investigated the effect of modifying boundary element details on the shear wall's deformation capacity by testing four reinforced concrete shear walls. According to Oh et al., increasing the confinement in the boundary elements can greatly boost the wall's deformation capability. Changing the wall cross-section from rectangular to barbell shape, while maintaining the same vertical and transverse reinforcement ratios in the boundary elements had a small influence on the wall response. A critical review of the available literature showed that there is a shortage of previously tested RMSW+BE. Except for one wall examined by Shedid et al., the boundary elements in these examined walls were formed from ordinary stretcher blocks [8]. The use of stretcher masonry units limits the geometrical form of the boundary elements to a square cross-section and the vertical reinforcement to four bars [82]. Furthermore, utilizing

standard stretcher units without reshaping them manually cannot accommodate confinement hoops with different spacing to achieve the code requirements of the vertical reinforcement buckling prevention ties [83].

Comparing W4-$C_{Lb,VRFT}^{190,8}$ and W5-$C_{Lb,VRFT}^{290,8}$ would determine the effect of changing the boundary element length when keeping the same amount of vertical reinforcement on the wall's behaviour, whereas comparing W5-$C_{Lb,VRFT}^{290,8}$ and W6-$C_{Lb,VRFT}^{290,6}$ would investigate the effect of boundary element vertical reinforcement ratio on the wall's response. All walls were subjected to 1.5 MPa vertical stress.

5.2 Materials

For the three walls presented in this paper, the concrete compressive strength, f_c, was obtained according to ASTM C39M-15 [84] by averaging the results of three cylindrical specimens (100 mm in diameter, 200 mm high). The concrete average compressive strength of the top-loading beam was 48.3 MPa (with a coefficient of variation C.O.V. = 10.8%), and the average compressive strength of the concrete in the bottom footing was 41.0 MPa (C.O.V. = 4.8%). The masonry units used in these tests were manufactured and supplied by the Canada Masonry Design Center (CMDC). The average compressive strength f_b of the three half scale standard stretcher masonry units was 34.7 MPa (C.O.V. = 7.6%), and for the four coupons of boundary element units, f_{be} was 22.8 MPa (C.O.V. = 4.8%) according to CSA A165-14 [85] and ASTM C140-15 [77]. Ready-to-use type-S mortar was used to construct the walls. Mortar cubes of dimensions 50 x 50 x 50 mm were tested according to the CSA A179-14 [86] and ASTM C109M-13 [87] standards. The average compressive strength of the ten mortar cubes was 15.1 MPa (C.O.V.= 16.1%). Two types of fine grout mixes were used for grouting the walls. The first type was high strength grout used in the boundary elements, and the second was normal strength grout used in the wall's web. The average compressive strength of the nine normal strength grout cylinders was 31.3 MPa (C.O.V. = 9.5%). The average compressive strength of the twelve high-strength grout cylinders was 43.2 MPa (C.O.V. = 15.5%). The grout strength was obtained according to CSA A179-14 [86]. Five fully grouted four-block high boundary element prisms were constructed using C-shaped block units and tested according to CSA S304-14 [20]. The average compressive strength of the boundary element prisms, f_m, was 25.4 MPa (C.O.V.= 8.0%). Eight fully grouted four-block high prisms were also constructed using standard stretcher

76

blocks in running bonds to obtain the compressive strength of the wall's web. The average compressive strength of the three web prisms, f_m, was 11.3 MPa (C.O.V. = 12.0%). The yield and ultimate strength of #3 vertical steel bars were obtained according to ASTM A615M-15 [78] and found to be 460 MPa and 680 MPa, respectively. The yield strengths of the D4 and D8 structural deformed wires determined from the tensile test were 590 and 535 MPa, respectively.

5.3 Theoretical response of the walls

The theoretical responses of the walls were determined and are summarized in Table 5.1. The predicted wall flexural capacity shown in Table 5.1 is the probable moment capacity calculated without taking into consideration the material strength reduction factors (i.e., $\phi_m = \phi_s = 1.0$) to predict the actual wall resistance. This value was used to check the capacity of the test setup. From the tensile test for the vertical steel rebars, the obtained yield strain and the yield stress were 0.0023 and 460 MPa, respectively. The yield lateral load (Q_y), yield curvature (φ_y) and yield displacement (Δ_y) were obtained using elastic analysis for the wall section. The extreme fibre ultimate compressive strain in the grouted masonry boundary element units (ε_{mu}) was calculated using Equation 5-1 driven from CSA S304-14 cl.16.11.6 [20][14] as follows:

$$\varepsilon_{mu} = \frac{A_{sh}A_{ch}f_{yh}}{6K_nA_gf'_mSh_c} - \frac{1}{300} \qquad \text{Equation 5-1}$$

where A_{sh} is the total effective area in each of the principal directions of the cross section within spacing S between the reinforcement hoops, A_{ch} is the cross-sectional area of the core of the boundary element, f_{yh} is the specified yield strength of hoop reinforcement, k_n is the ratio between the number of vertical reinforcement bars n to $(n-2)$, A_g is the gross cross-sectional area of masonry, f'_m is the compressive strength of masonry normal to the bed joint and h_c is the dimension of the core of the rectangular section measured perpendicular to the direction of the hoop bars to the outside of the confinement hoop.

Moreover, the ultimate lateral loads $Q_{u,0.0025}$ and $Q_{u,\varepsilon mu}$ were calculated using the equivalent stress block described in CSA S304-14 [20] assuming that ε_{mu} is either equal to 0.0025 or the value obtained from Equation 5-1, respectively. Subsequently, the corresponding ultimate curvatures ($\varphi_{u,0.0025}$, $\varphi_{u,\varepsilon mu}$) and ultimate displacements ($\Delta_{u,0.0025}$, $\Delta_{u,\varepsilon mu}$) were calculated accordingly. The ultimate displacement values were calculated at the top of the wall. As the plastic hinge length L_p affects the value of the plastic deformation, the ultimate wall

displacement was obtained using three plastic hinge length models. Equations 5-2, 5-3 and 5-4 were proposed by Paulay and Priestley [15], CSA S304-14 [20], and Bohl and Adebar [39], respectively.

$$L_{p1} = 0.5L_w \qquad\qquad \text{Equation 5-2}$$

$$L_{p2} = 0.5L_w + 0.1h_w \qquad\qquad \text{Equation 5-3}$$

$$L_{p3} = (0.2L_w + 0.05h_w)\left(1.0 - 1.5\,{}^P/_{f'_m A_g}\right) < 0.8L_w \qquad\qquad \text{Equation 5-4}$$

Table 5.1: Theoretical response of the walls

	W4-$C_{L_b,VRFT}^{190,8}$	W5-$C_{L_b,VRFT}^{290,8}$	W6-$C_{L_b,VRFT}^{290,6}$
Q_y (kN)	54.04	51.62	51.58
C_y (mm)	403.03	408.80	412.89
ϕ_y (rad/mm)	1.89E-06	1.96E-06	1.97E-06
Δ_y (mm)	3.57	3.71	3.72
$Q_{u,0.0025}$ (kN)	75.48	77.03	71.23
$C_{0.0025}$ (mm)	179.25	196.13	200.32
$\phi_{0.0025}$ (rad/mm)	1.39E-05	1.27E-05	1.25E-05
c/l_w	0.10	0.11	0.12
$Q_{u,\varepsilon mu}$ (kN)	75.48	77.31	71.71
$C_{\varepsilon mu}$ (mm)	161.52	190.09	198.35
$\phi_{\varepsilon mu}$ (rad/mm)	2.18E-05	2.70E-05	2.11E-05
c/l_w	0.09	0.11	0.11
$\Delta_{0.0025}$ (Using LP1)	23.74	21.83	21.39
$\Delta_{\varepsilon mu}$ (Using LP1)	36.83	45.78	35.93
$\Delta_{0.0025}$ (Using LP2)	37.17	33.74	32.99
$\Delta_{\varepsilon mu}$ (Using LP2)	58.95	73.43	57.08
$\Delta_{0.0025}$ (Using LP3)	28.49	26.02	25.46
$\Delta_{\varepsilon mu}$ (Using LP3)	44.64	55.50	43.36

The yield and ultimate curvatures and displacements were calculated based on equations provided by Paulay and Priestly [15]. The prediction calculations revealed that the wall's displacement response was affected by the plastic hinge length and the ultimate masonry compressive strain. The theoretical prediction of the response of the walls is compared with the experimentally measured response in the following subsections.

5.4 Results and Discussion

5.4.1 Force-displacement relationship and failure mode

The tested walls were dominated by a flexural failure mode, which was characterized by buckling of the vertical reinforcement rebar, horizontal cracks and crushing of the grouted core at the wall toes. The force-deformation relationship for the three tested walls is shown in Figure 5.1 (a to c). The first yield displacement (Δ_y) was defined as the displacement corresponding to the yielding of the outermost vertical reinforcement. The three tested walls had a hardening response. The force values in Figure 5.1(a to c) were corrected to account for the horizontal force component in the vertical actuators. Due to this correction, there was a small difference between the force-displacement relationship and the applied moment-displacement relationship. For clarity, the moment-displacement relationship was omitted from Figure 5.1(a to c). The wall's lateral displacement was reported at the first-floor level and at the top of the tested wall. For the tested walls shown in Figure 6, the cracks are localized at the first floor level, and fewer cracks are extended to the second floor.

The effects of changing the boundary element length and vertical reinforcement ratio on the response of the tested walls are shown in Figure 5.1 (d). Changing the boundary element length had almost no effect on the lateral resistance of the wall. The wall W5-$C_{L_b,VRFT}^{290,8}$ with a longer boundary element has a ductility ratio of 14 compared to 13 for the wall with a shorter boundary element, wall W4-$C_{L_b,VRFT}^{190,8}$. This increase in ductility can be explained by the increase in the ultimate crushing strain in the wall built with longer boundary elements. This increase was due to the vertical reinforcement and confinement hoop detailing in the boundary element. In the longer boundary elements, every steel rebar was tied with a confinement hoop compared to the shorter boundary elements, where only four of eight bars were tied with a confinement hoop. Tying every vertical steel rebar has the effect of increasing the strength and ductility of the boundary elements [88]. Increasing the ultimate crushing strain reduces the compression zone depth to the wall length ratio ($\frac{c}{l}$), which results in a more ductile section. The test results of walls W5-$C_{L_b,VRFT}^{290,8}$ and W6-$C_{L_b,VRFT}^{290,6}$ showed that increasing the vertical reinforcement increased the lateral capacity of the wall. The effect of increasing the vertical reinforcement on the ductility is discussed in the ductility section of this chapter.

79

With increasing lateral load, vertical splitting cracks appeared in the boundary element, and spalling occurred and uncovered the intact grouted core. Increasing the lateral displacement led to crushing in the toe zone of the confined core and buckling of the vertical steel bars in the boundary elements. The force-deformation relationship considers the horizontal component of the vertical actuators. In general, the tested walls had high deformation capacity, which can be represented by high displacement ductility and a large drift ratio. In addition, the tested walls had a large energy dissipation capacity, which can be represented by the large and wide hysteresis loops. The tested walls were able to maintain their lateral capacity under large inelastic deformation.

For W4-$C_{L_b,VRFT}^{190,8}$, the yield lateral loads, Q_y, were 56.6 and 54.3 kN, whereas the corresponding first yield displacements were 5.7 mm and 5.5 mm, in the push and pull directions, respectively. The average first yield displacement was taken as 5.6 mm, corresponding to 0.23% drift at the top of the wall, and it was used as the reference displacement for the next loading cycles. The ultimate lateral loads measured, Q_u, were 74.50 and 74 kN in the push and pull directions, respectively, corresponding to a displacement of 66 mm (2.8% drift at the top of the wall). The wall reached a lateral load of 70 kN (95% of the ultimate lateral load) at $6\Delta_y$ in the push direction and at $8\Delta_y$ in the pull direction, then it kept slightly hardening until $12\Delta_y$ when it reached the measured ultimate lateral load.

Spalling of the masonry face shell of the boundary elements in the push direction was observed at $7\Delta_y$. It was initiated by a vertical crack that was observed at the grouted core and masonry face shell interface. Face shell spalling extended to the third course in the push direction at $10\Delta_y$ and to the second course in the pull direction at $11\Delta_y$. Buckling of the vertical reinforcement in the boundary elements and grout core crushing occurred in the push direction at $12\Delta_y$ without noticeable strength degradation, as shown in Figure 5.3(a). The first reinforcement rebar rupture occurred during the first cycle of the $13\Delta_y$, which led to rapid strength degradation, upon which the test was terminated in the second push of $13\Delta_y$. Figure 5.2(a) shows the observed cracks of W4-$C_{L_b,VRFT}^{190,8}$.

For W5-$C_{L_b,VRFT}^{290,8}$, the lateral yield loads, Q_y, were 56.4 and 54.8 kN in the push and pull directions, respectively. The corresponding displacements for the lateral load at yield were 5.4 and 6.6 mm. The average first yield displacement was 6.0 mm, which corresponded to 0.25% of

the wall drift at the top of the wall and was used for the next cycles as a displacement increment factor. The ultimate lateral loads, Q_u, were 77.9 and 74.9 kN in the push and pull directions, respectively. The displacement corresponding to Q_u was 66 mm (2.77% drift at the top of the wall). At $6\Delta_y$ in the push direction and $7\Delta_y$ in the pull direction, the wall reached an average lateral load of 72 kN (95% of the ultimate lateral load) and then continued to harden slightly until $11\Delta_y$, when it reached the measured ultimate lateral load. The spalling of the masonry face shell on the side of the boundary element in the push direction was observed at $9\Delta_y$, as shown in Figure 5.3 (b). The vertical cracks between the grouted core and the masonry face shell initiated face shell spalling. The spalling of the face shell extended to the third course at $11\Delta_y$. The failure occurred at the first push of $14\Delta_y$ when buckling of the vertical reinforcement and crushing of the grouted core took place. The first diagonal shear crack was observed in the second cycle of $6\Delta_y$ at the first floor level, and it continues to increase with increasing lateral displacement. It was also observed that the number of diagonal shear cracks was lower in wall $W5\text{-}C_{Lb,VRFT}^{290,8}$ compared to wall $W4\text{-}C_{Lb,VRFT}^{190,8}$. The cracks in wall $W5\text{-}C_{Lb,VRFT}^{290,8}$ are shown in Figure 5.2 (b).

For $W6\text{-}C_{Lb,VRFT}^{290,6}$, the lateral yield loads, Q_y, in the push and pull directions were 53.60 and 45.12 kN, respectively. The corresponding displacements for the lateral loads at yield were 5.9 and 4.8 mm. The significant difference in the yield lateral load and displacement between the push and pull directions was due to a grout cavity observed in the web area during testing of the wall. To prevent such cavities from forming in a wall, it is a good practice to use clean-out during construction. The average first yield displacement was 5.3 mm, equivalent to 0.22% drift at the top of the tested wall and used as the reference displacement for the next cycles.

The ultimate lateral loads, Q_u, were 67.76 and 66.34 kN in the push and pull directions, respectively. The displacement corresponding to Q_u was 69 mm (2.89% drift at the top of the wall). The wall reached an average lateral load of 64 kN (~95% of the ultimate lateral load) at the 5th cycle in the push direction and the 7th cycle in the pull direction. It then continued to harden slightly until the 13th cycle, when it reached the measured ultimate lateral load. The vertical cracks and crushing of the boundary element's face shell at the toe zone took place at $8\Delta_y$, as shown in Figure 5.3 (b). Vertical cracks in the boundary elements propagated until the 9th cycle at $10\Delta_y$. Boundary element face shell spalling started at the toe zones at $11\Delta_y$. At $14\Delta_y$,

buckling of the vertical reinforcement occurred at the 7th boundary element course, causing a drop in the wall lateral capacity. The cracks of wall $W6\text{-}C_{L_b,VRFT}^{290,6}$ are shown in Figure 5.2 (c).

Table 5.2 shows the comparison between the predicted and the experimentally measured response. For the predicted values, the maximum compressive strain used was 0.0025 as per CSA S304-14 [20] clause 16.8.6, and the equivalent rectangular masonry stress block was $0.85f'_m$ as per clause (10.2.6). The shown experimental values were the average of the push and pull directions, except for the yield strength value for $W6\text{-}C_{L_b,VRFT}^{290,6}$, where only the value of the push direction was used due to the cavity on the west side of the wall. For the predicted ultimate displacement values, the values were calculated using Equation 5-1 based on the ultimate compressive strain of 0.0025 and the plastic hinge length. The comparison indicated that the predictions underestimated the yield strength by 16% to 21% compared to the experimental values. In addition, the prediction underestimated the ultimate lateral resistance for the walls by 23% to 28% compared to the measured lateral resistance. The lateral strength predictions showed that CSA S304-14 [20] provisions provide an acceptable safety margin for the lateral strength design values of the walls. The equations underestimated the first yield displacements by 34% to 43% and the ultimate displacements by between 40% and 57%. For the ultimate lateral displacement, the significant prediction errors could be attributed to the difference in the compressive strain value used by the code and the strain determined experimentally and due to the length of the plastic hinge region.

Table 5.2: Experimental and predicted forces and displacements

Wall		Q_y (kN)	Q_u (kN)	Δ_y (mm)	Δ_u (mm)	μ_Δ
$W4\text{-}C_{L_b,VRFT}^{190,8}$	Experimental	55.46	74.32	5.57	72.41	13
	Predicted	46.79	54.36	3.7	43.46	10.7
	Relative error	16%	27%	34%	40%	
$W5\text{-}C_{L_b,VRFT}^{290,8}$	Experimental	56.60	76.45	6.00	84.00	14
	Predicted	44.62	55.41	3.42	35.82	9.84
	Relative error	21%	28%	43%	57%	
$W6\text{-}C_{L_b,VRFT}^{290,6}$	Experimental	53.60	67.05	5.36	75.04	14
	Predicted	44.58	51.76	3.43	35.17	9.59
	Relative error	17%	23%	36%	53%	

(a)

(b)

83

1st floor displacement (mm)

Top of the wall lateral displacement (mm)

$+Q_y$	53.60 kN
$-Q_y$	-45.12 kN
$+Q_u$	67.76 kN
$-Q_u$	-66.35 kN
$+\Delta_y$	+5.9 mm
$-\Delta_y$	-4.8 mm

L_b	190 mm
b_b	290 mm
L_{wall}	1725 mm
Hoops	D4@60 mm
B.E Vert. Reinf.	6#3
Web Vert. Reinf.	4#3

(c)

Top of wall drift (%)

Push

Pull

wall 4
wall 5
wall 6

Top of wall displacement (mm)
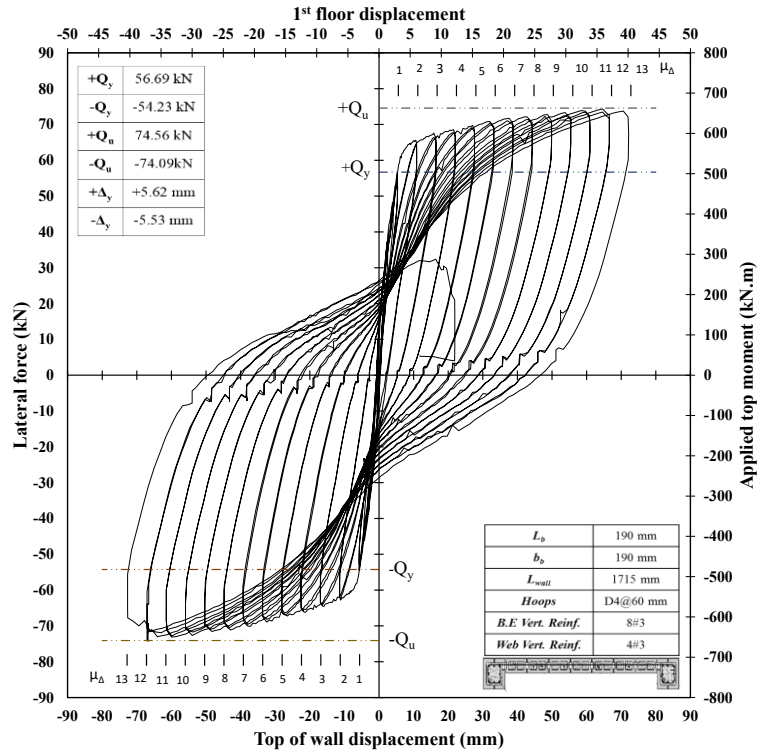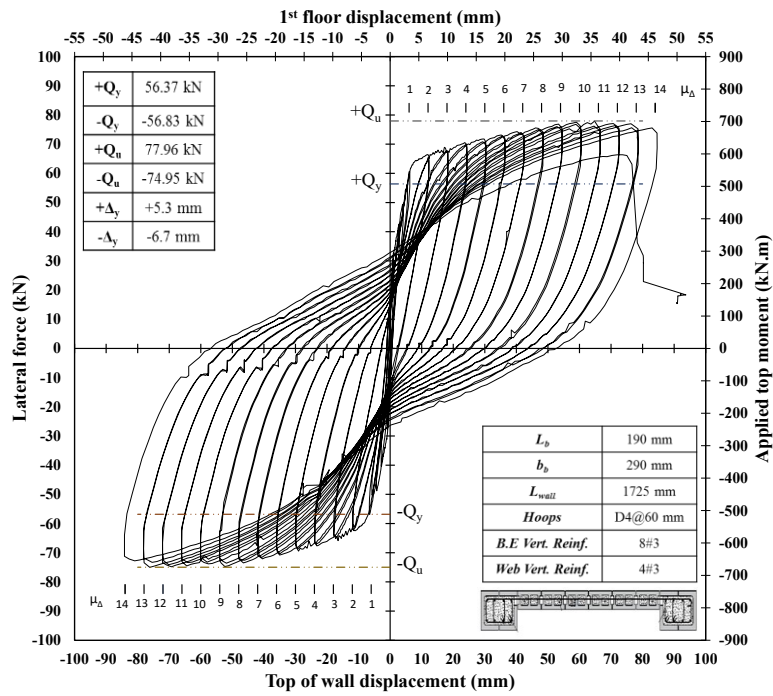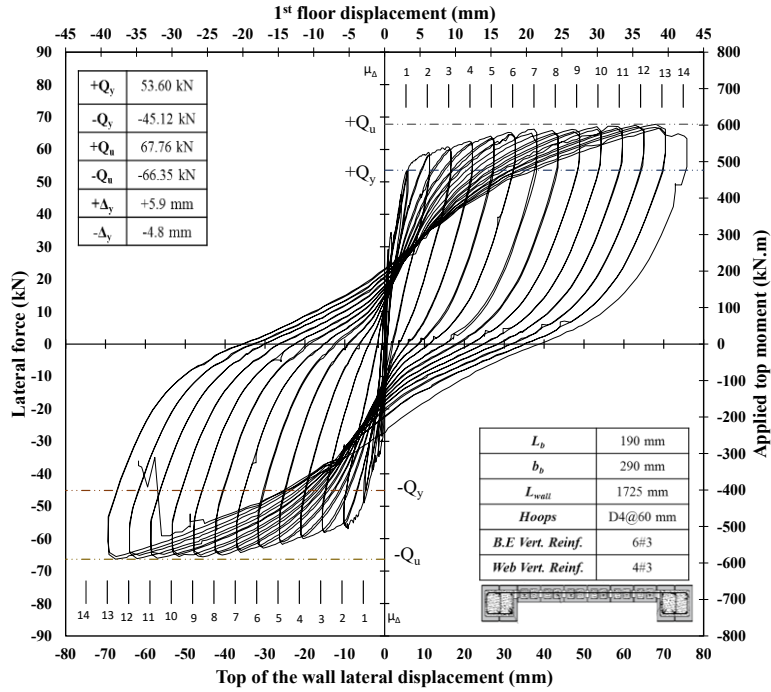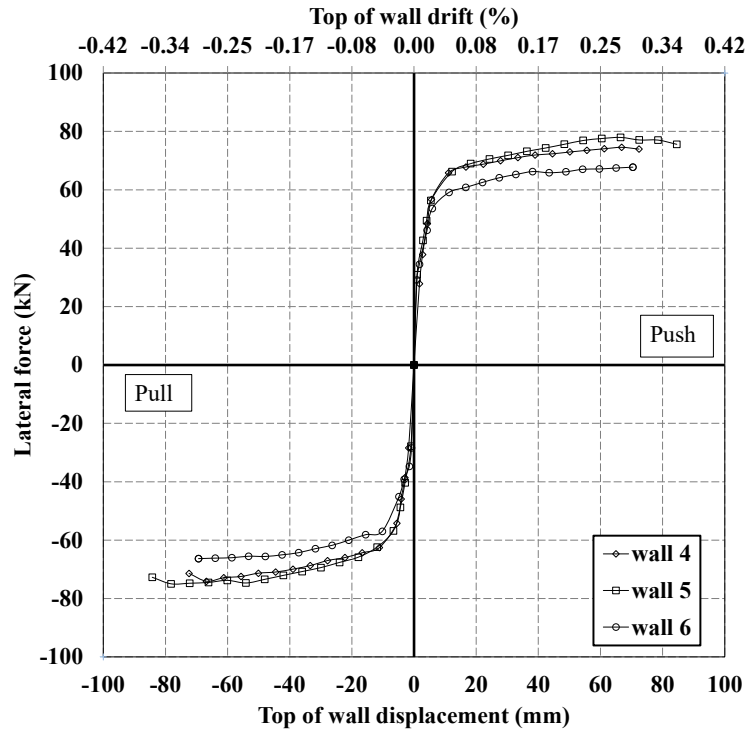
(d)

Figure 5.1: a) Force deformation relationship for W4-$C_{L_b,VRFT}^{190,8}$, b) Force deformation relationship for W5-$C_{L_b,VRFT}^{290,8}$, c) Force deformation relationship for W6-$C_{L_b,VRFT}^{290,6}$, d) Skeleton curve for the three tested walls.
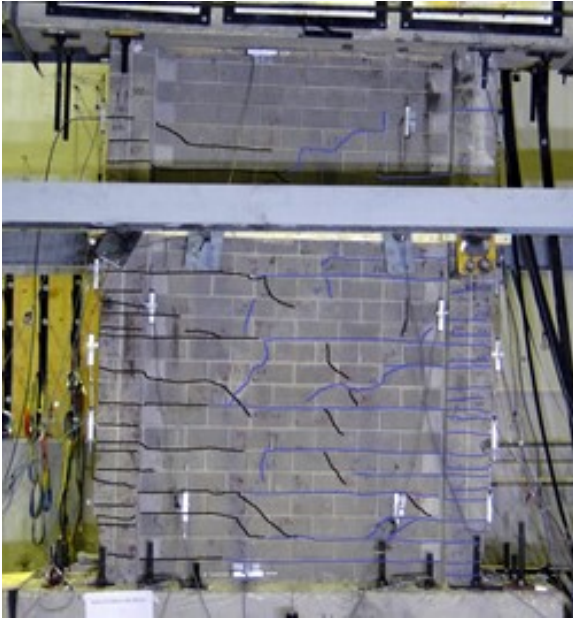
(a)

(b)
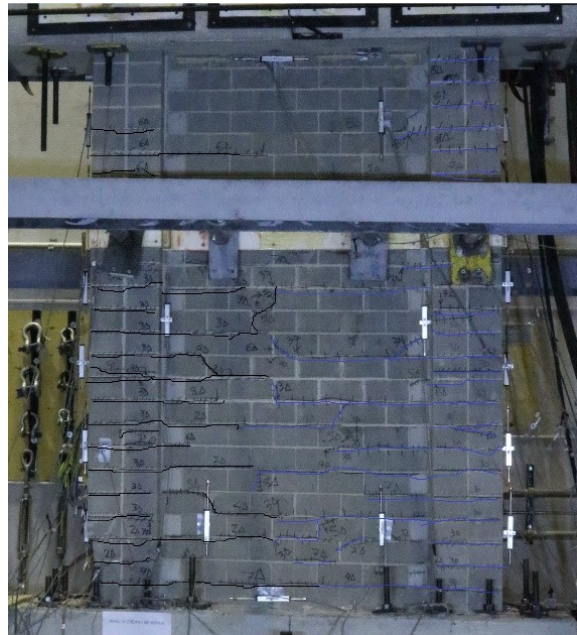
(c)

Figure 5.2: Wall crack pattern for a) W4-$C_{L_b,VRFT}^{190,8}$, b) W5-$C_{L_b,VRFT}^{290,8}$ and c) W6-$C_{L_b,VRFT}^{290,6}$

(a)	(b)	(c)
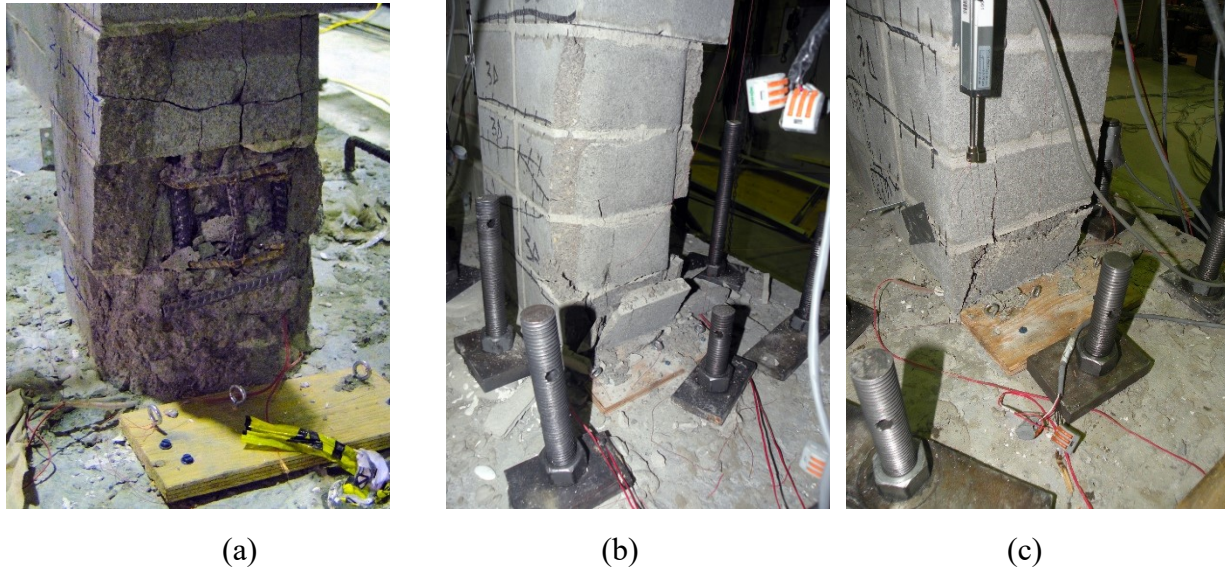
Figure 5.3: Cracks and reinforcement buckling at the toe zone a) W4-$C_{Lb,VRFT}^{190,8}$, b) W5-$C_{Lb,VRFT}^{290,8}$ and c) W6-$C_{Lb,VRFT}^{290,6}$

5.4.2   Displacement ductility

The displacement ductility ratio μ_Δ represents the ratio between the ultimate displacement (Δ_u) and the yield displacement (Δ_y) for an elastic-perfectly plastic system as described by Equation 5-5:

$$\mu_\Delta = \frac{\Delta_u}{\Delta_y} \hspace{4cm} \text{Equation 5-5}$$

The first yield displacement was taken as the displacement at the onset of yielding of the outermost vertical reinforcement bars at the end of the wall. Since no strength degradation was observed in the tested walls until the last cycle where the failure occurred, the ultimate displacement was considered the maximum displacement recorded for the walls. Table 5.3 shows the measured first yield displacement, the ultimate displacement, and the displacement ductility ratio for the tested RMSW without considering the idealized force-deformation relationship. From the test results of W4-$C_{Lb,VRFT}^{190,8}$ and W5-$C_{Lb,VRFT}^{290,8}$, it can be concluded that increasing the boundary element length by 50% increased the measured first yield displacement by 7.14% and the measured ultimate displacement by 15.38%. Additionally, it provided an enhanced displacement ductility ratio. The test results of W4-$C_{Lb,VRFT}^{190,8}$ and W6-$C_{Lb,VRFT}^{290,6}$ showed that the wall reached almost the same ultimate displacement and attained a higher displacement ductility

ratio when the masonry boundary element length was increased, and less vertical reinforcement was used. Comparing the responses of W5-$C_{L_b,VRFT}^{290,8}$, and W6-$C_{L_b,VRFT}^{290,6}$ showed that reducing the vertical reinforcement ratio in the boundary elements led to a reduction in the yield and ultimate displacement by 12.14%.

Reinforced masonry shear walls have different yield mechanisms due to their geometry, detailing and material properties [47]. According to the available literature, there are many approaches to idealize the force-displacement relationship of RMSW [89]. None of these methods is preferable [90]; however, the most commonly used method is the equal energy concept, in which the area under the actual force-deformation curve is equal to the area under the idealized curve. Figure 5.4 shows the idealized force-displacement relationship for the three tested walls. The difference between the idealized ultimate strength Q_{uid} and the measured ultimate strength Q_u was negligible (i.e., within 3%); thus, the two values were considered equal. The idealized force-displacement relationship was divided into elastic and plastic zones. The elastic zone corresponded to the area under the line that extended from the zero point to the idealized yield point (Q_u, Δ_{yid}) and passed through the measured yield point (Q_y, Δ_y). The plastic zone was the area under the plateau line that extended from the idealized yield point (Q_u, Δ_{yid}) to the ultimate displacement point (Q_u, Δ_u). The idealized wall response and idealized displacement ductility ($\mu_{\Delta id}$) are shown in Table 5.3.

Table 5.3: Experimental and idealized forces and displacements

Wall	Q_y (kN)	Q_u (kN)	Δ_y (mm)	Δ_u (mm)	μ_Δ	Q_{uid} (kN)	Δ_{yid} (mm)	Δ_{uid} (mm)	$\mu_{\Delta id}$
W4-$C_{L_b,VRFT}^{190,8}$	55.46	74.32	5.57	72.41	13	72.33	7.16	72.41	10
W5-$C_{L_b,VRFT}^{290,8}$	56.60	76.45	6.00	84.00	14	75.06	7.24	84.55	9.87
W6-$C_{L_b,VRFT}^{290,6}$	53.60	67.05	5.36	75.04	14	66.46	7.29	75.8	10
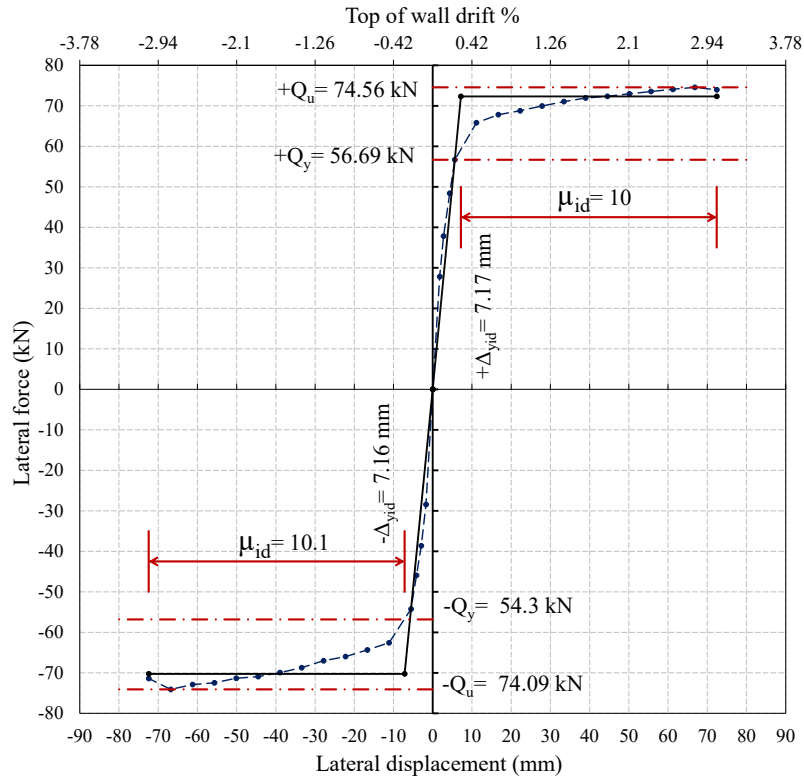
(a)
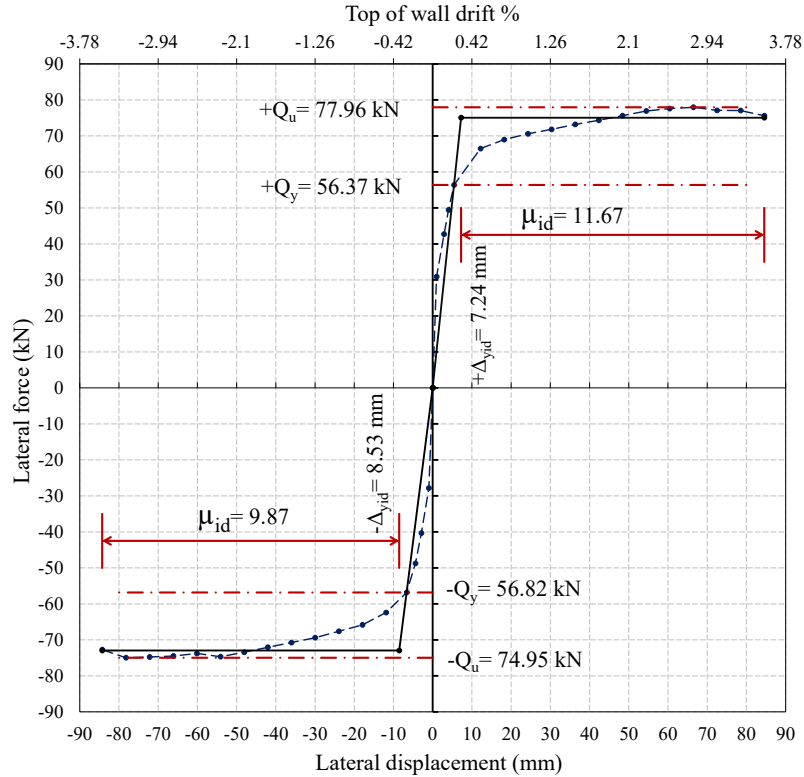
(b)
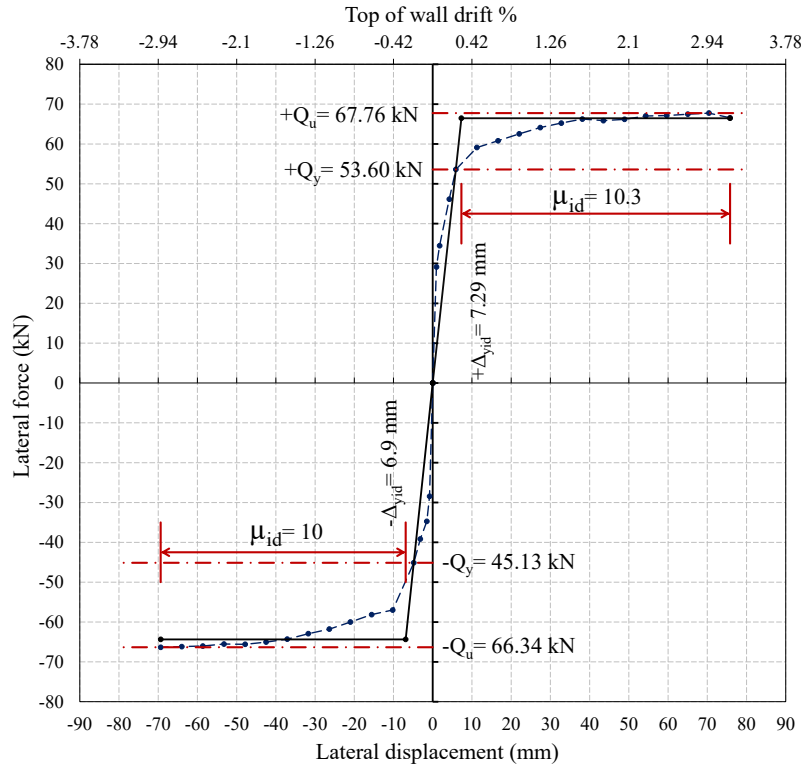
(c)

Figure 5.4: Idealized force displacement relationship for a) Wall 4, b) Wall 5and c) Wall 6

5.4.3   Ultimate compressive strain

The relationship between the average measured compressive strains at the ends of the walls and the normalized measured lateral force for the tested walls are shown in Figure 5.5(a to c). The vertical displacements at the wall ends were measured at heights of 340 mm, 680 mm, and 1020 mm from the top of the footings of the walls. The discontinuity in the measurements was due to face shell spalling and the loss of the brackets that held the potentiometers. The average measured ultimate masonry compressive strain for the three tested walls was 10×10^{-3} mm/mm which was four times the design value recommended by CSA S304-14 [20], i.e. 2.5×10^{-3} mm/mm.

Figure 5.5(d) shows a comparison between the measured axial compressive strains in the three walls averaged over 340 mm height (2.8% of the total effective height of the wall) at different ductility ratios. The comparison between W4-$C^{190,8}_{L_b,VRFT}$ and W5-$C^{290,8}_{L_b,VRFT}$ shows that increasing the aspect ratio of the MBEs and the configuration of the transverse reinforcement slightly increased the measured compressive strains in W5-$C^{290,8}_{L_b,VRFT}$. This can be attributed to the

89

increase in the confinement reinforcement ratio in the boundary elements of $W5\text{-}C_{L_b,VRFT}^{290,8}$. These results support the findings reported by Welt et al. [88], which showed that the contribution of changing the aspect ratio of the BE had a negligible influence on the measured compressive strains. However, it was also reported that increasing the number of tied vertical steel bars in the transverse direction increased the measured compressive strains. Thus, the increased measured strains in $W5\text{-}C_{L_b,VRFT}^{290,8}$ were attributed to the enhancement of the confinement reinforcement configuration rather than the increase in the length of the MBEs. The comparison between $W5\text{-}C_{L_b,VRFT}^{290,8}$ and $W6\text{-}C_{L_b,VRFT}^{290,6}$ shows that increasing the vertical reinforcement in the boundary element increased the measured axial compressive strain.

(a)

(b)

90
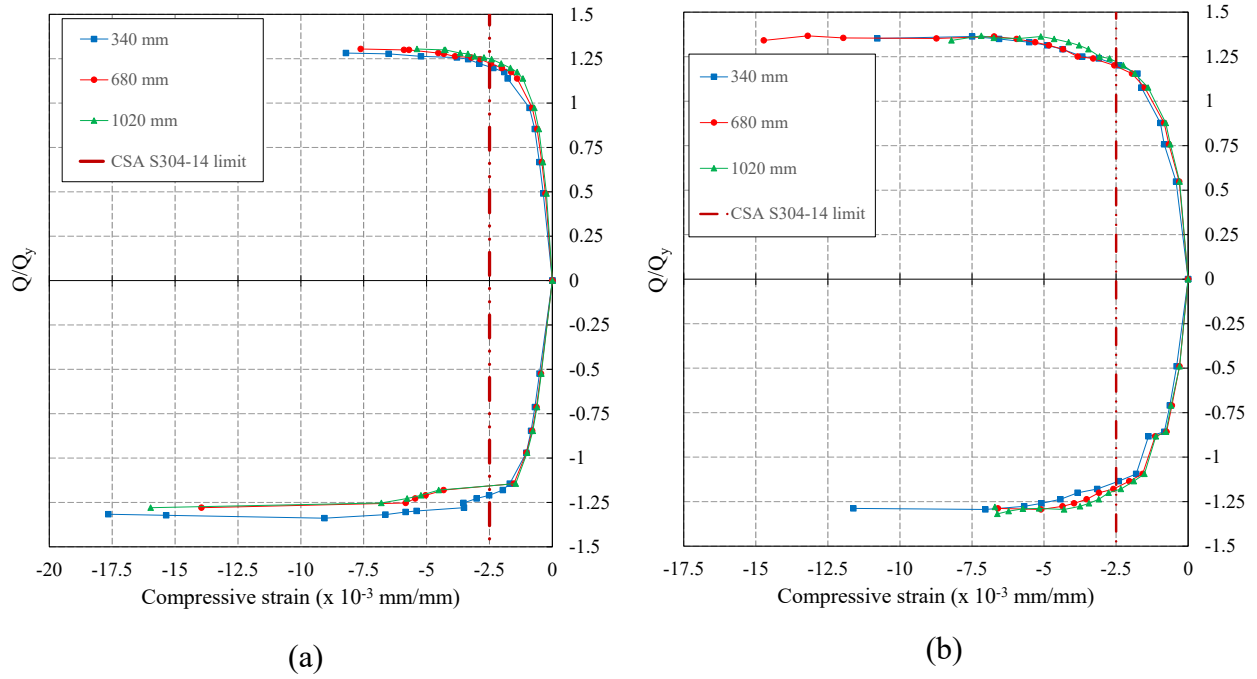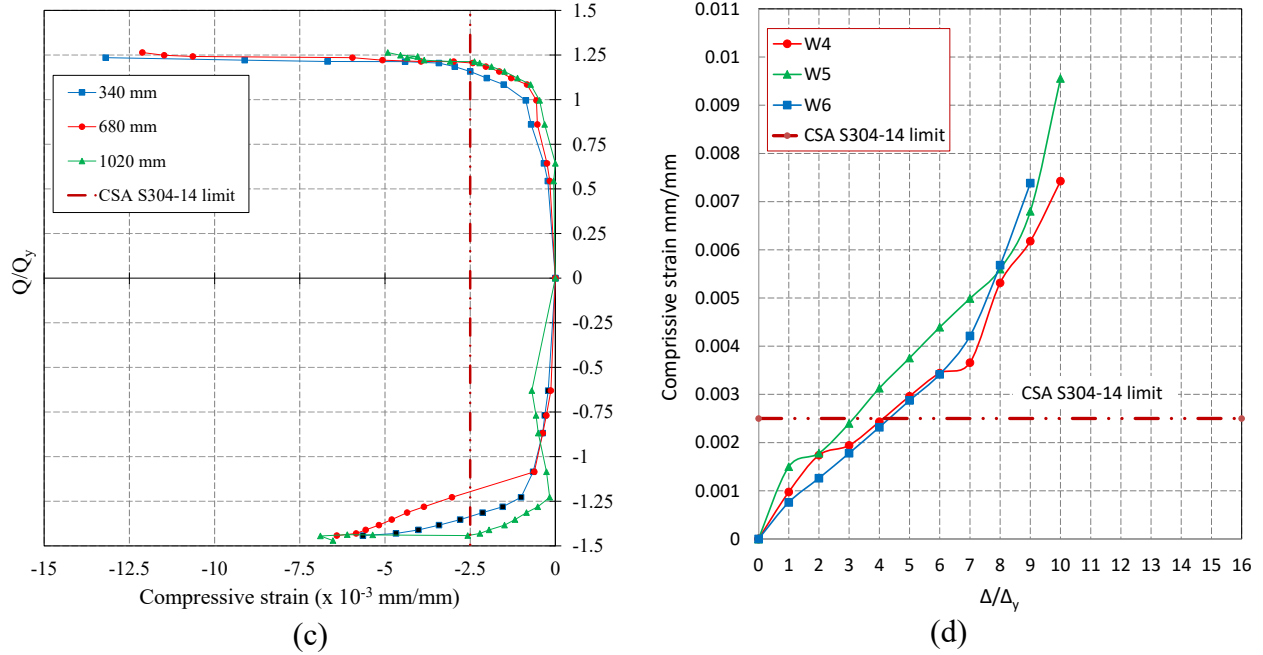
Figure 5.5: Measured compressive strain (a) W4-$C_{Lb,VRFT}^{190,8}$, (b) W5-$C_{Lb,VRFT}^{290,8}$, (c) W6-$C_{Lb,VRFT}^{290,6}$, and (d) Measured compressive strain at different ductility levels

5.4.4 Stiffness

Because low to moderate magnitude earthquakes frequently occur, there is a need for walls with adequate lateral stiffness to control deformations during these events. This helps prevent instability (local and global), alleviate the damage to non-structural elements, and ensure human safety. Calvi et al. [91] proposed using the secant stiffness in the context of displacement-based seismic design to improve the prediction of the response of a seismic force-resisting system to shear force. The effective lateral secant stiffness, k_e, is defined as the slope of the line from the zero point to the peak point of each cycle of the force-displacement relationship. The initial stiffness, k_i, was taken as the effective stiffness for the first cycle (0.25Δ) in the studied RMSW. The stiffness degradation was normalized by dividing the effective stiffness for each cycle by the initial stiffness (k_e/k_i). Figure 5.6 (a) shows the relationship between the effective stiffness and the top of the wall's lateral displacement for the three tested walls. All walls showed the same stiffness degradation pattern, with a considerable stiffness drop at low drift levels relative to the initial wall stiffness. The measured values of the initial stiffness (k_i) and stiffness at the yield strength (k_y), at the ultimate strength (k_{Qu}), at the ultimate displacement ($k_{\Delta u}$) and at different top of wall drifts (0.5%, 1.0%, 1.5% and 2.0%) are shown in Table 5.4. The measured initial

91

stiffness values for walls with larger boundary elements (W5-$C_{L_b,VRFT}^{290,8}$ and W6-$C_{L_b,VRFT}^{290,6}$) were approximately 100% higher than those for the wall with a smaller boundary element (W4-$C_{L_b,VRFT}^{190,8}$). This can be attributed to the increase in the moment of inertia and axial load to maintain the same axial stress level for walls with 190×290 mm BE. In addition, since the initial stiffness was taken as the effective stiffness for the first cycle (0.25Δ) and the wall with 190×190 mm BEs has three vertical bars at the outermost side of the wall compared to two vertical bars in 190×290 mm BEs walls. Wall with 190×190 mm BE underwent more displacement to measure 0.25 of the yield strain in the vertical bars. This increase in the displacement with a minor difference in the lateral loads could also contribute to the observed lower initial stiffness in walls with 190×190 mm BEs. The measured stiffness at the yield strength, ultimate strength and ultimate displacement points were almost the same for the three tested walls. The secant stiffness at first yield (k_y), which is a significant parameter in the design process of RMSW, was 64% for wall W4-$C_{L_b,VRFT}^{190,8}$ and 30% for walls W5-$C_{L_b,VRFT}^{290,8}$ and W6-$C_{L_b,VRFT}^{290,6}$. The three walls, regardless of their boundary element sizes and reinforcement ratios, had almost the same effective secant stiffness starting from the yield cycle until the failure of the walls. A comparison of walls W4-$C_{L_b,VRFT}^{190,8}$ and W5-$C_{L_b,VRFT}^{290,8}$ showed that the boundary element size influenced the initial stiffness of the tested walls. The comparison between walls W5-$C_{L_b,VRFT}^{290,8}$ and W6-$C_{L_b,VRFT}^{290,6}$ also showed that the vertical reinforcement ratio of the MBE significantly influenced the stiffness of the walls. Figure 5.6 (b) shows the variation in the normalized wall stiffness averaged in both loading directions with respect to multiples of the first yield displacement (Δ_{cycle}/Δ_y). The three tested walls showed the same stiffness degradation trend. However, wall W4-$C_{L_b,VRFT}^{190,8}$, with a smaller boundary element, had a higher normalized stiffness compared to the walls with larger boundary elements. This can be attributed to the lower initial stiffness of W4-$C_{L_b,VRFT}^{190,8}$.

Table 5.4: Experimentally measured stiffness

Wall	k_i (kN/mm)	k_y (kN/mm)	k_{Qu} (kN/mm)	$k_{\Delta u}$ (kN/mm)	0.5% (kN/mm)	1.0% (kN/mm)	1.5% (kN/mm)	2.0% (kN/mm)
W4-$C_{L_b,VRFT}^{190,8}$	15.56	9.91	1.2	1.02	5.8	3.05	1.99	1.2
W5-$C_{L_b,VRFT}^{290,8}$	32.1	9.8	1.14	0.89	5.33	2.87	2.00	1.25
W6-$C_{L_b,VRFT}^{290,6}$	31.04	9.53	1.11	0.87	5.16	2.81	1.82	1.33
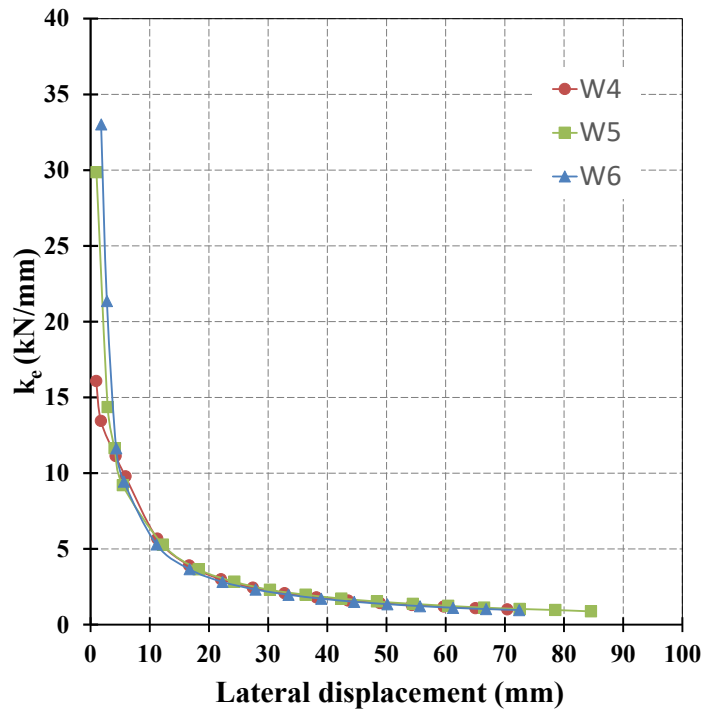
(a)
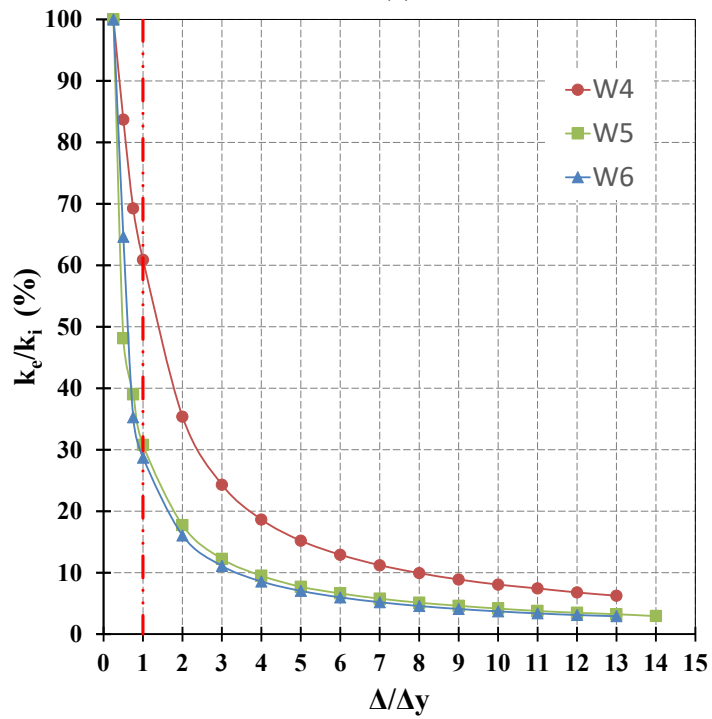
(b)

Figure 5.6: measured lateral stiffness (a) Relation between effective stiffness and the top of wall lateral displacement, and (b) Relation between normalized lateral stiffness and ductility level.

5.4.5 Curvature and curvature ductility

Figure 5.7(a to c) presents the curvature profiles of the tested walls at different displacement ductility levels. The reported curvature values were determined using the vertical deformations detected by LVDTs L1-L12 positioned on the ends of the tested walls. The results were averaged for each of the six gauge lengths shown in Figure 3.10 for the three tested walls. The curvature profiles are presented along the heights of the tested walls, which represents 16.4% of the effective wall height (h_{eff}). The curvature values at the start of the first yield in vertical reinforcement (φ_y), measured within the first 340 mm gauge length, are shown in Table 5.5. The measured yield curvature for wall W4-$C_{Lb,VRFT}^{190,8}$ (with the smaller boundary element) was less than the measured yield curvature for walls W5-$C_{Lb,VRFT}^{290,8}$ and W6-$C_{Lb,VRFT}^{290,6}$ (with the larger boundary element) by 26% and 18%, respectively. The difference in the measured yield curvature can be attributed to the difference in the walls' configuration and reinforcement arrangement, the difference in the applied axial load and the moment value at the yield point. The measured ultimate curvature, $\varphi_{\Delta u}$, for the three tested walls was taken at a ductility level 9 since the readings were subsequently discontinued due to face shell spalling. The measured ultimate curvature for wall W4-$C_{Lb,VRFT}^{190,8}$ (with the smaller boundary element) was less than the measured yield curvature in walls W5-$C_{Lb,VRFT}^{290,8}$ and W6-$C_{Lb,VRFT}^{290,6}$ (with the larger boundary element) by 9% and 7%, respectively. It is also can be noted that although W5-$C_{Lb,VRFT}^{290,8}$ has a higher $\varphi_{\Delta u}$ value when compared to W4-$C_{Lb,VRFT}^{190,8}$, W4-$C_{Lb,VRFT}^{190,8}$ has higher curvature ductility μ_{φ} due to its lower φ_y value Figure 5.7 (d) shows the relationship between the normalized total applied moment with respect to the yield moment and the average curvature measured over 340 mm from the top of the wall footing for the three tested walls. The comparison showed that the three walls, regardless of their configuration, had approximately the same normalized moment-curvature relationship until the yield point. However, notably, above the yield point, the increase in the BE size and vertical reinforcement resulted in an increase in the measured curvature. It also can be noted in Figure 5.7 (d) that W6-$C_{Lb,VRFT}^{290,6}$ experienced a minor reduction in the measured moment capacity at the 8th cycle due to concrete crushing. However, walls W4-$C_{Lb,VRFT}^{190,8}$ and W5-$C_{Lb,VRFT}^{290,8}$ did not experience this reduction due to the higher confinement ratio in boundary elements of these walls which increased the BE core capacity [92]. Due to the

testing frame limitations, the wall height was not enough to capture the full extent of the plasticity zone of the tested walls as shown in Figure 5.7 (a to c). Nevertheless, the equivalent plastic hinge length l_p can be obtained following the methodology proposed by Salim et.al. [92]. This methodology is based on a typical moment-curvature relationship where a reduction in the moment capacity is expected due to concrete crushing after reaching its maximum value in the ascending portion of the moment-curvature relationship. Therefore, W6-$C_{Lb,VRFT}^{290,6}$ results could be used to estimate l_p. Figure 5.8 (a) shows the moment-curvature relationship where M_1=806.1 kN.m is the maximum bending moment on the ascending part of the moment-curvature relationship, M_2=801.3 kN.m is the reduced moment due to concrete crushing and M_3=824.5 kN.m is the maximum moment capacity of the wall. In Figure 5.8 (b), the equivalent plastic hinge length, l_p, was obtained by intersecting M_1 line with a vertical line drawn from the minimum moment value M_2. The Figure 5.8 (b) shows that l_p equal to 1.6 m. The idealized W6-$C_{Lb,VRFT}^{290,6}$ curvature profile is shown in Figure 5.8 (c). When comparing the obtained l_p value with values estimated in section 2.4, it can be seen that the equation proposed by Mattock (1967) $0.5l_w + 0.05h_w$ is providing the most accurate estimate of plastic hinge height.

Table 5.5: Experimentally measured curvature

Wall	φ_y x10^{-5}(rad/mm)	$\varphi_{\Delta u}$* x10^{-5}(rad/mm)	μ_φ*	μ_Δ*
W4-$C_{Lb,VRFT}^{190,8}$	0.22	2.36	10.7	8.9
W5-$C_{Lb,VRFT}^{290,8}$	0.30	2.61	8.7	9
W6-$C_{Lb,VRFT}^{290,6}$	0.27	2.56	10.7	9.2

*Measured at the 9th cycle
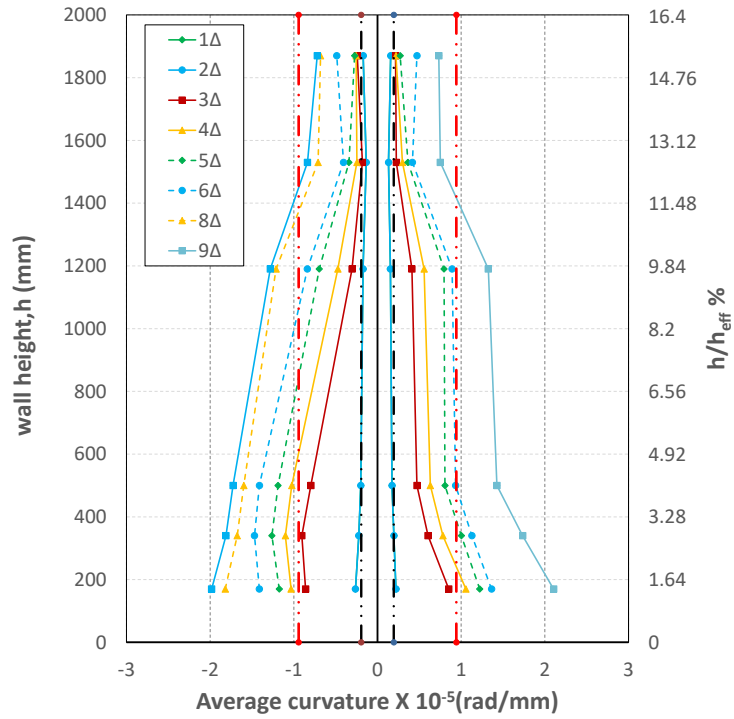
(a)
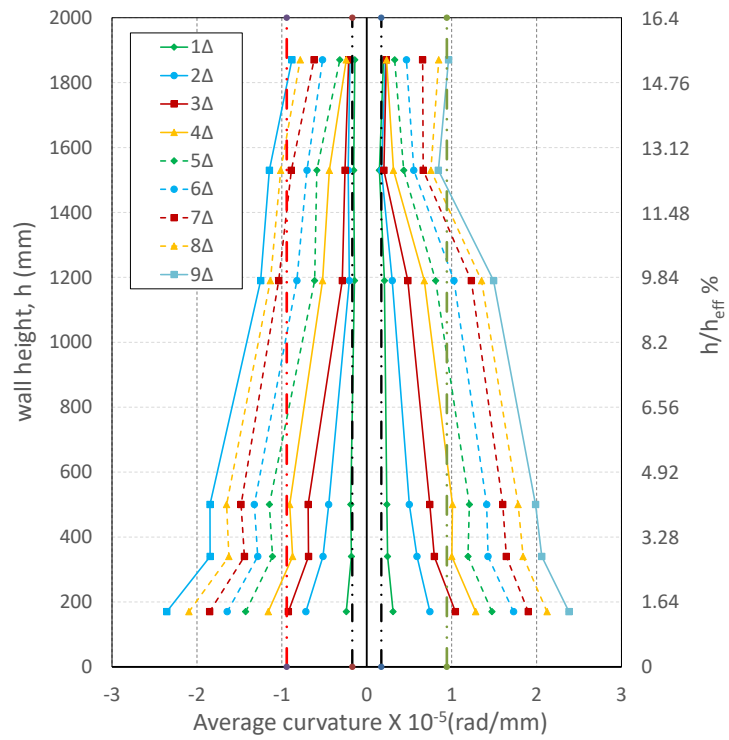
(b)
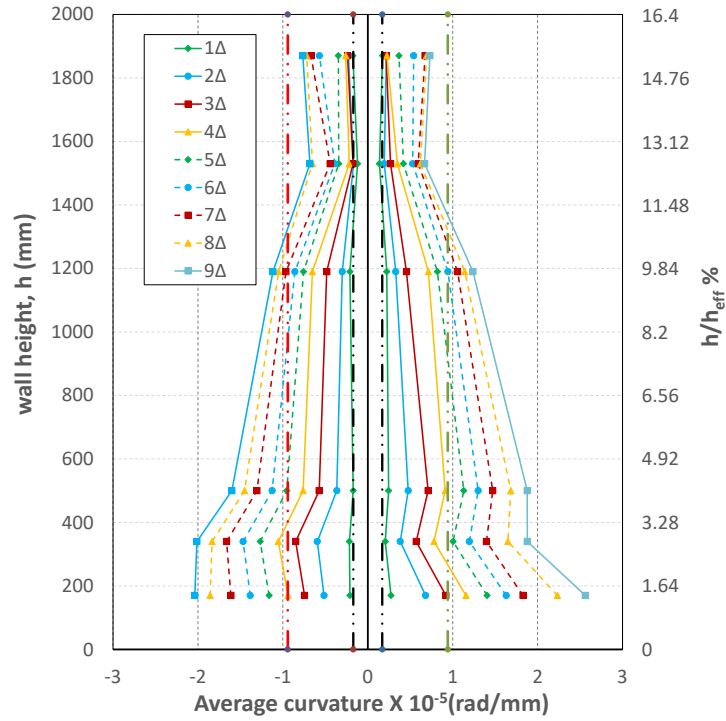
(c)
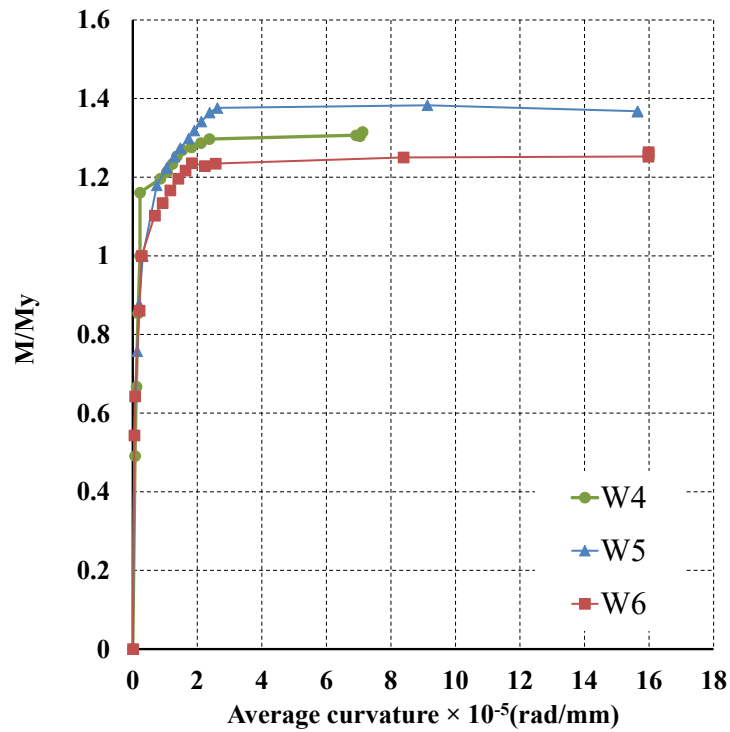
(d)

Figure 5.7: a) Curvature profile for W4-$C_{Lb,VRFT}^{190,8}$, b) Curvature profile for W5-$C_{Lb,VRFT}^{290,8}$, c) Curvature profile for W6-$C_{Lb,VRFT}^{290,6}$, d) normalized total applied moment with respect to the yield moment and the curvature for the three tested walls
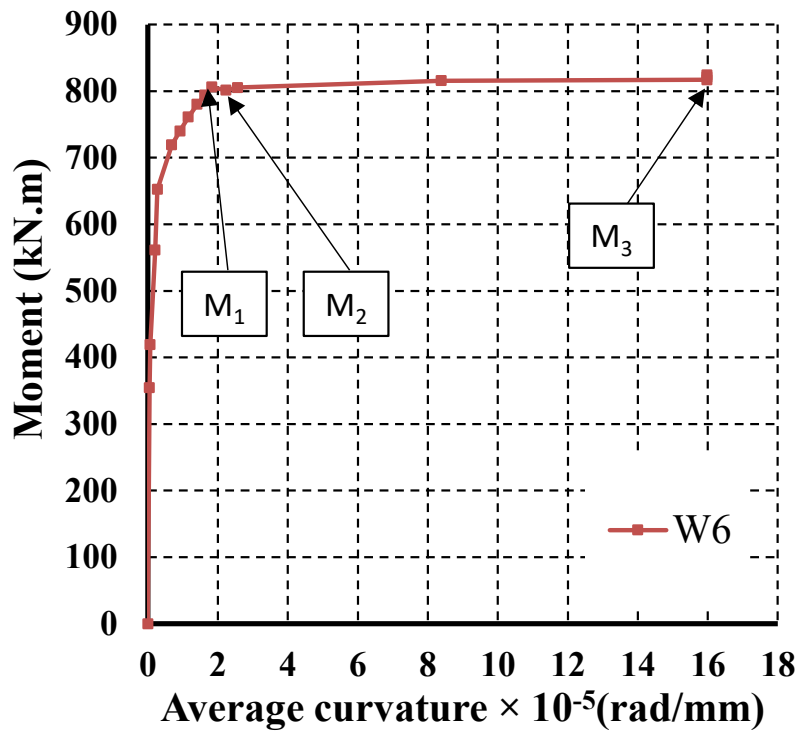
(a)
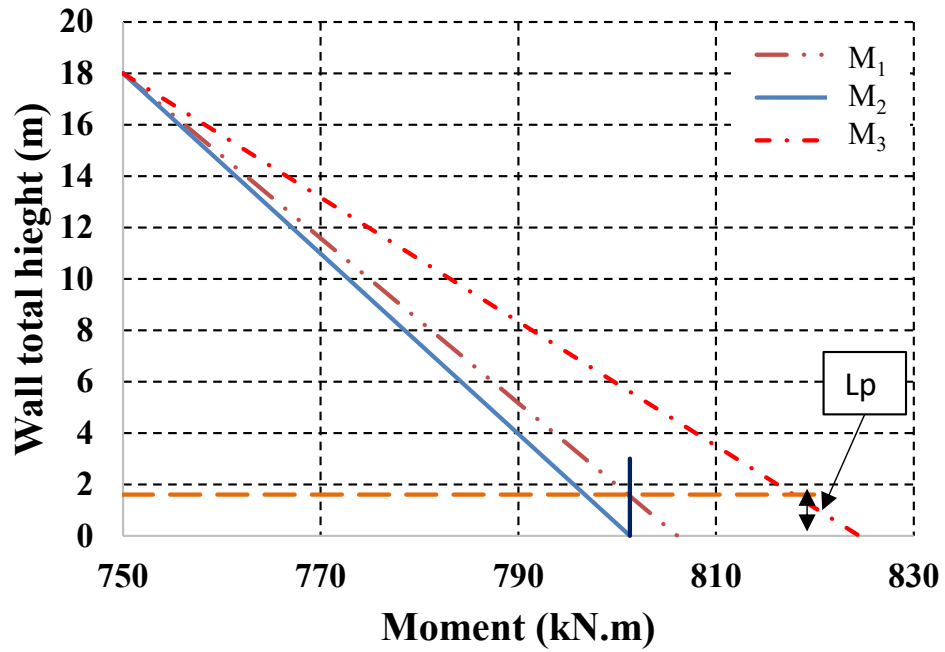
(b)
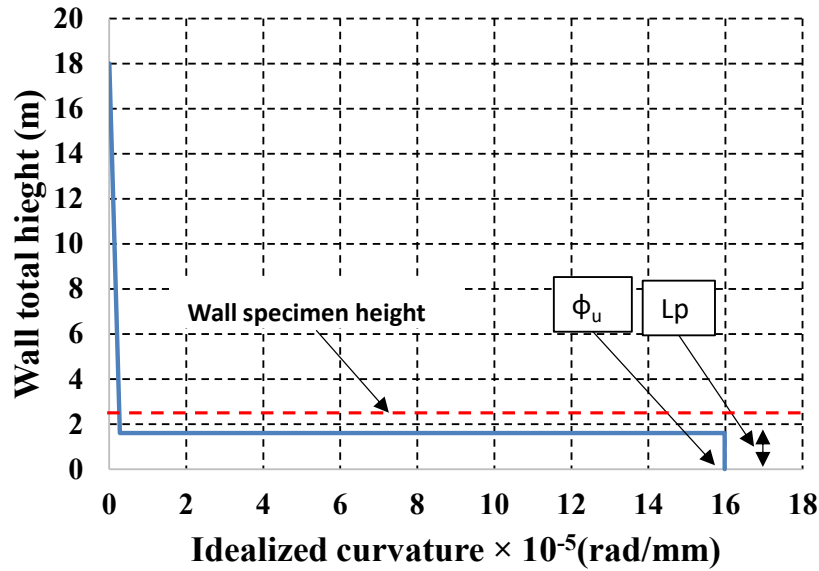
(c)

Figure 5.8: W6-$C_{Lb,VRFT}^{290,6}$ a) Moment-curvature curve b) Equivalent plastic hinge length
c) Idealized curvature profile.

5.4.1 Ductility modification factors

Reducing the design forces led to more inelastic deformations in the structure and, consequently, greater yielding of the vertical reinforcement and crushing of the masonry. This inelastic deformation can be accommodated by the structural system, ensuring that the wall will not experience a sudden strength degradation in the inelastic zone and provide an adequate ductile response. Moreover, displacement and damage in the structure must be well controlled [15]. The inelastic response provides two advantages: it increases the natural period of the structure, and it is cost-effective.

The National Building Code of Canada (NBCC) [21] recommends reducing the elastic force by the product of the ductility-related force modification factor, R_d, and the overstrength-related force modification factor, R_o. The elastic displacements are then multiplied by the product $R_d R_o$ to determine the inelastic displacements corresponding to the design lateral load. The R_d value of the ductile reinforced masonry walls is 3.0, and the R_o value is 1.5. The NBCC [21], in contrast, allocates an R_d value of 3.5 and an R_o value of 1.6 to reinforced concrete buildings built with ductile shear walls. ASCE 7-16 [93] assigns the same R value of 5.0 to both special reinforced concrete and special reinforced masonry shear wall structures. This section illustrates the

possibility of increasing the values of the ductility-related reduction factors for ductile RMSW to match the R_d value of ductile reinforced concrete walls.

Based on experimental observations in the published literature, two concepts were proposed to measure the ductility modification factor (D.M.F) [15][33]. The "equal displacement" principle is used for low-frequency systems up to 2 Hz, where the greatest displacement for an inelastic system is equal to or near the maximum displacement for an elastic system with the same initial stiffness. The D.M.F for an equal displacement system is equal to the system displacement ductility $R_d = \mu_\Delta$. In contrast, the second concept of the equal energy technique is valid for systems with frequencies ranging from 2 to 8 Hz. The energy under the load-displacement curve of the elastic system up to the maximum displacement is equivalent to that of the perfectly elastic plastic system when subjected to the same seismic excitation, which results in a D.M.F equal to $\sqrt{2\mu_\Delta - 1}$ [24].

For a structure with a natural period greater than the peak of the design response spectrum at 0.5 seconds, the inelastic system's maximum displacement is similar to that of an elastic system with the same stiffness as the inelastic system's initial elastic stiffness but unlimited strength [15]. For a twelve-story building, the estimated period is $0.05(h_b)^{3/4}$, where h_b is the building height, as specified by NBCC 2015 [21] is 0.75 second. Thus, In this study, the equal displacement approach was used to quantify the D.M.F as suggested by most of the force-based design codes [91].

Table 5.6 shows the calculated R_d and R_0 values, where Q_y is the measured yield strength, Q_{iu} is the idealized ultimate strength, Q_{du} is the design ultimate strength and Q_e is the ultimate strength for an equivalent elastic system. Figure 5.9 shows the calculated ultimate strength for an equivalent elastic system for the three tested walls. The overstrength factor, R_0, was calculated as the ratio between the idealized ultimate strength increased by 10% and the yield strength [35]. The ductility reduction factor was calculated as the ratio between the ultimate strength for an equivalent elastic system and the idealized ultimate strength. The minimum calculated ductility reduction factor for the tested walls was approximately 10, which highlights the strong potential for increasing the recommended R_d value by NBCC 2015 [21] for reinforced masonry ductile walls. More experimental data are needed to investigate the force reduction factor for RMSW on the component level. In addition, investigation on the system level by implementing FEMA P-695 [94] methodology is required.

100

Table 5.6: Strength and ductility modification factors

Wall	Q_y (kN)	Q_{iu} (kN)	Q_{du} (kN)	Q_e (kN)	R_d (Q_e/Q_{iu})	R_o ($1.1 \times Q_{iu}/Q_y$)	$R_d \times R_0$
W4-$C_{L_b,VRFT}^{190,8}$	55.46	72.33	54.36	729.65	10.08	1.43	14.46
W5-$C_{L_b,VRFT}^{290,8}$	56.60	75.06	55.41	876.2	11.67	1.46	17.02
W6-$C_{L_b,VRFT}^{290,6}$	53.60	66.46	51.76	690.27	10.38	1.36	14.16
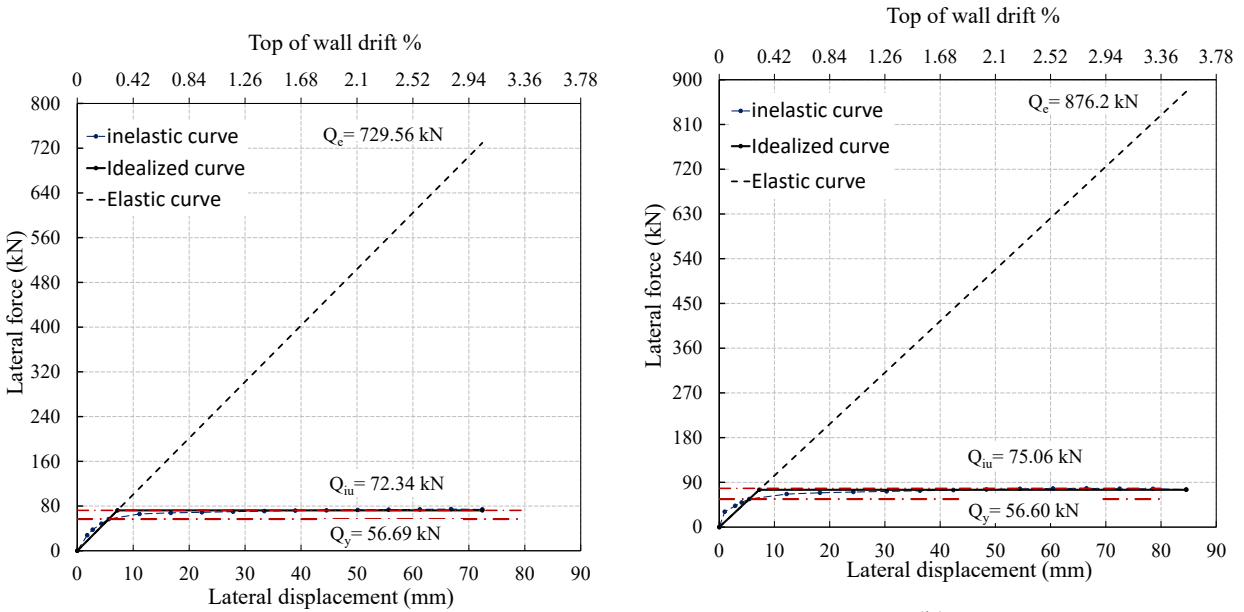
(a)

(b)
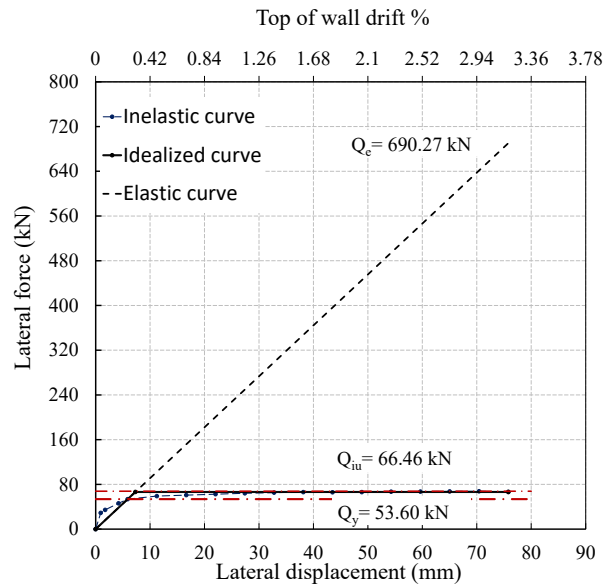
(c)

Figure 5.9: Idealized inelastic response VS elastic response for a) W4-$C_{L_b,VRFT}^{190,8}$, b) W5-$C_{L_b,VRFT}^{290,8}$ and c) W6-$C_{L_b,VRFT}^{290,6}$

101

5.4.2 Energy dissipation and damping

Energy dissipation is a critical factor in structural member seismic performance. Higher hysteretic damping is provided through energy dissipation, resulting in a smaller force to be resisted by the wall. The area enclosed by each hysteresis loop of the load-deformation relationship of the tested walls was used to compute the dissipated energy (E) at each ductility level. Figure 5.10 (a) shows the relationship between the dissipated energy (E) normalized with respect to the dissipated energy at the yield cycle (E_y) and the displacement ductility level. Because of the increased number of cycles, wall W5-$C_{Lb,VRFT}^{290,8}$ dispersed 32% more energy than wall W4-$C_{Lb,VRFT}^{190,8}$. However, the energy dissipated by each cycle in wall $W4 - C_{Lb,VRFT}^{190,8}$ was higher than that of wall W5-$C_{Lb,VRFT}^{290,8}$ due to the shift of the vertical reinforcement in W4-$C_{Lb,VRFT}^{190,8}$ towards the ends of the wall. These findings are consistent with Kapoi's [51] results, which revealed that walls with higher concentrated vertical reinforcement released 50% more energy. The comparison between walls W4-$C_{Lb,VRFT}^{190,8}$ and W5-$C_{Lb,VRFT}^{290,8}$ showed that, with the same vertical reinforcement area, walls with large boundary elements dissipated more energy in total due to the increased number of cycles. However, walls with smaller boundary elements dissipated more energy per cycle. Comparing walls W5-$C_{Lb,VRFT}^{290,8}$ and W6-$C_{Lb,VRFT}^{290,6}$ showed that reducing the vertical reinforcement ratio in the boundary elements led to the expected reduction in the amount of dissipated energy. This reduction was due to the reduction in the lateral strength of the wall. Another approach is to normalize the dissipated energy with respect to the input energy (E_{input}).

The input energy, E_{input}, at each displacement increment was estimated as the area under the skeleton curve of the first–hysteresis loop to that displacement level. Figure 5.10 (b) shows the relationship between the dissipated energy, normalized with respect to the input energy, and the displacement ductility level. The three tested walls had the capability of dissipating approximately the same input energy up to ductility level 2. The amount of energy dissipated by the three walls increased by 23% on average between ductility levels 1 and 2. After ductility level 2, the rate of increase in the dissipated energy decreased until ductility level 10, where the dissipated energy reached its maximum value until failure. By comparing W5-$C_{Lb,VRFT}^{290,8}$ and W6-$C_{Lb,VRFT}^{290,6}$ it can be observed that walls with a higher reinforcement ratio in the boundary

elements have more energy dissipation capability. The difference in the dissipated energy can be attributed to the higher vertical reinforcement ratio in the boundary elements in $W5\text{-}C_{L_b,VRFT}^{290,8}$. Concrete, as a brittle material, does not dissipate much energy with repeated cyclic loads. As a result, the energy dissipated by the reinforced concrete member is nearly equal to the energy dissipated by the member's flexural rebars [95]. Increasing the boundary element size had a negligible impact on the energy dissipation of the tested walls.

The relation between the damping ratio and the ductility level has been proven to be dependent on the hysteresis rules considered in the inelastic time history analysis shown in Figure 5.11 [96]. An elastic damping ratio of 5% may be assumed for concrete and masonry structures [24], [96]. Figure 5.12 shows the relation between the damping ratio and the ductility level for different hysteresis rules assuming the elastic damping of 5%. It can be seen from Figure 5.12 that the damping ratio is increasing with the increase of the ductility level. The increase in the damping ratio at a higher ductility level can be attributed to the increase in the dissipated energy.

For the tested walls, the damping ratio, ξ, was calculated using Equation 5-6, where E_{Diss} is the energy dissipated at a certain level of ductility, and E_{sto} is the elastic strain energy stored in an equivalent linear elastic system [97]:

$$\xi = \frac{1}{4\pi}\left(\frac{E_{Diss}}{E_{sto}}\right) \qquad\qquad \text{Equation 5-6}$$

As shown in Figure 5.10 (c), the hysteresis damping increased with increasing ductility level for the three walls. At ductility level 1, the walls had almost the same damping ratio of 6%. At higher ductility levels the damping ratio increased to exceed 20%. However, it is still recommended to keep the design damping value in the range of 2% to 5% [24] till more experimental data is available. With the increase in the ductility ratio, the damping ratio increased at a higher rate in wall $W4\text{-}C_{L_b,VRFT}^{190,8}$, which had a smaller boundary element.
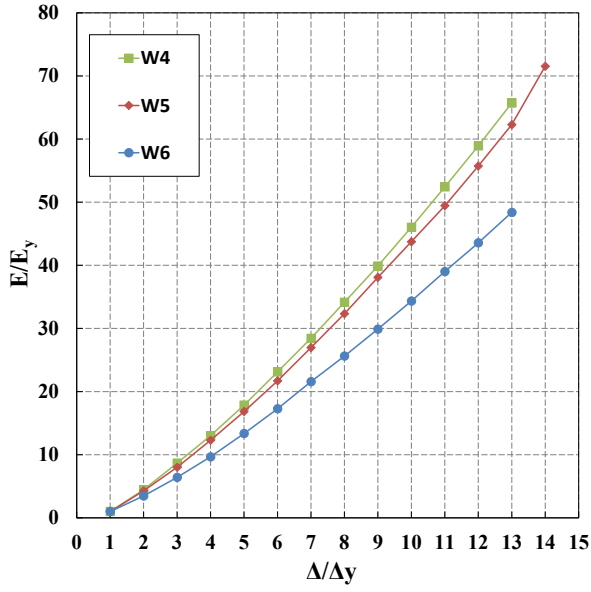
(a)
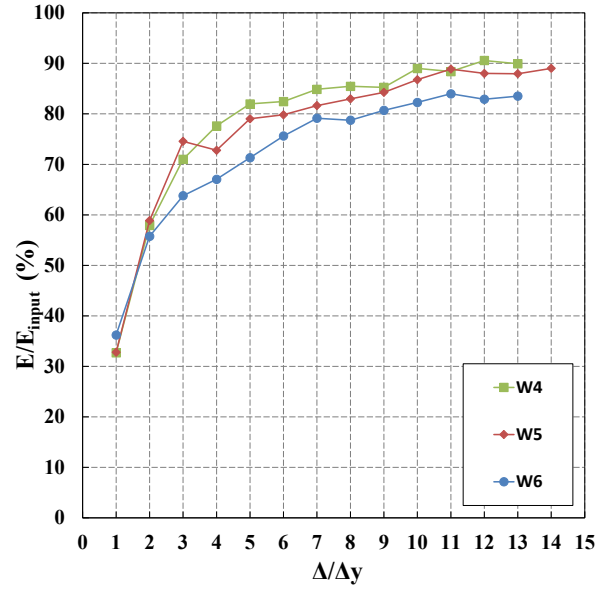
(b)
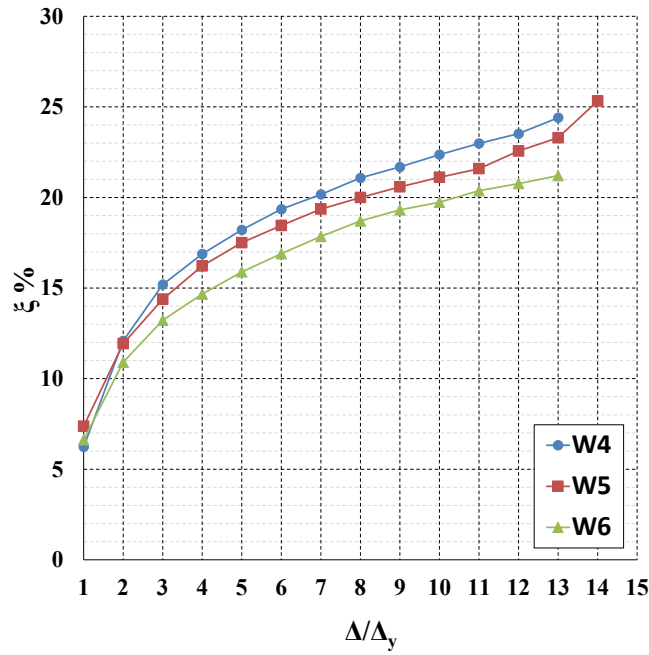
(c)

Figure 5.10: a) Dissipated energy normalize with respect to the dissipated energy at the yield cycle b) Normalized dissipated energy normalized with respect to the input energy and c) Damping ratio at different ductility level
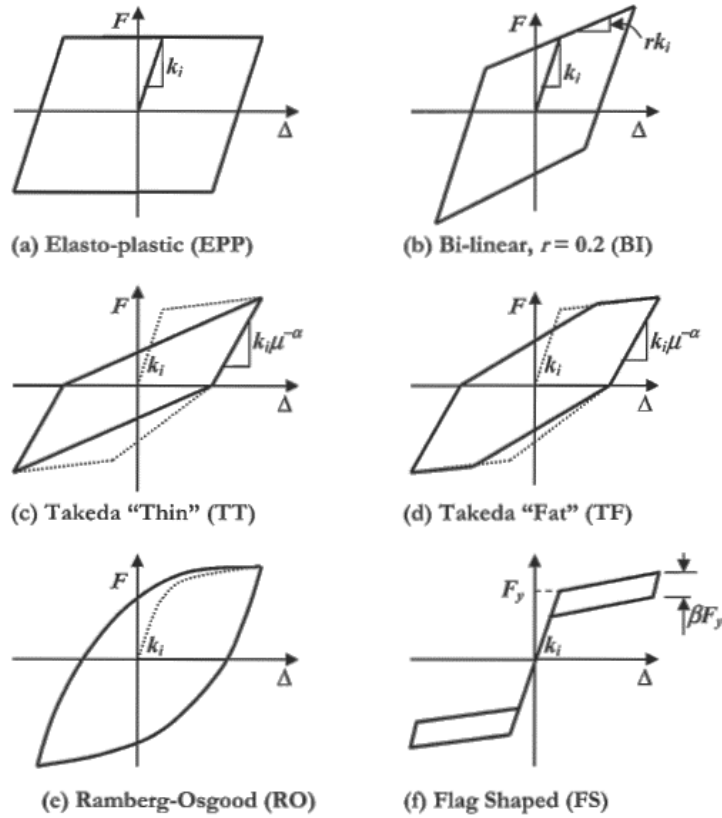
Figure 5.11:Hysteresis rules considered in inelastic time history analysis [96].
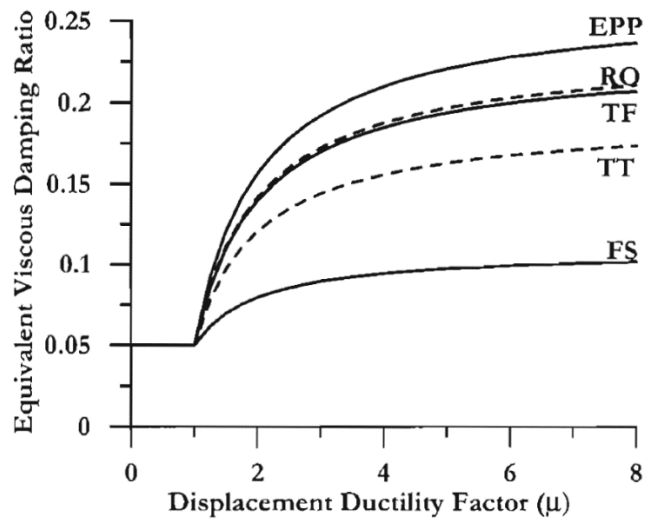
Figure 5.12: Design Equivalent Viscous Damping Ratios for 5% Elastic Damping [96].

5.5   Conclusions

Test results showed that the new C-shaped boundary element blocks utilized as MBE in RMSW allowed for the flexibility to control the lateral reinforcement spacing and increase the vertical reinforcement ratio and MBE size. The in-plane cyclic response of high-rise RMSW+BE was assessed in this study. The walls were built using half scale masonry units and tested to failure under sustained axial compressive loads and quasi-static reversed cyclic lateral loads and top moments. The specimens were slender walls that represented the plastic hinge of a wall in a 12-storey building. The effects of the change in the size and vertical reinforcement ratio of the MBE on the seismic response of the RMSW were established.

Additionally, the test results showed that the cracks in the tested walls were localized at the first floor level, and fewer cracks extended to the second floor. In general, walls were dominated by a flexural failure mode characterized by yielding of vertical reinforcement, horizontal cracks, and masonry toe crushing. Vertical splitting cracks appeared in the masonry boundary elements and spalling uncovered the intact grouted core when the applied loads increased. Larger lateral displacement led to toe crushing of the confined grout core and buckling/rupture of the vertical reinforcement bars in the MBE. Changing the size or the vertical reinforcement ratio of the MBE had minimal effect on the cracking pattern of the walls. All walls exhibited a consistent hysteretic response with large loops, indicating enhanced energy dissipation levels and damping capability. Furthermore, the walls with masonry fibres maintained high compressive strains that exceeded the value of 0.0025 recommended by CSA S304-14 [20]. The current CSA S304-14 [20] provisions predicted the lateral yield force and the ultimate lateral load with an acceptable safety margin for the proposed shear wall system. Increasing the BE size increased the initial stiffness of the wall. However, walls with smaller MBE had a larger normalized stiffness than walls with larger MBE. In conclusion, the vertical reinforcement ratio of the MBE had a minor influence on the stiffness of the tested walls.

Wall W4-$C_{L_b,VRFT}^{190,8}$ (with a small boundary element) showed a lower measured yield curvature than walls W5-$C_{L_b,VRFT}^{290,8}$ and W6-$C_{L_b,VRFT}^{290,6}$ (with a larger boundary element) by 26% and 18%, respectively. The measured ultimate curvature for W4-$C_{L_b,VRFT}^{190,8}$ (with a small boundary element) was less than the measured yield curvature in walls W5-$C_{L_b,VRFT}^{290,8}$ and -$C_{L_b,VRFT}^{290,6}$ (with a larger boundary element) by 9% and 7%, respectively. The comparison revealed that until the yield

point, the three walls had essentially the same normalized moment-curvature relationship, regardless of their configuration. Above the yielding point, increasing the boundary element size led to an increase in curvature.

It was also observed that the three tested walls dissipated the same input energy up to ductility level 2. Between ductility levels 1 and 2, the quantity of energy dissipated by the three walls increased by 23% on average. The rising rate in dissipated energy dropped after ductility level 2 until ductility level 10 when the dissipated energy reached its maximum value until failure. Walls with a higher boundary element reinforcement ratio dissipated up to 90% of the input energy. However, increasing the size of the BE had little effect on energy dissipation. The C-shaped components provided lateral strength as expected, as well as opportunities for the use of increased vertical and confining reinforcement and appropriate changes in the boundary element length. It is anticipated that employing C-shaped masonry units to construct MBE can significantly reduce the amount of time required to construct a wall by between 50% and 67% compared to walls constructed with normal stretcher units.

Notably, due to the testing frame limitations, the wall height was not sufficient to represent the full extent of the plasticity zone of the tested walls. Therefore, it is highly recommended that future studies consider using specimens with heights greater than the plastic hinge length calculated by Equation 5-1. Based on these test results, it is recommended that the ductility-related force reduction factor for ductile RMSW be increased from 3.0 (recommended by the current CSA S304-14). More experimental data are needed to investigate the force reduction factor for RMSW at the component level. In addition, an investigation at the system level by implementing FEMA P-695 [94] methodology is required.

In summary, the work presented in this chapter fulfils Objectives # 5, #6, and #7. The results confirm hypothesis #3, where increasing the boundary element length increased the measured ultimate crushing strain and ductility for walls with the same confinement reinforcement ratio (W4-$C_{L_b,VRFT}^{190,8}$ vs W5-$C_{L_b,VRFT}^{290,8}$). In addition, increasing the boundary element length maintained the same idealized ductility for walls with a lower confinement reinforcement ratio (W4-$C_{L_b,VRFT}^{190,8}$ vs W6-$C_{L_b,VRFT}^{290,6}$). For hypothesis # 4, reducing the vertical reinforcement ratio in BE for walls with different BE size increased the ductility. However, for walls with the same BE size, reducing the vertical reinforcement ratio reduced the ductility. The results are also confirming

hypothesis #5 that there is a potential to increase the ductility reduction factor for ductile RMSW recommended by NBCC 2015.

Chapter 6

Numerical Investigation of the Effect of Design Parameters on the Response Behaviour of Reinforced Masonry Shear Walls

6.1 Numerical modelling of the reinforcement masonry shear wall

To fulfil Objectives # 8 and # 9, a numerical model is developed and experimentally validated in this chapter to serve the following objectives. First, to investigate the effect of changing the confinement reinforcement ratio in reinforced masonry walls boundary elements on the seismic response behaviour of reinforcement masonry shear walls (to test Hypothesis # 2). Second, to establish the effect of the eccentricity in the boundary element on the accuracy of 2D model predictions. The effect of the used loading protocol (cyclic vs monotonic) on the wall curvature was also investigated in this chapter.

VecTor2 software, which was used in this study, is a nonlinear finite element analysis (NLFEA) program for two-dimensional reinforced concrete membrane structures [98]. VecTor3 program for the analysis of three-dimensional reinforced concrete solid structures.VecTor3 employs a three-dimensional smeared, rotating crack formulation developed based on two well-recognized analytical models for cracked reinforced concrete: the Modified Compression Field Theory and the Disturbed Stress Field Model [99]. VecTor software is implementing models developed for concrete material. The behaviour of fully grouted reinforced masonry shear walls is similar to the behaviour of reinforced concrete [36]. The cementitious material (concrete blocks, mortar and grout) properties were modelled as one material named "concrete" following the smeared modelling approach [100]. The model was validated against experimental results from three different experimental programs. A comparison between the results obtained from the 2D model and the 3D model is also presented in this chapter.

6.1.1 Finite-Element Model

Masonry walls consist of units such as stones, bricks, and blocks that are attached using mortar joints. Usually, these mortar joints have low tensile and shear bond strength, resulting in a weak interface between the units of the masonry. This causes the masonry walls to have anisotropic directional characteristics, depending on the orientation of the mortar joints relative to the applied pressures [101]. By having continuity in the stress flow, the existence of the grout

enhances the wall behaviour, making the behaviour of completely grout reinforced masonry (RM) walls comparable to reinforced concrete (RC) walls. There are two distinct primary approaches for modelling the composite masonry scheme, namely, the discrete crack approach and the smeared crack approach. In the discrete crack approach, the characteristics of each of the constituent components are modelled individually, namely, masonry units, mortar, grout, and reinforcing steel bars. On the other hand, the smeared crack approach considers the masonry materials' equivalent properties and is commonly used to study their nonlinear behaviour by modelling strengthened concrete structural components [102]. Since, as the effect of mortar joints is ignored, this strategy is appropriate for modelling hollow masonry units filled with grout [103].

Some of the currently suggested models are based on Vecchio and Collins (1986)'s Modified Compression-Field Theory MCFT. This theory deviates from the initial field theory of compression that considers the tensile stresses between cracks in the concrete (Vecchio 1986). The MCFT can be described as an analytical model for anticipating the reaction of reinforced concrete buildings that are subjected to in plane shear and normal stress [104]. In this theory, the conditions of equilibrium and compatibility within the shell element are considered in terms of average stresses and strains. The MCFT was developed by testing shell elements with uniform f_x and f_y axial stresses and a uniform v_{xy} shear stress (Figure 6.1). The deformed shape is presumed to have straight and parallel edges and can be described as a shear strain γ_{xy}, and ε_x and ε_y as the axial strain.
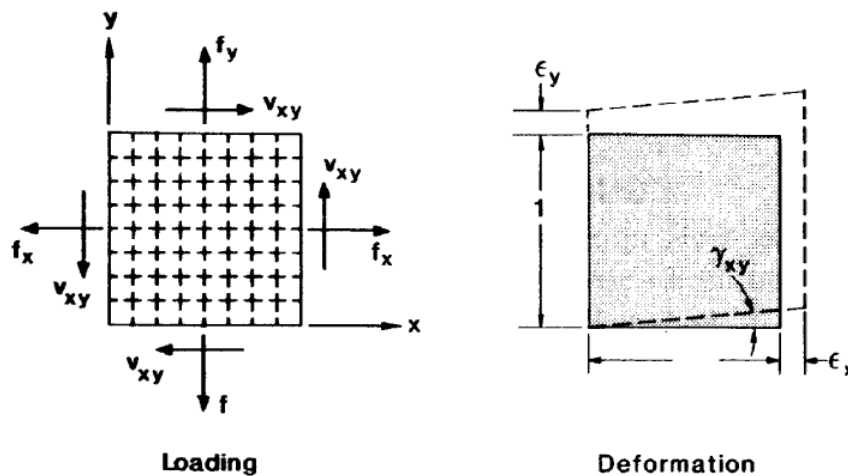
Figure 6.1: Membrane element (Vecchio 1986 [105]).

Based on the Modified Compression Field Theory (MCFT) and the Disturbed Stress Field Model [106], VecTor2 adopts a smeared, rotating-crack formulation for reinforced concrete. It offers many methods and models to capture the response of the simulated elements. Selecting these models will affect the numerical simulation results. To model panels of the reinforced masonry shear walls that were investigated in this research, the smeared method was chosen. The plane membrane element size of 100 mm x 100 mm was chosen based on research was undertaken by Minaie et al. [107] and Seif Eldin et al. [69], which showed that this mesh element size is practical and offers an acceptable level of precision for finite element modelling of masonry walls. Grouted masonry was modelled using four nodes rectangular plane elements with uniform thickness. Rectangular plan element is eight degree of freedom element (two degree of freedom for each node in the x and y direction). VecTor 2 has the capacity of 4000 elements. The flexural and shear reinforcement was smeared in the vertical and horizontal directions along the in-plane membrane element area with eight degrees of freedom, or rectangular element, as named in VecTor2 software. Moreover, this element size reflects the actual size of each in-plane cell for the normal half-scale concrete block dimensions considered in this research. In this model, three distinct plane membrane components have been described and used.

The number of load stages, determined by the load increase factor, can affect solution convergence efficiency. When the building is in deteriorated condition, many small load increments may be preferred to fewer large ones. Smaller load increments allow the solution to converge in fewer iterations before continuing. Given concrete's total softening response, poor convergence may overestimate its strength for imposed displacement and underestimate displacement for the applied load. After many trials, it was found that selecting the load step increment factor to be equal to the first cycle target displacement divided by 16 provided a good conversion.

The first element has a high compressive strength masonry with a large proportion of strengthening in the x and y directions and was assigned to the top loading beam and the wall footing to make sure it is stiff and uncracked while loading the walls. The second element, which represents the boundary elements, has the assigned compressive strength of the masonry material, and the vertical and horizontal reinforcement, as a percentage of their respective cross-sectional area. In addition, the second plane member has a confinement level that is defined as the ratio between the steel hoops volume and the grout bounded by two vertical hoops volume.

The third element was used to model the web area. It has the same percentage of the smeared vertical reinforcement in the y-direction as the vertical reinforcement and is distributed uniformly along the wall length (see Figure 6.2). In this strategy, the bond between the steel reinforcement and the masonry was assumed to be fully bonded, since the failure mechanism by de-bonding was not one of the types of failure observed in this investigation. In order to simulate the boundary conditions in the laboratory test, all the joints at the foundation base were restricted in the x and y directions. Nevertheless, all the other joints were not restricted in any direction.

6.1.2 Material Models

The behaviour of fully grouted RM walls under axial stress is comparable to that of RC walls. The stress-strain compression relationship for masonry can, therefore, be simulated using equations comparable to those for concrete [15]. The chosen pre-peak and post-peak compression base model used in this analysis is based on a non-linear relationship suggested by Hoshikuma et al. [108] in terms of the average compressive force f_m and the corresponding peak strain ε_p.

To consider the combined effects of the transverse cracking and tensile strain that causes compression softening in cracked concrete, the compression softening model 1992-B (e1/e0-Form) suggested by Vecchio [98] was used. A significant loss in stiffness, ultimate strength capacity, and ductility can result from this reduction. Vecchio 1992-B (e1/e0-Form) model calculates the reduction factor β_d to the peak compressive strength f_m with no change to the corresponding peak strain [109].

Adding confinement reinforcement in the boundary element has two effects on the wall behaviour. The first effect is increasing the concrete strength and strain corresponding to the peak stress by an enhancement factor β_1. Kupfer-Richart Model was adopted by VecTor2 to calculate the enhancement factor based on the relationship proposed by Kupfer et al. [110] and Richart et al. [111]. The second effect of adding confinement reinforcement is the buckling of vertical reinforcement. There are three models to be considered for reinforcing bar buckling. These are the Dhakal-Maekawa (DM), the Refined Dhakal-Maekawa model (RDM) [112], [113], and the Asatsu models. The DM and RDM models can only be utilised with ductile steel reinforcement modelled using Seckin or Menegotto-Pinto hysteretic models [98]. This occurs when the unsupported length to diameter ratio (L/D) of the reinforcing bars exceeds 5.0, and the

112

compressive reinforcement strain exceeds its yield strain in both models. As a result, both models require L/D input prior to the analysis for L/D ratios > 5.0 to account for rebar buckling. For L/D=0 and L/D=5, no rebar buckling effects are considered. The Asatsu model does not require L/D input. Akkaya et al. (2013) adapted Seckin and Menegotto-Pinto hysteretic models for ductile reinforcement with buckling effects utilising Dhakal and Maekawa (2002b) formulations, which are applicable to discrete modelling for reinforcement.

A quick decline in masonry tensile stresses occurs when the principal tensile stress is greater than the tensile strength of masonry. This results in the initiation of cracks in masonry walls. Increased deformations lead to larger cracks, which lowers bonding activity on the surface of the crack. 'Tension stiffening' is the term for this type of behaviour. The deterioration slope is influenced by the amount of reinforcement and the bonding mechanism since the tensile stresses are redistributed to the reinforcement [98]. Modified Bentz model [114] was chosen in this investigation because it provides a more accurate degradation branch response to lateral loads after multiple trials.

Many processes such as dowel action, strain softening, shear slip along crack surfaces and others have been considered in this finite element FE model, as shown in Figure 6.3.
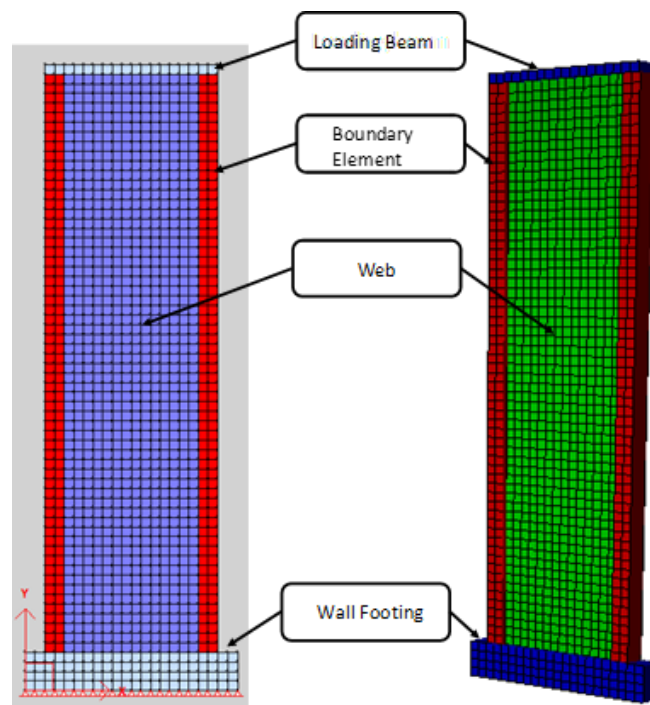
Figure 6.2: Finite element mesh for the studied RM walls.
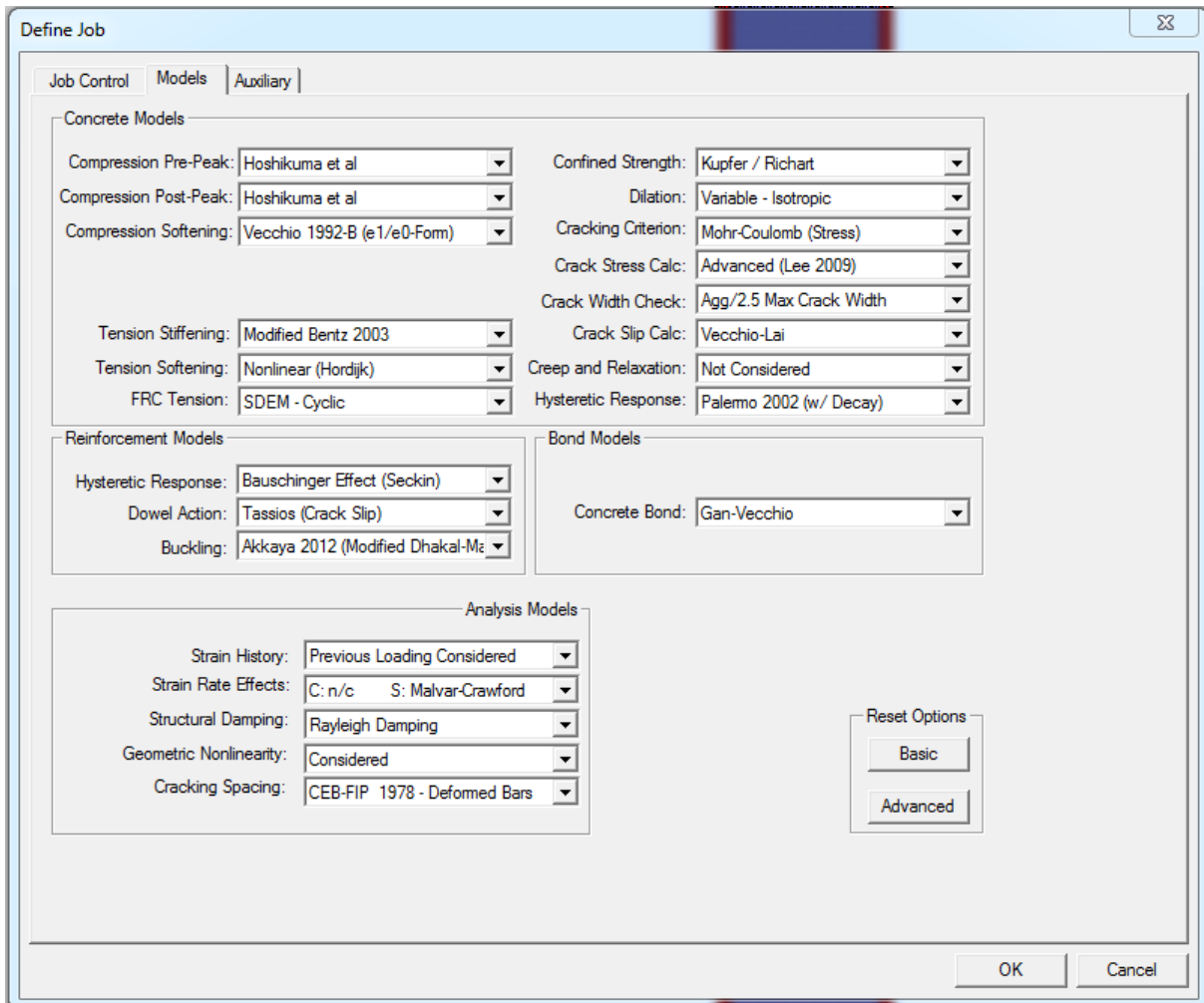
Figure 6.3: Materials and analysis models

6.1.3   Model validation

The model was calibrated and validated in two steps. The first step is to validate it against the behaviour of two walls that were reported in the literature; wall 4 tested by Banting et al. [9] and wall 3 tested by Shedid et al. [8]. Both walls were reinforced fully grouted masonry walls with boundary elements and they were three-storey height. Figure 6.4(a,b) shows that the predicted hysteretic responses are in good agreement with the experimental results reported in [2,51]. The suggested nonlinear model for RM shear walls predicts initial stiffness, yield strength, and ultimate strength. On average, the numerical predictions are within 10% of the experimentally measured values. In the second step, the model was validated against the experimental results reported by the author for $W4\text{-}C_{Lb,VRFT}^{190,8}$. The comparison between these results and the model predictions shows even better agreement, as shown in Figure 6.4(c). This shows that model

predictions are much closer to the experimental data when there is a complete knowledge of the test conditions and the material properties. It can also be seen that the model captures the performance of the RM structural wall with a wide range of aspect ratios (i.e. 2.21, 3.23 and 10.6). Figure 6.5 shows a comparison between the curvature profile for the tested specimen Wall 4 [83] and the outcome curvature profile from the numerical model. The comparison shows that the numerical model is capable of predicting the wall curvature with only a 9% error. It can also be seen that the model can capture well the yield curvature and the plastic hinge height. The deviation of the model predictions from the measured values happened only at curvatures $>$ 16×10^{-5} due to the failure of one of the potentiometers as a result of the face shell spalling. Figure 6.6 displays the strain profile measured at the base of the wall specimen over a length of 340 mm at drift levels of 1.0%, 1.5% and 2.0%. There is good agreement between the experimental results and the model predictions for drifts of 1% and 1.5%. At 2% drift, the max difference between the experimental measurements and the numarically predicted strains is 45% which can be attributed to the face shell spalling. In conclusion, the numerical model is shown to be capable of capturing the cyclic behaviour, curvature profile and the strain distribution along the wall length.

(a)

115
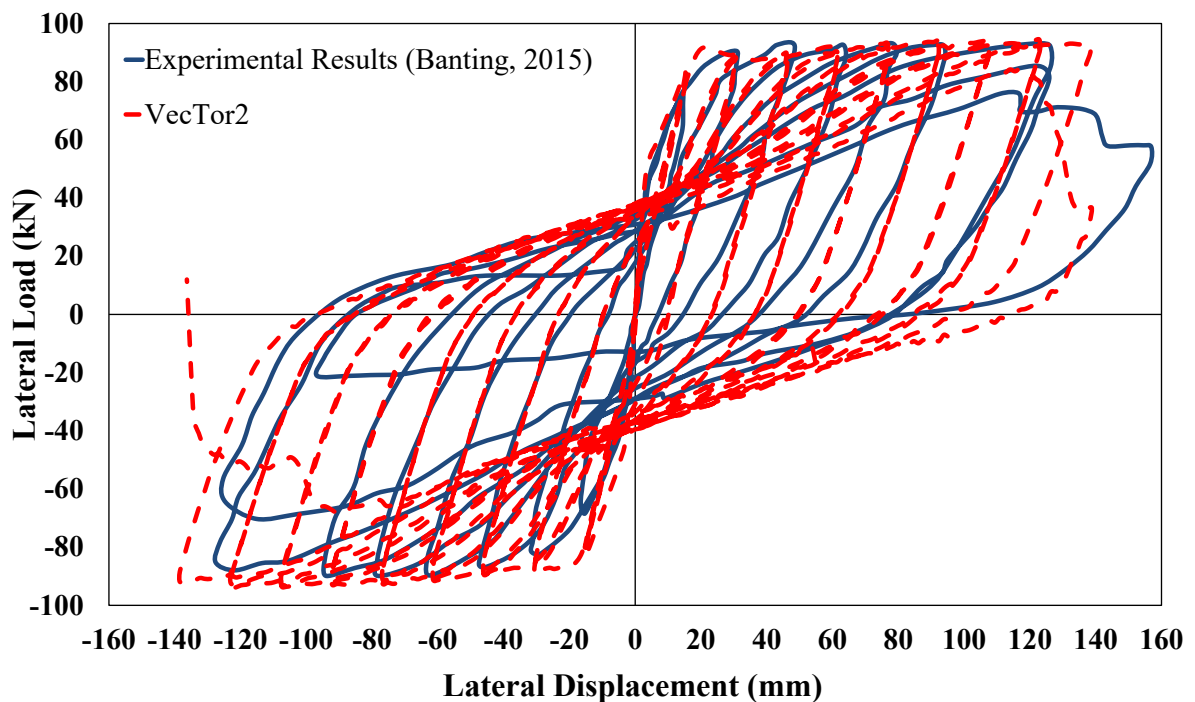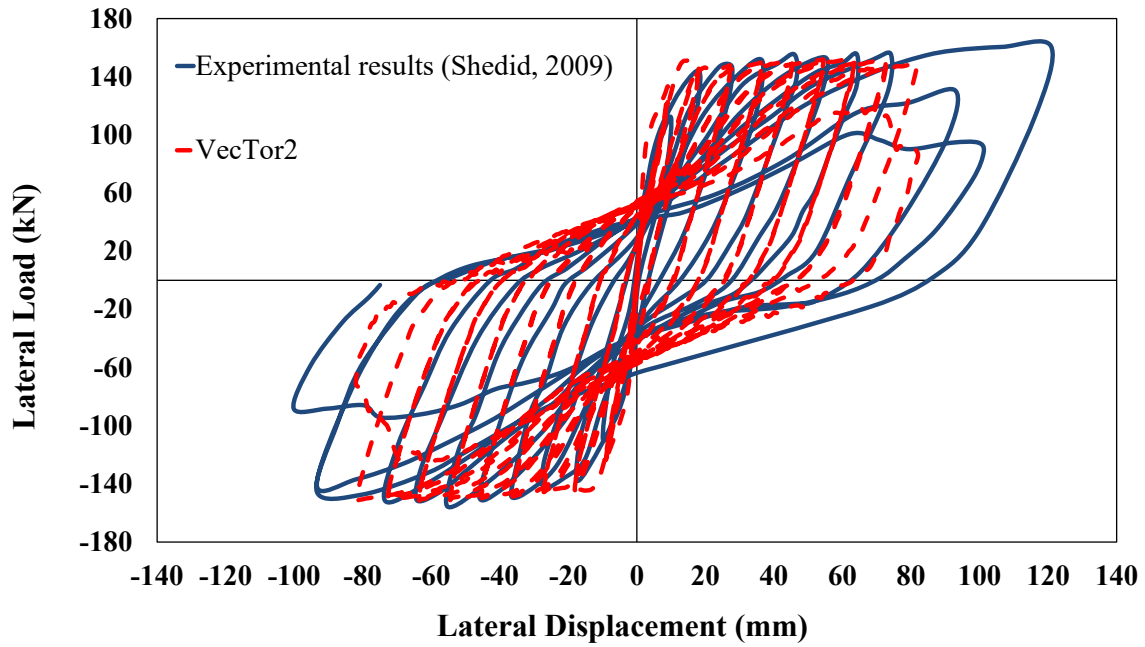
(b)
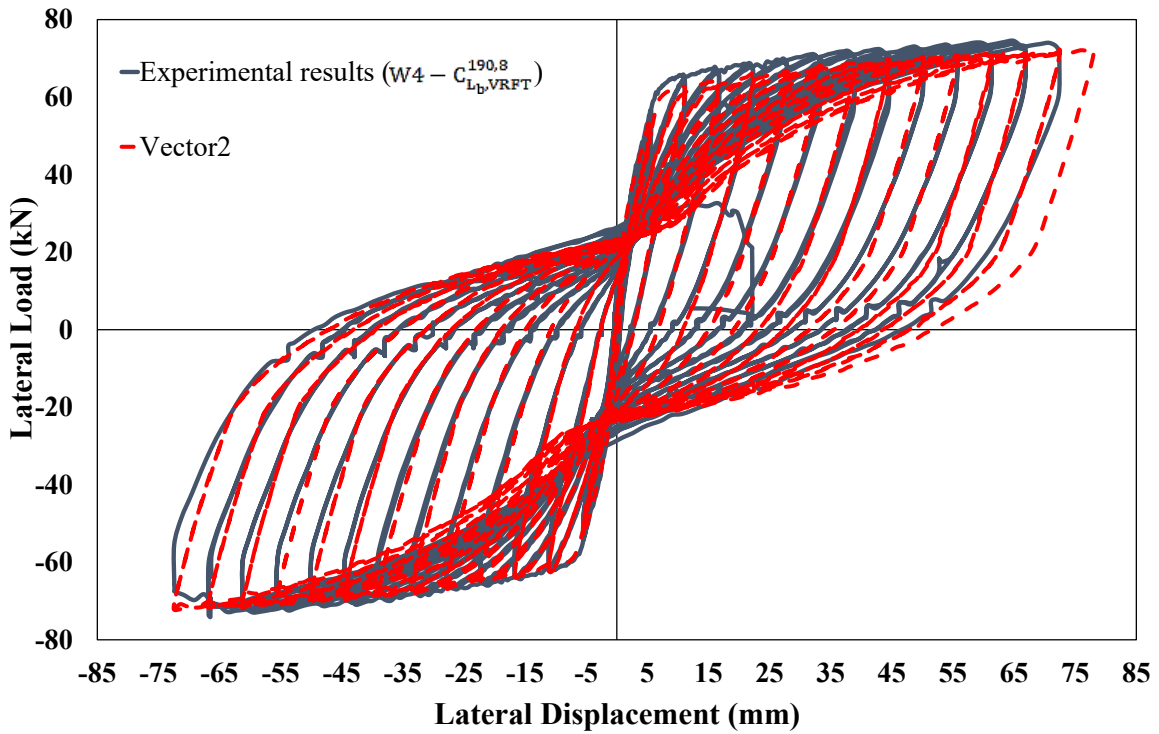
(c)

Figure 6.4: Validation of the numerical model (a) wall 4 [9] ;(b) wall 3 [8]; (c) wall W4-$C_{L_b,VRFT}^{190,8}$
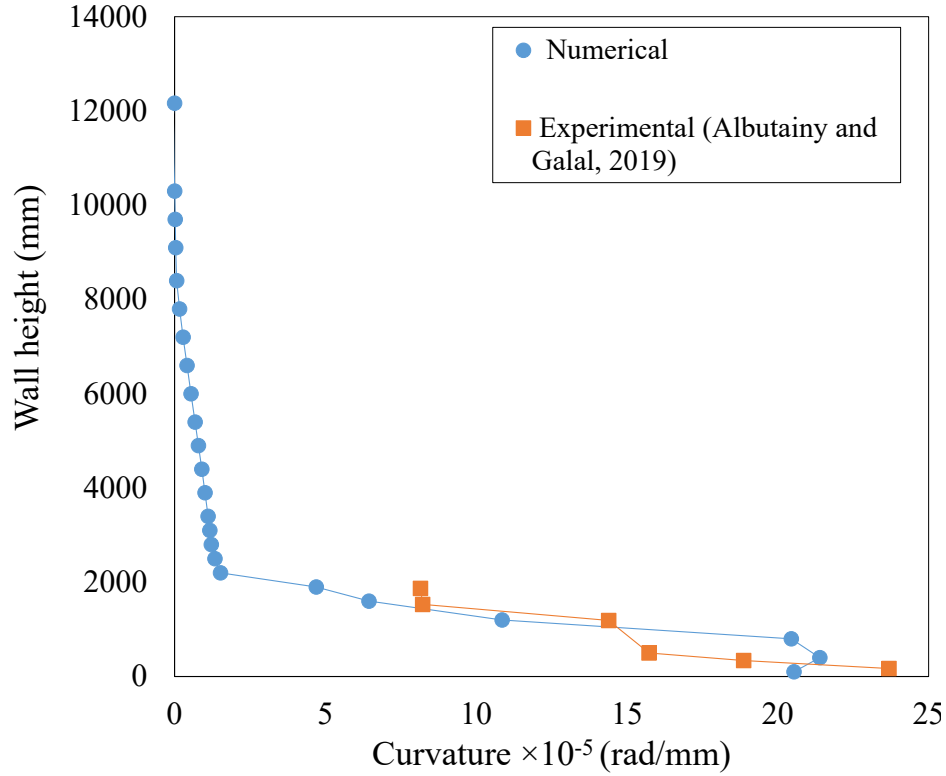
Figure 6.5: Numerical vs experimental curvature profiles
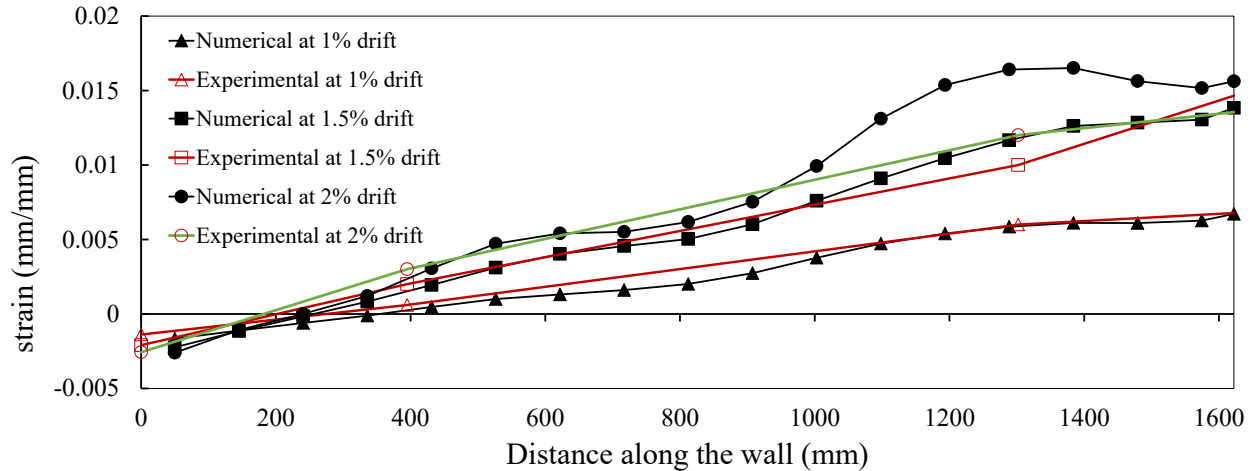
Figure 6.6: Strain profile over the wall 4 length

Following the validation of the numerical model, it has been utilized to investigate the effect of monotonic versus cyclic loading and whether the 2D model can predict the wall response behaviour when it has eccentric boundary elements. In other words, can a 3D model be replaced by a 2D model in such a case? This question has never been addressed before in the literature. These two effects will be discussed in sections 6.1.4 and 6.1.5, respectively.

Figure 6.7 shows the difference between the curvature profiles generated by the numerical model using reversed cyclic and monotonic loading. It can be seen that the loading pattern has minimum effect on the wall's curvature profile. This conclusion is of importance when conducting future parametric studies, as it will simplify the model and speed up the computational effort.
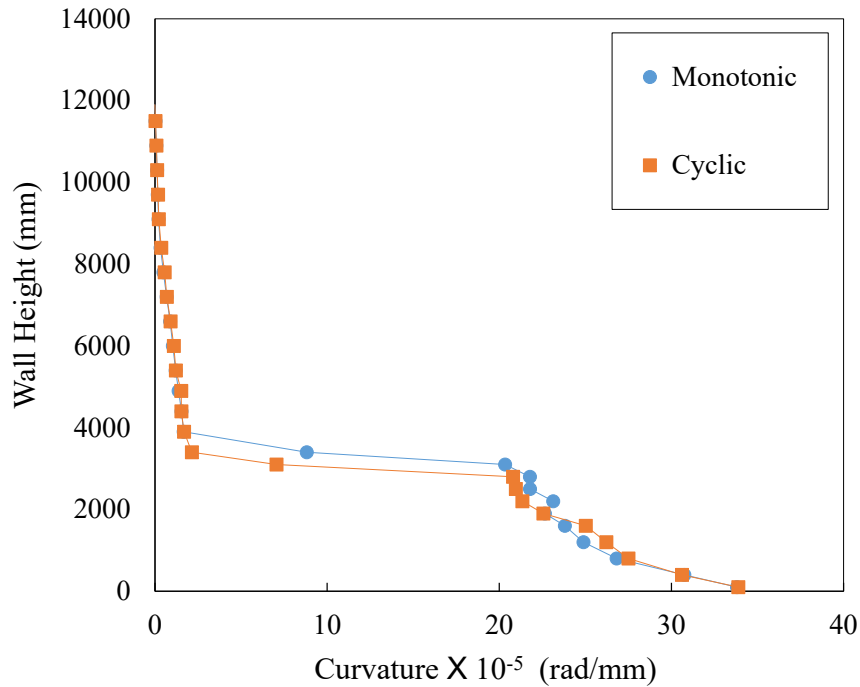
Figure 6.7: Curvature profile generated numerically using reversed cyclic and monotonic loading

6.1.4   Comparison between 3D model and 2D model predictions

The boundary elements in the experimentally tested walls were eccentric with respect to the wall web. As shown in Figure 6.8(b), in the 2D model, it is assumed that the boundary elements are symmetric about the web centerline. To assess the accuracy of the 2D model results, a comparison between the 2D model using vecTor2 and 3D model using VecTor3 was conducted. Due to the limitation of the number of elements in VecToe3, a reduced height model was used. The 2D model was developed as described earlier. For the 3D model, the same material models were used. The element type used in VecTor3 model is the eight-noded regular hexahedral element. Out-of-plan supports were provided to the 3D model to avoid out-of-plane failure. The comparison between the 2D and 3D models considered the deformation and failure mode, the

118

crack pattern and the stress distribution at the failure point. This comparison is shown in Figure 6.9. It can be seen that the eccentricity of the boundary elements is not affecting the predicted lateral force capacity, initial stiffness, stiffness degradation and energy dissipated in each cycle. However, the number of cycles to failure in the 2D model was eight and in the 3D model was 6, which represents the value of the ductility factor. The ductility factor recommended for special reinforced masonry walls in CSA S304-14 [20] is 3.0, which is already less than what is obtained from the two models. Thus, considering the close agreement between the two models until the third cycle, it can be claimed that the responses predicted by both models are similar. Figure 6.10 shows the deformation and the failure mode predicted by the 2D and 3D models at the failure point. The two models showed the same failure mode; failure of the left boundary element and web elements next to the right boundary element. Additionally, the similarity in the crack patterns predicted by the two models can be seen in Figure 6.11. The stress in the vertical reinforcement at the failure point is shown in Figure 6.12. The figure shows that the stress distributions in the vertical reinforcement are also the same in the 2D and 3D models. Therefore, one can conclude that the 2D model, with the assumption that the boundary elements are symmetrical about the web centre line can adequately represent the tested walls with eccentric boundary elements.

(a)

119
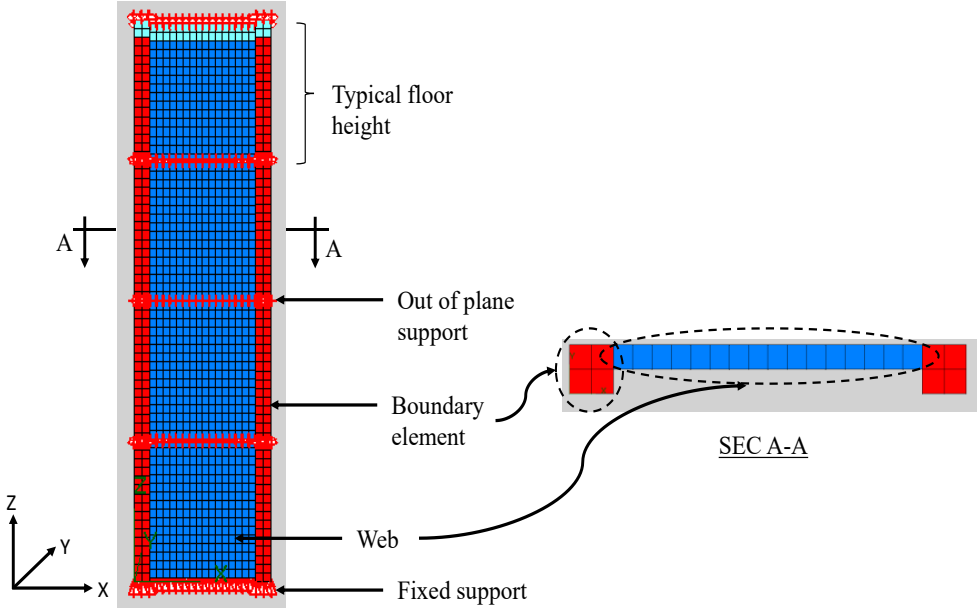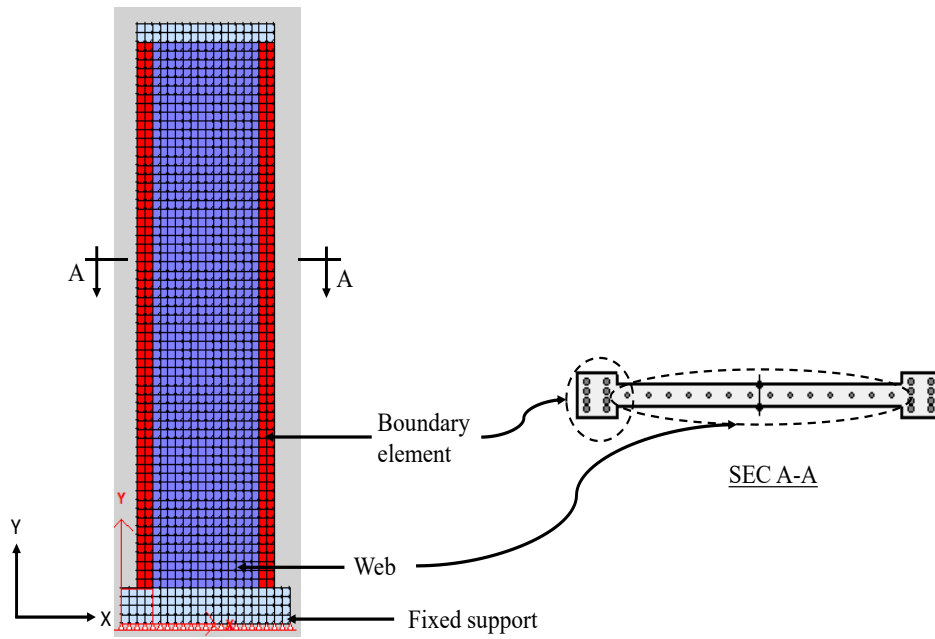
Figure 6.8: a) 3D model configuration b) 2D model configuration
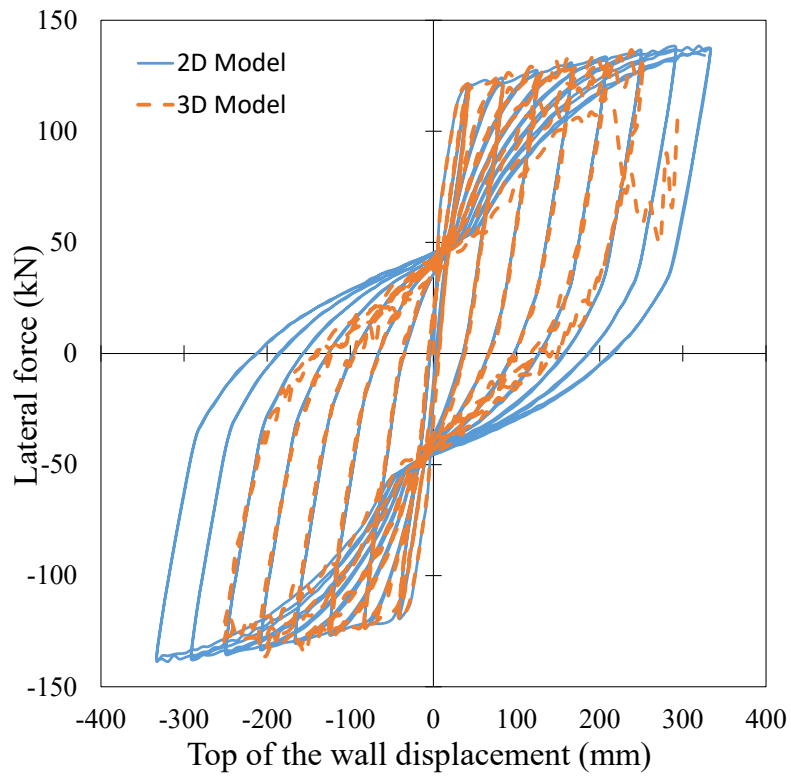
Figure 6.9: Comparison between 2D and 3D model hysteresis output

(a)   (b)
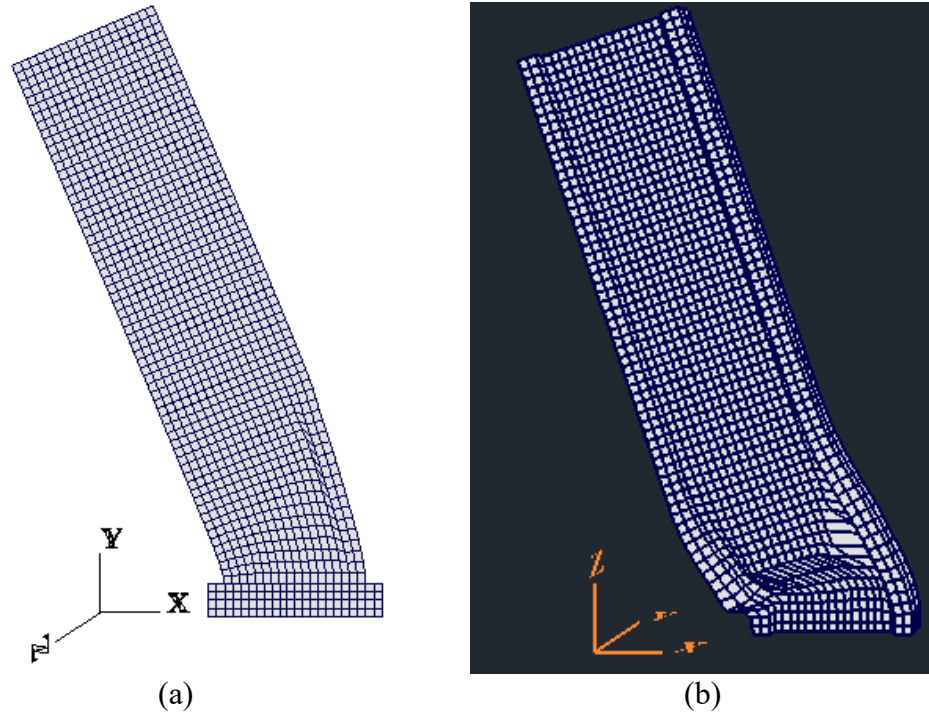
Figure 6.10: Deformation and failure mode a) 2D model, b) 3D model

(a)   (b)
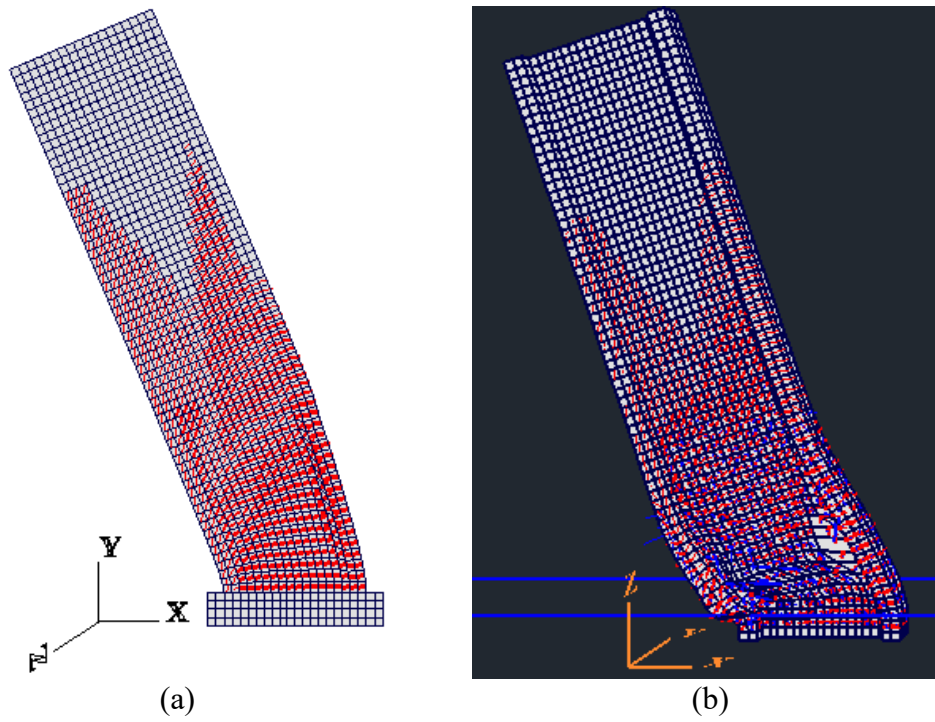
Figure 6.11: Crack Pattern a) 2D model, b) 3D model

121
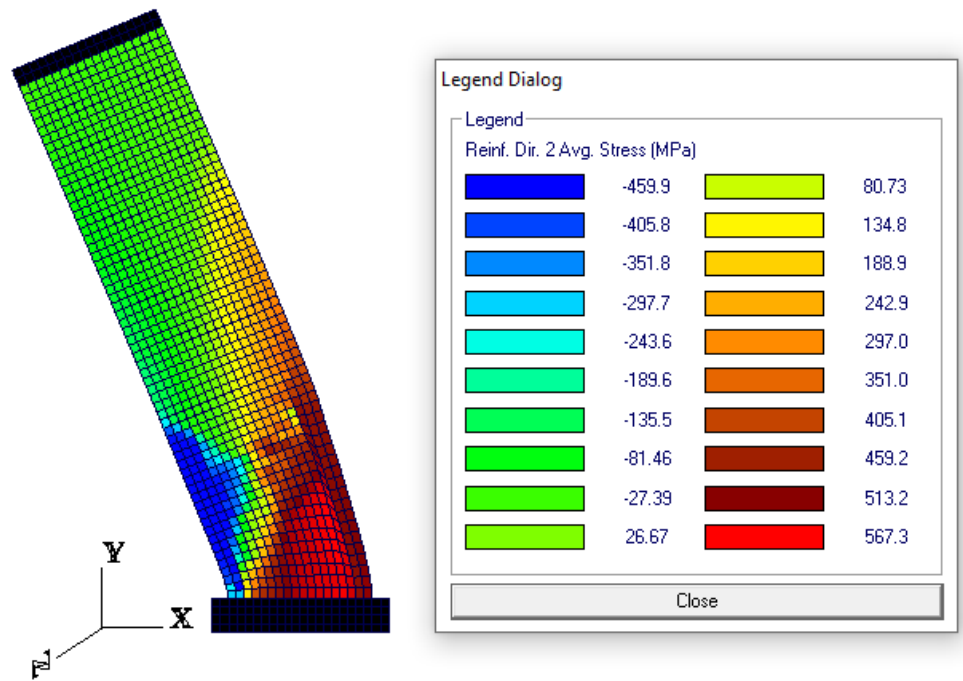
(a)
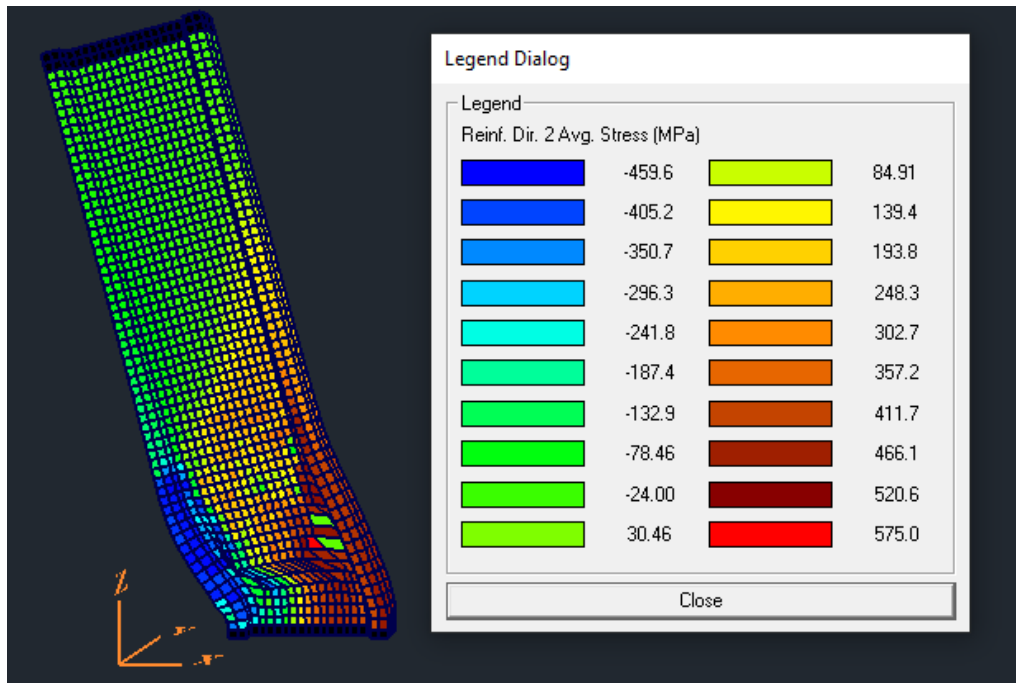
(b)

Figure 6.12: Vertical reinforcement stress distribution predicted by a) the 2D model, and b) the 3D model

6.2   Effect of changing the boundary elements confinement ratio

Phase one of the experimental work aimed at studying the effect of increasing the confinement reinforcement in the boundary elements on the behaviour of RMSW. As explained by the author in [70], walls 1 and W2-C_S^{30} ran into an undesired mode of failure (other than flexural failure), and the effect of increasing the confinement reinforcement in the boundary element couldn't be addressed, mainly due to the cost associated with repeating the tests for W1-C_S^{60} and W2-C_S^{30}. This drawback was the motive for developing and experimentally validating a numerical model to investigate the confinement effect.

6.2.1   Modelled walls

Three half-scaled RMSW+BE were modelled under a reversed cyclic lateral loading. The wall height (h_w) was 18.25 m. The boundary element length (L_b) and width (B_b) were selected to represent a standard masonry concrete block of 190 mm x 190 mm. The three walls have similar vertical and horizontal reinforcement, as shown in Figure 6.13. However, the walls vary in the amount of confinement reinforcement in the boundary elements by changing the spacing between the vertical hoops to 60 mm, 30 mm, and 45 mm for W1-C_S^{60}, W2-C_S^{30} and W3-C_S^{45}, respectively.

The average compressive strength of the boundary elements prisms, f_m, was 23.7 MPa. The average compressive strength of the web prisms, f_m, was 10.20 MPa (C.O.V. = 5.8%). The yield and ultimate strength of #3 vertical bars were determined to be 460 MPa and 680 MPa, respectively. The yield and ultimate strength of D4 bars were 588 MPa and 633 MPa, respectively.

As stated earlier, confinement reinforcement is defined as the ratio between the hoop volume and the concrete between two hoops volume. To determine the unsupported length for vertical reinforcement (b/t), which should be input manually, the method proposed by Dhakal and Maekawa [115] was used. The calculated unsupported length for the vertical reinforcement were 6.3, 3.15 and 4.73 for W1-C_S^{60}, W2-C_S^{30} and W3-C_S^{45}, respectively.

Figure 6.13: Dimensions and reinforcement arrangement of the tested walls (all dimensions are in millimeters)

6.2.2 Force displacement relationship.

Figure 6.14(a, b, and c) shows the force-displacement relationship for the three modelled walls. Increasing the confinement reinforcement in the boundary elements has no effect on the yield and the ultimate lateral resistance. In addition, increasing the confinement reinforcement is not affecting the stiffness degradation. However, reducing the spacing between the confinement reinforcement leads to an increase in the number of cycles to failure, which reflects the increase in the ductility of the wall. The increase in the number of cycles also indicates the increase in the energy dissipated by the wall, which enhances the seismic behaviour of the wall. Figure 6.14(d) shows the skeleton curves for the three modelled walls.

(a)

(b)

(c)

(d)

Figure 6.14: a) Force deformation relationship for W1-C_S^{60}, b) Force deformation relationship for W2-C_S^{30}, and c) Force deformation relationship for W3-C_S^{45}, and d) Skeleton curve for the three walls.

6.2.3 Predicted total strain

Figure 6.15 shows the relation between lateral force and the stain in the vertical reinforcement. For W1-C_S^{60} with hoops spacing of 60 mm (Figure 6.15 (a)), the vertical strain increased suddenly, which indicates the occurrence of buckling. On the other hand, for W2-C_S^{30} and W3-C_S^{45}, no sudden change was predicted in the vertical strain. As shown by Albutainy and Galal in [70], the failure mode for W3-C_S^{45} was global buckling for the boundary element and crushing for the grouted masonry in the web area near the boundary element under compression. It can be concluded that reducing the spacing between the hoops in the boundary element is delaying the vertical reinforcement buckling, and the failure occurred as a result of this buckling. However, reducing the spacing between the hoops will result in a stronger boundary element and will shift the failure to the next weaker area, which is the web. One of the advantages of using C-shaped boundary element is to control the boundary element length to make sure that the strains in the web area will not exceed the value of 0.0025 recommended by CSA S304-14[20].
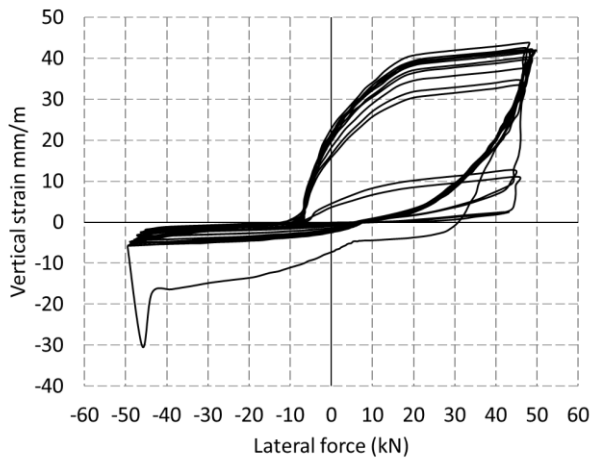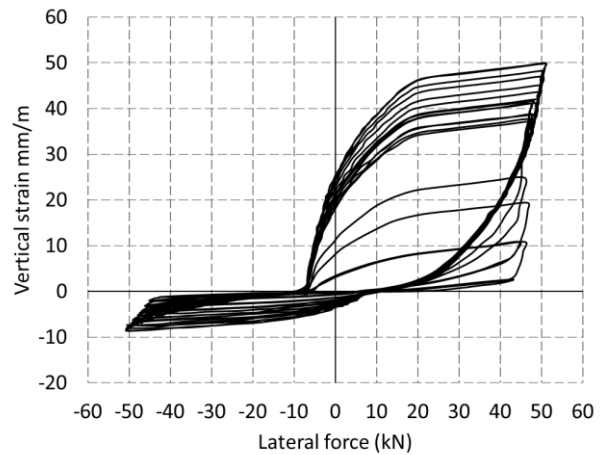
(a)   (b)
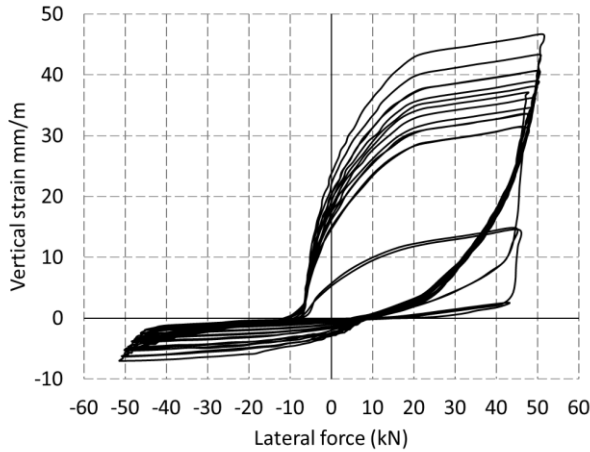
(c)

Figure 6.15: Vertical strain VS lateral force resistance a) W1-C_S^{60}, b) W2-C_S^{30}, c) W3-C_S^{45}

6.3   Conclusions

VecTor2 and VecTor3 software selected material models were used to model fully grouted RMSW with an acceptable accuracy to study the effect of the eccentricity of the boundary elements with respect to the web by comparing 2D and 3D models (objectives #8 and #9). In addition, the 2D model was used to evaluate the effect of changing the confinement ratio in the BE on the behaviour of RMSW+BE (hypothesis #2). The eccentricity of the boundary elements is not affecting the predicted lateral force capacity, initial stiffness, stiffness degradation and energy dissipated in each cycle. The number of cycles to failure in the 2D model was higher than that predicted by the 3D model, which represents the value of the ductility factor. Considering the results obtained from the two models till the third cycle, it can be claimed that the response of the 2D and 3D models are similar. Deformation and failure mode, crack pattern and vertical reinforcement stress distribution generated by the 2D and 3D models at the failure point were found to be the same. Based on the comparison between the 2D and 3D models, it can be concluded that the 2D model, with the assumption that the boundary elements are symmetrical about the web centerline, can represent the tested walls with eccentric boundary elements. Increasing the confinement reinforcement in the boundary elements by reducing the spacing between confinement hoops has no effect on the yield and the ultimate lateral resistance and stiffness degradation. However, it increases the number of cycles to failure, which reflects the increase in the ductility of the wall. The increase in the number of cycles-to-failure also indicates the increase in the energy dissipated by the wall, which enhances the seismic behaviour of the

127

wall. Reducing the spacing between the hoops in the boundary element is delaying/preventing the vertical reinforcement buckling and the failure occurred as a result of this buckling and shifts the failure to the next weaker area (the web). One of the advantages of using C-shaped boundary elements is to control the boundary element length to make sure that the strains in the web area will not exceed the value of 0.0025 recommended by CSA S304-14 [20] for the unconfined zones.

Chapter 7

Summary, Conclusions, and Recommendations

7.1   Summary

Six half-scale RMSW+BE specimens characterized by flexural dominance under reversed cyclic lateral loading and synchronized gravity load and top moment were constructed and tested for this study. These walls represent the plastic hinge zone of a 12-storey reinforced masonry shear wall building. Instead of conventional stretcher units, C-shape masonry units were used to build the boundary elements. The size, vertical reinforcement ratio, and boundary element confinement ratio of the wall's boundary elements were considered as variables in this research.

This study demonstrated, experimentally, that reinforced masonry shear walls (RMSW) are capable of performing as an effective seismic force resisting system (SFRS) for mid-rise buildings in moderate seismic zones. Many confinement techniques were suggested to enhance the RMSW ductility and its energy dissipation capabilities by increasing the measured compressive strain. Adding boundary elements, as an end confinement method, has an advantage over the other proposed confinement methods in providing space for two layers of vertical reinforcement with confinement hoops, providing out-of-plane stability and decreasing the compression zone. The experimental and numerical research work in this thesis provided evidence and a predictive tool for improving the structural performance and constructability of RMSW. These developments were achieved in collaboration with the industrial partners of an NSERC Collaborative Research and Development (CRD) with the industrial partners: Canadian Concrete Masonry Producers Association (CCMPA), Association des Entrepreneurs en Maçonnerie du Québec (AEMQ) and Canada Masonry Design Center (CMDC).

An experimentally validated numerical model was developed to estimate the effect of modifying the confinement reinforcement ratio in reinforced masonry wall boundary elements. The model was validated against the results of three separate experimental programs. A comparison of the results obtained from the 2D model and the 3D model was carried out to determine the effect of eccentricity in the boundary element on the accuracy of the 2D model findings. Furthermore, the influence of the loading protocol used (cyclic vs monotonic) on the wall curvature was examined. The model was used to check the effect of changing the

confinement ratio in the boundary element by changing the spacing between the confinement hoops on the behaviour of the RMSW+BE.

7.2   Conclusions

7.2.1   Conclusions from the experimental work

The following conclusions can be drawn from Phase I experimental work (development of an experimental setup and testing 3 walls):

1. Using C-shaped masonry units to form the boundary elements can reduce the required manpower and the time needed to build shear walls by 50% and 67%, respectively, compared to the walls constructed using regular stretcher units. This was estimated from the mason's productivity in the construction of RMSW+BE from C-shaped blocks compared to stretcher units. From the constructability point of view, it was proved that the C-shape units provided the lateral strength as designed and provided the option of increasing the vertical and confinement reinforcement, as well as the flexibility to change the boundary element length.

2. The test results showed that reducing the spacing between the confinement hoops in the boundary elements eliminated vertical reinforcement buckling or crushing in the grouted core. This is evident from the results of wall $W2\text{-}C_S^{30}$ with 30 mm and $W3\text{-}C_S^{45}$ with 45 mm hoop spacing, where the failure occurred before vertical bars buckled.

3. The out-of-plane failure occurred at the mid-height of $W2\text{-}C_S^{30}$ on the eighth push cycle indicates that providing stronger boundary elements at the wall ends was not sufficient to provide the required support to the web zone to reach an aspect ratio (H/(t+10mm)) of 30 that is higher than the ratio of 24 recommended by CSA S304-14 [4]. As such, providing boundary elements at the ends of the wall does not permit relaxing the current aspect ratio limits in CSA S304-14 [4]. Despite this, the wall had a ductility factor of 7 and was able to maintain its lateral and vertical capacity until the final cycle. The wall failed at the second 8th push cycle due to web crushing and buckling of vertical web reinforcement (in the unconfined zone close to the boundary element), which imposed a lateral strain on the grout and the face shell and produced wall failure.

4. Out-of-plane deformation affected the curvature of the wall, especially for those cycles prior to reaching the out-of-plane displacement critical value. The effective lateral

stiffness for RMSW with C-shaped boundary elements was not affected by the confinement ratio or the failure mode.

5. Lastly, both walls W2-$C_S^{30}$and W3-C_S^{45} have almost the same ratio between the normalized dissipated energy (E/E_y) but at different displacement ductility levels. However, the out-of-plane failure reduced the capability of the wall to dissipate the input energy.

The following conclusions can be drawn from Phase II experimental work (testing of three walls):

1. The cracks developed in the tested walls were mostly limited to the first floor, with only a few cracks extending to the second. This implies that it would be sufficient to test only the lower floor panel in future experimental programs of testing RMSW under cyclic loads. In general, a flexural failure mode, which is characterised by vertical reinforcement yielding, horizontal cracks, and masonry toe-crushing was the dominant failure mechanism of walls. When the applied stresses were increased, vertical splitting cracks in the border elements formed, and spalling ensued, revealing the undamaged grouted core. The confined grout core was toe crushed, and the vertical reinforcement bars in the boundary elements buckled/ruptured as the lateral displacement increased.

2. Changing the boundary element size or the vertical reinforcement ratio in the boundary element were found to have minimal effect on the cracking pattern of the walls.

3. All walls exhibited a consistent hysteretic response with large loops, indicating enhanced energy dissipation levels and damping capability.

4. The walls maintained high ultimate compression strains in the extreme masonry fibres that were more than the value of 0.0025 recommended by CSA S304-14 [20]. The ultimate compression strains could be increased for RMSE+BE to 0.0035, similar to reinforced concrete shear walls. The current CSA S304-14 [20] provisions were capable of predicting the lateral yield force and the ultimate lateral load with an acceptable safety margin for the proposed shear wall system.

5. Increasing the boundary element size from 190x190 mm to 190x290 mm increased the initial stiffness of the wall. However, walls with smaller boundary elements have a higher normalized stiffness compared to walls with larger boundary elements.

6. The vertical reinforcement ratio of the boundary element has a minor influence on the stiffness of the tested walls.

7. Walls with small boundary elements (square 190x190) showed lower measured yield curvature by an average of 22% compared to walls with a larger boundary element (rectangular 190x290).

8. The measured ultimate curvature for wall with a small boundary (square 190x190) element is less than the measured yield curvature in walls with a larger boundary element (rectangular 190x290) by an average of 8%.

9. The comparison revealed that until the yield point, walls with different boundary element sizes have essentially the same normalized moment-curvature relationship, regardless of their configuration. Above the yielding point, increasing the boundary element size led to an increase in curvature.

10. Due to the testing frame limitations, the wall height was not enough to capture the full extent of the plasticity zone of the tested walls. However, the equivalent plastic hinge height was obtained.

11. Based on the test results, there is a potential that the ductility-related force reduction factor for ductile RMSW be increased from 3.0 (recommended by the current CSA S304-14) to at least 3.5. More experimental data are needed to investigate the force reduction factor for RMSW at the component level. In addition, an investigation at the system level by implementing FEMA P-695 [94] methodology is required.

7.2.2 Conclusions from numerical work

To represent the behaviour of reinforced masonry (RM) shear walls, nonlinear finite element (FE) models were developed. The following conclusions can be drawn based on numerical simulations:

1. The modelling methodology and the selected material models of VecTor2 software were able to capture the cyclic response of fully grouted RMSW with acceptable accuracy.

2. The eccentricity of the boundary elements is not affecting the predicted lateral force capacity, initial stiffness, stiffness degradation and energy dissipated in each cycle.

3. The number of cycles to failure in the 2D model was higher than that predicted by the 3D model, which represents the value of the ductility factor. Considering the results obtained from the two models till the third cycle, it can be claimed that the response of the 2D and 3D models are similar.

4. Deformation and failure mode, crack pattern and vertical reinforcement stress distribution generated by the 2D and 3D models at the failure point were found to be the same. As such, 2D models can be confidently used to represent the cyclic response of RMSW+BE at a lower computational effort compared to 3D models.

5. Based on the comparison between the 2D and 3D models, it can be concluded that the 2D model, with the assumption that the boundary elements are symmetrical about the web centre line, can represent the tested walls with eccentric boundary elements.

6. Increasing the confinement reinforcement in the boundary elements by reducing the spacing between confinement hoops has no significant effect on the yield and the ultimate lateral resistance, whereas it increases ductility.

7. Increasing the confinement reinforcement, by reducing the spacing between confinement hoops, has no effect on the stiffness degradation. Mainly the stiffness degradation is related to the crack's propagation. In RMSW+BE, the cracks were mainly horizontal cracks so the hoops are not crossing the propagated cracks to affect the stiffness degradation.

8. Reducing the spacing between the confinement reinforcement leads to an increase of the number of cycles till failure, which reflects the increase in the ductility of the wall. The increase in the number of cycles-to-failure also indicates the increase in the energy dissipated by the wall, which enhances the seismic behaviour of the wall

9. Reducing the spacing between the hoops in the boundary element is delaying/preventing the vertical reinforcement buckling and the failure occurred as a result of this buckling.

10. Reducing the spacing between the hoops results in a stronger boundary element and shifts the failure to the next weaker area (the web). One of the advantages of using C-shaped boundary elements is to control the boundary element length to make sure that the strains in the web area will not exceed the value of 0.0025 recommended by CSA S304-14[20].

7.3 Originality of work and contributions to knowledge

This study presents a contribution to knowledge that led to the enhancement of seismic hazard safety of mid-rise masonry buildings in Canada. The main findings of this thesis would benefit the end-user and stakeholders in the masonry design and the construction industry. These benefits can be categorized as direct and indirect. The direct benefits came from conducting

well-designed experimental and numerical investigations that contributed to enhancing the current construction methods of reinforced masonry boundary elements. The indirect benefit lies in the generation of new experimental and analytical fundamental knowledge that will be useful as a benchmark for other researchers to continue the advancements in this field. The contributions can be listed as follows:

1. This study pushes the existing boundaries by developing an experimental setup that allows testing the plastic hinge zone in 12 storeys RMSW building having an aspect ratio of 10.6, whereas the RM shear wall with the highest tested aspect ratio was 4.5. This aspect has not been investigated before.

2. In-depth knowledge of the seismic performance of RMSW, with newly proposed boundary element formed with C-shaped units based on experimental results.

3. Developing and experimentally validating a numerical model that can simulate the seismic behaviour of the RMSW with c-shaped boundary elements.

4. Establishing the effect of boundary element eccentricity with respect to the web and the effect of changing the boundary element confinement reinforcement spacing.

7.4   Recommendations for Future Work

This research proposed C-shaped units to form the boundary elements in the RMSW to avoid the limitations inherent to the current practice and to enhance the performance of the RMSW. To test the proposed RMSW configuration, a novel test setup was developed, which will open the floor to investigate more parameters with the flexibility to change the wall aspect ratio. As a continuation to the presented research, the following research points are suggested to be investigated in the future:

1. Investigating the behaviour of coupled RMSW+BE.
2. Extending the experimental investigation for the effect of confinement ratio in the boundary elements with different BE sizes.
3. Extending the experimental investigation to walls with different lengths and studying the effect of changing the boundary element length to the wall's overall length on the seismic behaviour of the RMSW.
4. Extending the experimental investigation to apply dynamic loads (shack table test).
5. Extending the experimental investigation to test a building with several RMSW.

6. Extending the numerical investigation to better estimate RMSW plastic hinge height taking into consideration the boundary element configuration.

7. Extend the numerical work to investigate the seismic response of RMSW+BE under real seismic base excitation.

References

[1]   R. P. Clarke, "Sustainable reinforced masonry walls under lateral in-plane load: Experimental behaviour and code-based predictions," *Structures*, vol. 1, pp. 76–83, 2015, doi: 10.1016/j.istruc.2014.10.002.

[2]   NAHB Research Center, "Building Concrete Masonry Homes :Design and Construction Issues," Upper Marlboro, MD, USA, 1998.

[3]   J. B. Mander, M. J. N. Priestley, and R. Park, "Theoretical Stress-Strain Model for Confined Concrete," *J. Struct. Eng.*, vol. 114, no. 8, pp. 1804–1826, 1988.

[4]   M. J. N. Priestley, "Seismic resistance of reinforced concrete-masonry shear walls with high steel percentages.pdf," *Bull. New Zeal. Natl. Soc. Earthq. Eng.*, vol. 10, no. 3, 1977.

[5]   T. Paulay and W. J. Goodsir, "The Ductility of Structural Walls," *Bull. New Zeal. Natl. Soc. Earthq. Eng.*, vol. 18, no. 3, pp. 250–269, 1985.

[6]   H. Sveinsson, B. I., McNiven, H. D., and Sucuoglu, "Cyclic loading tests of masonry single piers, Volume 4_Height to width ratio of 1," Berkeley, California, 1985.

[7]   B. P. B. Shing, A. Member, J. L. Noland, E. Klamerus, and H. Spaeh, "Inelastic Behavior of Concrete Masonry Shear Walls," *ASCE*, vol. 115, no. 9, pp. 2204–2225, 1990.

[8]   M. T. Shedid, W. W. Dakhakhni, and R. G. Drysdale, "Characteristics of Rectangular, Flanged, and End-Confined Reinforced Concrete Masonry Shear Walls for Seismic Design," *J. Struct. Eng.*, vol. 136, no. 12, pp. 1471–1482, 2010, doi: 10.1061/(ASCE)ST.1943-541X.0000253.

[9]   B. R. Banting and W. W. El-Dakhakhni, "Force- and Displacement-Based Seismic Performance Parameters for Reinforced Masonry Structural Walls with Boundary Elements," *J. Struct. Eng.*, vol. 138, no. 12, pp. 1477–1491, 2012, doi: 10.1061/(ASCE)ST.1943-541X.0000572.

[10]   M. T. Shedid, W. W. El-Dakhakhni, and R. G. Drysdale, "Behavior of fully grouted reinforced concrete masonry shear walls failing in flexure: Experimental Results," *Eng. Struct.*, vol. 31, no. 9, pp. 2032–2044, 2009, doi: 10.1016/j.engstruct.2009.03.006.

[11]   M.J.N.Priestly, "Ductility of Unconfined Masonry Shear Walls," *Bull. New Zeal. Natl. Soc. Earthq. Eng.*, vol. 14, no. 1, pp. 12–20, 1981.

[12]   M. T. Shedid, W. W. El-Dakhakhni, and R. G. Drysdale, "Behavior of fully grouted reinforced concrete masonry shear walls failing in flexure: Analysis," *Eng. Struct.*, vol. 31, no. 9, pp. 2032–2044, 2009, doi: 10.1016/j.engstruct.2009.03.006.

[13]   N. A. Hart, G. C., Noland, J. L., Kingsley, G. R., Englekirk, R. E. and Sajjad, "The use of confinement steel to increase the ductility in reinforced masonry shear walls," *Mason. Soc. J.*, vol. 7, no. 2, 1988.

[14]   B. R. Banting, "Seismic Performance Quantification of Concrete Block Masonry Structuralwalls With Confined Boundary Elements and Development of The Normal

Strain-Adjusted Shear Strength Expression (Nssse)," McMaster University, 2013.

[15] M. Priestley and T. Paulay, "Seismic design of reinforced concrete and masonry buildings," *1992*. 1992, [Online]. Available: http://is-this-book-good.info/wp-content/uploads/pdfs/Seismic Design of Reinforced Concrete and Masonry Buildings by M J N Priestley - Must Have.pdf.

[16] P. B. Shing, E. Klamerus, H. Spaeh, and J. L. Noland, "Seismic Performance of Reinforced Masonry Shear Walls," *9th World Conference on Earthquake Engineering*. p. Vol. 6:103-108, 1988.

[17] A. Matsumura, "Shear strength of reinforced masonry walls," *9th World Conference of Earthquake Engineering*, vol. Vol. 6. pp. 121–126, 1988.

[18] B. R. Robazza, S. Brzev, T. Y. Yang, K. J. Elwood, D. L. Anderson, and B. McEwen, "Out-of-Plane Behavior of Slender Reinforced Masonry Shear Walls under In-Plane Loading: Experimental Investigation," *J. Struct. Eng.*, vol. 144, no. 3, p. 04018008, 2018, doi: 10.1061/(ASCE)st.1943-541x.0001968.

[19] M. Albutainy, A. Ashour, and K. Galal, "Effect of boundary elements confinement level on the behaviour of reinforced masonry structural walls with boundary elements," in *13th Canadian Masonry Symposium*, 2017, no. July.

[20] CSA S304-14, "Design of Masonry Structures," *CSA Group*. CSA Group, Mississauga, Ontario, p. 169, 2014, doi: 10.1080/09613218309442127.

[21] Canadian Commission on Building and Fire Codes, "National Building Code of Canada 2015," vol. 1. National Research Council of Canada, 2015.

[22] Ahmadi F. K., "Displacement-based Seismic Design and Tools for Reinforced Masonry Shear-Wall Structures," The University of Texas at Austin, 2012.

[23] P. B. Shing, E. W. Carter, and J. L. Noland, "Influence of Confining Steel on Flexural Response of Reinforced Masonry Shear Walls," *Mason. Soc. J.*, vol. 11, no. 2, 1993.

[24] D. Anderson and S. Brzev, *Seismic design guide for masonry buildings*, no. April. Toronto, ON: Canadian Concrete Masonry Producers Association, 2009.

[25] R. Park and T. Paulay, *Reinforced Concrete Structures*. Toronto: A Wiley-Interscience publication, 1975.

[26] H. Sveinsson, B. I., McNiven, H. D., and Sucuoglu, "Cyclic loading tests of masonry piers," Berkeley, California, 1985.

[27] M. Tomaževič and M. Lutman, "Seismic resistance of reinforced masonry walls," in *9th World Conference on Earthquake Engineering*, 1988, vol. Vol. VI, pp. 97–102.

[28] G. R. Kingsley, F. seible, R. E. Klingner, and P. B. Shing, "Testing of large-scale reinforced Masonry components and systems," San Diego, 1994.

[29] K. C. Voon and J. M. Ingham, "Experimental In-Plane Shear Strength Investigation of Reinforced Concrete Masonry Walls," *J. Struct. Eng.*, vol. 132, pp. 400–408, 2006, doi: 10.1061/(ASCE)0733-9445(2006)132:3(400).

[30] S. C. Miller, W. W. El-Dakhakhni, and R. G. Drysdale, "Experimental Evaluation of the Shear Capacity of Reinforced Masonry Shear Walls," in *10th Canadian Masonry Symposium*, 2005, p. 10.

[31] W. W. El-Dakhakhni, B. R. Banting, and S. C. Miller, "Seismic performance parameter quantification of shear-critical reinforced concrete masonry squat walls," *J. Struct. Eng.*, vol. 139, no. June, pp. 957–973, 2013, doi: 10.1061/(ASCE)ST.1943-541X.0000713.

[32] W. J. Newmark, N. M. and Hall, "Seismic design criteria for nuclear reactor facilities Report No. 46," 1973.

[33] A. K. Chopra, *Dynamics of structures : theory and applications to earthquake engineering*. 2007.

[34] R. G. Drysdale, A. A. Hamid, and L. R. Baker, *Masonry structures: behaviour and design*. Prentice Hall, 1994.

[35] M. T. Shedid, "Strategies To Enhance Seismic Performance of Reinforced Masonry Shear Walls," McMaster University, 2009.

[36] V. Colotti, "Modeling of Flexural and Shear Response in Reinforced Masonry Walls Under Seismic Loading," *TMS J.*, pp. 37–48, 2001.

[37] T. Paulay and S. M. Uzumeri, "A Critical Review of the Seismic Design Provisions for Ductile Shear Walls of the Canadian Code and Commentary," *Can. J. Civ. Eng.*, vol. 2, no. 4, pp. 592–601, 1975, doi: 10.1139/l75-054.

[38] M. J. N. Priestley and M. J. Kowalsky, "Aspects of drift and ductility capacity of rectangular cantilever structural walls," *Bull. New Zeal. Natl. Soc. Earthq. Eng.*, vol. 31, no. 2, pp. 73–85, 1998.

[39] A. Bohl and P. Adebar, "Plastic hinge lengths in high-rise concrete shear walls," *ACI Struct. J.*, vol. 108, no. 2, pp. 148–157, 2011, doi: 10.1073/pnas.0703993104.

[40] M. T. Shedid and W. W. El-Dakhakhni, "Plastic Hinge Model and Displacement-Based Seismic Design Parameter Quantifications for Reinforced Concrete Block Structural Walls," *J. Struct. Eng.*, vol. 140, no. 4, p. 04013090, 2014, doi: 10.1061/(ASCE)ST.1943-541X.0000883.

[41] D. Williams, "Seismic behaviour of reinforced masonry shear walls," 1971.

[42] M. Priestley, "Seismic resistance of brick masonry walls," *Bull. New Zeal. Natl. Soc. Earthq. Eng.*, vol. 7, no. 4, 1974.

[43] M. J. N. Priestley and Dm. Elder, "Cyclic loading tests of slender concrete masonry shear walls," *Bull. New Zel. Natl. Soc. Earthq. Eng.*, vol. 15, no. 1, pp. 3–21, 1982.

[44] T. Kaminosono, M. Teshigawara, H. Haraishi, M. Fujiissawa, and A. Nakaoka, "Experimental study on seismic performance of reinforced masonry walls," in *Proceeding of ninth world conference on earthquake engineering*, 1988, pp. VI-109-VI–114.

[45] J. D. B. and P. B. Shing, "Shear Strength of reinforced Masonry walls." .

[46]   "confinement of concrete masonry," University of California, 1990.

[47]   G. Ibrahim, Khaled; Suter, "Ductility of concrete masonry shear walls subjected to cyclic loading," 1999.

[48]   M. Snook, D. McLean, C. McDaniel, and D. Pollock, "Effects of confinement reinforcement on the performance of lap splices in concrete masonry," in *10th Canadian Masonry Symposium*, 2005, p. 11.

[49]   K. C. Voon and J. M. Ingham, "Experimental In-Plane Shear Strength Investigation of Reinforced Concrete Masonry Walls," *J. Struct. Eng.*, vol. 132, no. 3, pp. 400–408, 2006, doi: 10.1061/(ASCE)0733-9445(2006)132:3(400).

[50]   M. T. Shedid, W. W. El-Dakhakhni, and R. G. Drysdale, "Alternative Strategies to Enhance the Seismic Performance of Reinforced Concrete-Block Shear Wall Systems," *J. Struct. Eng. ASCE*, vol. 136, no. 6, pp. 676–689, 2010, doi: 10.1061/(ASCE)ST.1943-541X.0000164.

[51]   C. M. Kapoi, "Experimental performance of concrete masonry shear walls under in-plane loading," WASHINGTON STATE UNIVERSITY, 2012.

[52]   F. Ahmadi, J. Hernandez, J. Sherman, C. Kapoi, R. E. Klingner, and D. I. McLean, "Seismic Performance of Cantilever-Reinforced Concrete Masonry Shear Walls," *J. Struct. Eng.*, vol. 140, no. 9, p. 04014051, 2014, doi: 10.1061/(ASCE)ST.1943-541X.0000941.

[53]   Y. Zhao and F. Wang, "Experimental studies on behaviour of fully grouted reinforced-concrete masonry shear walls," *Earthq. Eng. Eng. Vib.*, vol. 14, no. 4, pp. 743–757, 2015, doi: 10.1007/s11803-015-0030-5.

[54]   N. Aly and K. Galal, "Experimental Investigation of Axial Load and Detailing Effects on the Inelastic Response of Reinforced-Concrete Masonry Structural Walls with Boundary Elements," *J. Struct. Eng.*, vol. 146, no. 12, p. 04020259, 2020.

[55]   N. Priestley, "Ductility of confined concrete masonry shear walls," *Bull. New Zeal. Natl. Soc. Earthq. Eng.*, vol. 15, no. 1, pp. 22–26, 1982.

[56]   A. Abo El Ezz, H. M. Seif Eldin, and K. Galal, "Influence of confinement reinforcement on the compression stress-strain of grouted reinforced concrete block masonry boundary elements," *Structures*, vol. 2, pp. 32–43, 2015, doi: 10.1016/j.istruc.2015.01.001.

[57]   A. T. Obaidat, A. Abo El Ezz, and K. Galal, "Compression behaviour of confined concrete masonry boundary elements," *Eng. Struct.*, vol. 132, pp. 562–575, 2017, doi: 10.1016/j.engstruct.2016.11.043.

[58]   B. AbdelRahman and K. Galal, "Monotonic and cyclic stress-strain models for confined concrete-masonry shear wall boundary elements," *Eng. Struct.*, vol. 249, no. January, 2021, doi: 10.1016/j.engstruct.2021.113343.

[59]   H. Krawinkler, "Scale effects in static and dynamic model testing of structures," in *9th World Conference on Earthquake Engineering*, 1988, pp. 2–9, [Online]. Available: http://www.iitk.ac.in/nicee/wcee/article/9_vol8_865.pdf.

139

[60] M. Tomaževič and T. Velechovsky, "Some aspects of testing small-scale masonry building models on simple earthquake simulators," *Earthq. Eng. Struct. Dyn.*, vol. 21, no. 11, pp. 945–963, 1992, doi: 10.1002/eqe.4290211102.

[61] H. Krawinkler, "Possibilities and limitations of scale-model testing in earthquake engineering," in *Proceedings of the Second US National Conference on Earthquake Engineering.*, 1979, pp. 283–292.

[62] D. Abrams, "Effects of Scale and Loading Rate with Tests of Concrete and Masonry Structure." 1996.

[63] M. Corradi, E. Speranzini, and G. Bisciotti, "Out-of-plane reinforcement of masonry walls using joint-embedded steel cables," *Bull. Earthq. Eng.*, vol. 18, no. 10, pp. 4755–4782, 2020, doi: 10.1007/s10518-020-00875-3.

[64] B. E. Abboud, A. A. Hamid, and H. G. Harris, "Small-scale modelling of concrete block masonry structures," *ACI Struct. J.*, vol. 87, no. 2, pp. 145–155, 1990.

[65] L. Long, A. Hamid, and R. Drysdale, "Small-scale modelling of concrete masonry using ½ scale units: a preliminary study," 2005, [Online]. Available: http://canadamasonrydesigncentre.com/download/10th_symposium/4b-4.pdf.

[66] A. Mohammed, T. G. Hughes, and A. Mustapha, "The effect of scale on the structural behaviour of masonry under compression," *Constr. Build. Mater.*, vol. 25, no. 1, pp. 303–307, 2011, doi: 10.1016/j.conbuildmat.2010.06.025.

[67] V. G. Haach, G. Vasconcelos, and P. B. Lourenço, "Parametrical study of masonry walls subjected to in-plane loading through numerical modelling," *Eng. Struct.*, vol. 33, no. 4, pp. 1377–1389, 2011, doi: 10.1016/j.engstruct.2011.01.015.

[68] E. Minaie, F. L. Moon, and A. A. Hamid, "Nonlinear finite element modelling of reinforced masonry shear walls for bidirectional loading response," *Finite Elem. Anal. Des.*, vol. 84, pp. 44–53, 2014, doi: 10.1016/j.finel.2014.02.001.

[69] H. M.Seif Eldin, M. Albutainy, and K. Galal, "Parametric Study To Investigate the Shear Behavior of Reinforced Masonry Shear walls," 2015.

[70] M. Albutainy and K. Galal, "Experimental investigation of reinforced concrete masonry shear walls with C-shaped masonry units boundary elements," *Structures*, vol. 34, no. January, pp. 3667–3683, 2021, doi: 10.1016/j.istruc.2021.09.080.

[71] B. R. Banting, "Boundary Element Unit Primer - Draft," 2015.

[72] B. Robazza, K. J. Elwood, D. L. Anderson, and S. Brzev, "in-Plane Seismic Behaviour of Slender Reinforced Masonry Shear Walls : Experimental Results," in *12th Canadian Masonry Symposium*, 2013, vol. 2010, no. Nbcc 2010.

[73] N. Taly, *Design of Reinforced Masonry Structures*. 2010.

[74] L. N. Lowes, D. E. Lehman, A. C. Birely, D. A. Kuchma, K. P. Marley, and C. R. Hart, "Earthquake response of slender planar concrete walls with modern detailing," *Eng. Struct.*, vol. 43, pp. 31–47, 2012, doi: 10.1016/j.engstruct.2012.04.040.

[75]   Standard Specification for Mortar for Unit Masonry, "Standard Specification for Mortar for Unit Masonry," *United States: American Society for Testing and Material.* pp. 2–13, 2007, doi: 10.1520/C0270-10.

[76]   CSA, *Mortar and grout for unit masonry, A179-14*, vol. 14, no. July 2015. Toronto, Ontario, Canada: Canadian Standards Association, 2014.

[77]   American Society for Testing and Materials (ASTM), "Standard Test Methods for Sampling and Testing Concrete Masonry Units and Related Units,C140/C140M." American standard for testing materials, West Conshohocken, PA, United States, p. 24, 2015, doi: 10.1520/C0140.

[78]   American Society for Testing and Materials (ASTM), "Standard Specification for Deformed and Plain Carbon Steel Bars for Concrete, ASTM A615/A615M." American standard for testing materials, West Conshohocken, Pennsylvania, United States, p. 6, 2004, doi: 10.1520/A0615.

[79]   American Society for Testing and Materials (ASTM), "Standard Specification for Steel Welded Wire Reinforcement, Plain, for Concrete, ASTM A1064/A1064M-12." American standard for testing materials, West Conshohocken, United States, p. 11, 2012, doi: 10.1520/A1064.

[80]   G. H. Powell, "Displacement-Based Seismic Design of Structures," in *Earthquake Spectra*, 2008, vol. 24, no. 2, pp. 555–557, doi: 10.1193/1.2932170.

[81]   Y. Oh, S. W. Han, and L. Lee, "Effect of boundary element details on the seismic deformation capacity of structural walls," *Earthq. Eng. Struct. Dyn.*, vol. 31, no. January, pp. 1583–1602, 2002, doi: 10.1002/eqe.177.

[82]   M. Albutainy and K. Galal, "Effect of Changing Boundary Element Size on The Response Of Reinforced Concrete Masonry Shear Walls with C-Shape Boundary Element," in *Proceedings, Annual Conference - Canadian Society for Civil Engineering*, 2019, vol. 2019-June, no. 2010, pp. 1–9.

[83]   M. Albutainy and K. Galal, "Ductility of Reinforced Masonry Shear Walls With C-Shaped Boundary Elements," in *12th Canadian Conference on Earthquake Engineering*, 2019, pp. 2–8.

[84]   American Society for Testing and Materials (ASTM), "Standard test method for compressive strength of cylindrical concrete specimens, C39-15." West Conshohocken, PA, United States of America, 2015.

[85]   Canadian Standards Association (CSA)., "CSA standards on concrete masonry units, A165-14." Mississauga, Ontario, Canada, 2014.

[86]   Canadian Standards Association (CSA)., "Mortar and grout unit masonry, A179-14." Toronto, Ontario, Canada, 2014.

[87]   American Society for Testing and Materials (ASTM), "Standard test method for compressive strength of hydraulic cement mortars (using 2-in. or [50-mm] cube specimens), C109M-13." 1West Conshohocken, PA, United States of America; 2013.

[88] T. S. Welt, L. M. Massone, J. M. LaFave, D. E. Lehman, S. L. McCabe, and P. Polanco, "Confinement Behavior of Rectangular Reinforced Concrete Prisms Simulating Wall Boundary Elements," *J. Struct. Eng.*, vol. 143, no. 4, p. 04016204, 2017, doi: 10.1061/(ASCE)ST.1943-541X.0001682.

[89] W. El-Dakhakhni, "Resilient Reinforced Concrete Block Shear Wall Systems for the Next-generation of Seismic Codes," in *International Masonry Conference 201El-Dakhakhni, W. (2014). Resilient Reinforced Concrete Block Shear Wall Systems for the Next-generation of Seismic Codes. International Masonry Conference 2014, 1–34.4*, 2014, pp. 1–34.

[90] M. J. N. Priestley, "Performance based seismic design," *Bull. New Zeal. Soc. Earthq. Eng.*, vol. 33, no. 3, pp. 325–346, 2000, doi: 10.4018/978-1-4666-1640-0.ch002.

[91] G. M. Calvi, M. J. N. Priestley, and M. J. Kowalsky, "Displacement-Based Seismic Design of Structures," *Earthq. Spectra*, vol. 24, no. 2, pp. 555–557, 2008, doi: 10.1193/1.2932170.

[92] S. R. Razvi and M. Saatcioglu, "Analysis and design of concrete columns for confinement," *Earthq. Spectra*, vol. 15, no. 4, pp. 791–810, 1999, doi: 10.1193/1.1586072.

[93] American Society of Civil Engineers, "Minimum design loads and associated criteria for buildings and other structures, ASCE7-16," *American Society of Civil Engineers*. Reston, Virginia, USA, pp. 1–889, 2017, doi: 10.1061/9780784414248.

[94] FEMA P-695, "Quantification of Building Seismic Performance Factors," *Fema P695*, no. June. p. 421, 2009.

[95] H. Park and T. Eom, "Energy Dissipation Capacity of Flexure-Dominated Reinforced Concrete Members," in *13th World Conference on Earthquake Engineering World Conference on Earthquake Engineering*, 2004, no. 3481, [Online]. Available: http://www.iitk.ac.in/nicee/wcee/article/13_3481.pdf.

[96] M. J. N. Priestley, G. M. Calvi, and M. J. Kowalsky, *Displacement-Based Seismic Design of Structures*. Pavia, Italy: Fondazione Eucentre, 2007.

[97] A. S. Elnashai and L. Di Sarno, *Fundamentals of Earthquake Engineering*. 2008.

[98] T. Wong, P. S., and F. J., Vecchio, H., "VecTor2 & Formworks User's Manual Second Edition," University of Toronto, 2002.

[99] F. ElMohandes and F. J. Vecchio, "VecTor3: A. User's Manual B. Sample Coupled Thermal and Structural Analysis," *A Companion to Cognitive Science*, no. November. Toronto, Canada, p. 153, 2013, doi: 10.1002/9781405164535.ch35.

[100] K. S. Ibrahim and G. T . Suter, "SMEARED CRACK MODEL FOR REINFORCED CONCRETE MASONRY SHEAR WALL ANALYSIS," in *10th IB2Mac*, 1994, pp. 731–740.

[101] L. Facconi, D. Ph, G. Plizzari, and F. Vecchio, "Disturbed Stress Field Model for Unreinforced Masonry," *J. Struct. Eng.*, vol. 140, no. 4, pp. 1–11, 2014, doi:

10.1061/(ASCE)ST.1943-541X.0000906.

[102] P. B. Shing, H. R. Lotfi, A. Barzegarmehrabi, and J. Brunner, "Finite Element Analysis of Shear Resistance of Masonry Wall Panels with and without Confining Frames," *Earthquake Engineering, Tenth World Conference*. pp. 2581–2586, 1992.

[103] R. D. Ewing, A. M. El-Mustapha, and J. C. Kariotis, "Finite Element Computer Program For The Nonlinear Static Analysis Of Reinforced Masonry Walls," in *Brick and Block Masonry(8 th IBMAC)*, 1988, pp. 1119–1130.

[104] Serhan Güner, "Performance Assessment Of Shear-Critical Reinforced Concrete Plane Frames," University of Toronto, 2008.

[105] F. J. Vecchio and M. P. Collins, "Modified Compression-Field Theory for Reinforced Concrete Elements Subjected To Shear.," *Journal of the American Concrete Institute*, vol. 83, no. 2. pp. 219–231, 1986, doi: 10.14359/10416.

[106] F. J. Vecchio, D. Lai, W. Shim, and J. Ng, "Disturbed Stress Field Model for Reinforced Concrete: Validation," *Journal of Structural Engineering*, vol. 127, no. 4. pp. 350–358, 2001.

[107] E. Minaie, F. L. Moon, and A. A. Hamid, "Nonlinear finite element modelling of reinforced masonry shear walls for bidirectional loading response," *Finite Elem. Anal. Des.*, vol. 84, pp. 44–53, 2014, doi: 10.1016/j.finel.2014.02.001.

[108] B. J. Hoshikuma, K. K. Member, K. Nagaya, and A. W. Taylor, "Stress-Strain Model For Confined Reinforced Concrete In Bridge Piers," *J. Struct. Eng.*, vol. 123, no. 1992, pp. 624–633, 1997.

[109] F. J. Vecchio, "Finite element modelling of concrete expansion and confinement," *J. Struct. Eng.*, vol. 118, no. 9, pp. 2390–2406, 1992.

[110] H. Kupfer, H. K. Hilsdorf, and H. Rusch, "Behavior of Concrete under Biaxial Stress," *ACI J.*, vol. 87, no. 2, pp. 656–666, 1969.

[111] A. Richart, Frank Erwin; Brandtzæg and R. L. Brown, "A study of the failure of concrete under combined compressive stresses," in *University of Illinois. Engineering Experiment Station. Bulletin*, 1928, vol. 26, no. 12.

[112] R. P. Dhakal and K. Maekawa, "Modeling for Postyield Buckling of Reinforcement," *J. Struct. Eng.*, vol. 128, no. 9, pp. 1139–1147, 2002, doi: 10.1061/(asce)0733-9445(2002)128:9(1139).

[113] R. P. Dhakal and K. Maekawa, "Reinforcement Stability and Fracture of Cover Concrete in Reinforced Concrete Members," *J. Struct. Eng.*, vol. 128, no. 10, pp. 1253–1262, 2002, doi: 10.1061/(asce)0733-9445(2002)128:10(1253).

[114] E. C. Bentz, "Sectional Analysis of Reinforced Concrete Members," University of Toronto, 2000.

[115] R. P. Dhakal and K. Maekawa, "Path-dependent Cyclic Stress-Strain Relationship of Reinforcing bar including buckling," *Eng. Struct.*, vol. 24, no. 11, pp. 1383–1396.

Appendix A

Calculating the critical buckling load for W2-C$_s^{30}$ boundary element

$P_f = 288525$ N   Applied axial load

$A_{d=} 4 \times 71 = 284$ mm   Area of distributed reinforcement

$T_1 = \phi_s A_d f_y = 96560$ N   Tension in distributed reinforcement

$T_2 = \phi_s A_{BE} f_y = 96560$ N   Tension in BE reinforcement

$C_s = \phi_s A_{BE} f_y = 96560$ N   Compression in BE reinforcement

A_l = compression zone area

$C_m = 0.85 \phi_m f_m' A_l = 0.85 \times 0.8 \times 23.7 \times A_l = 16.116\ A_l$

$P_f + T_1 + T_2 - C_s - C_m = 0$

$C_m = 385085$ N   Compression in BE

Thus,

$A_l = 23894.57$ mm$^2 = a \times 190$ mm

Thus,

$a = 125.7$ mm

$P_{cr} = \dfrac{\pi^2 \phi_{cr} E_m I}{(1+0.5\beta_d)(kh)^2}$ Critical load

$I = \dfrac{125.7 \times 190^3}{12} = 71848025$ mm^4

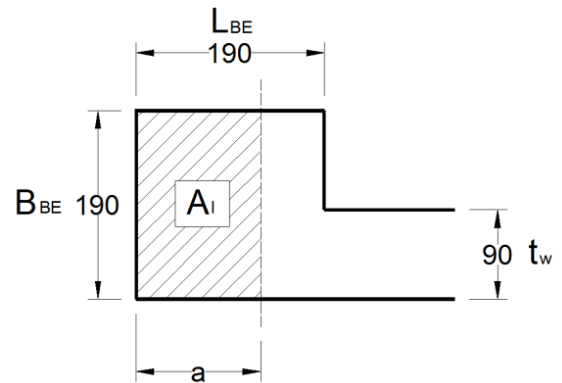$E_m = 850 \times 23.7 = 20145$ MPa

$k = 1.0$

$\phi_{cr} = 0.75$

$\beta_d = 0$

$h = 2338$ mm

$P_{cr} = 1958$ kN

$P_{fb} = C_m + \phi_s A_s f_y = 433.36$ kN < 1958 kN

Out-of-plane buckling resistance is adequate

Compression zone area